

Two dimensional gas temperature measurements of fuel sprays in a high pressure cell

Citation for published version (APA):

Yu, M. (2012). *Two dimensional gas temperature measurements of fuel sprays in a high pressure cell*. [Phd Thesis 1 (Research TU/e / Graduation TU/e), Mechanical Engineering]. Technische Universiteit Eindhoven. <https://doi.org/10.6100/IR741677>

DOI:

[10.6100/IR741677](https://doi.org/10.6100/IR741677)

Document status and date:

Published: 01/01/2012

Document Version:

Publisher's PDF, also known as Version of Record (includes final page, issue and volume numbers)

Please check the document version of this publication:

- A submitted manuscript is the version of the article upon submission and before peer-review. There can be important differences between the submitted version and the official published version of record. People interested in the research are advised to contact the author for the final version of the publication, or visit the DOI to the publisher's website.
- The final author version and the galley proof are versions of the publication after peer review.
- The final published version features the final layout of the paper including the volume, issue and page numbers.

[Link to publication](#)

General rights

Copyright and moral rights for the publications made accessible in the public portal are retained by the authors and/or other copyright owners and it is a condition of accessing publications that users recognise and abide by the legal requirements associated with these rights.

- Users may download and print one copy of any publication from the public portal for the purpose of private study or research.
- You may not further distribute the material or use it for any profit-making activity or commercial gain
- You may freely distribute the URL identifying the publication in the public portal.

If the publication is distributed under the terms of Article 25fa of the Dutch Copyright Act, indicated by the "Taverne" license above, please follow below link for the End User Agreement:

www.tue.nl/taverne

Take down policy

If you believe that this document breaches copyright please contact us at:

openaccess@tue.nl

providing details and we will investigate your claim.

*Two dimensional gas temperature
measurements of fuel sprays in
a high pressure cell.*

Proefschrift

ter verkrijging van de graad van doctor aan de
Technische Universiteit Eindhoven, op gezag van de
rector magnificus, prof.dr.ir. C.J. van Duijn, voor een
commissie aangewezen door het College voor
Promoties in het openbaar te verdedigen
op maandag 19 november om 16.00 uur

door

Miao Yu

geboren te Anhui, China

Dit proefschrift is goedgekeurd door de promotor:

prof.dr. L.P.H. de Goey

Copromotoren:

dr.ir. C.C.M. Luijten

en

dr. N.J. Dam

Copyright©2012 by M. Yu

All rights reserved. No part of this publication may be reproduced, stored in a retrieval system, or transmitted, in any form, or by any means, electronic, mechanical, photocopying, recording, or otherwise, without the prior permission of the author.

This research was financially supported by the Dutch Technology Foundation STW, which is part of the Netherlands Organization for Scientific Research (NWO) and partly funded by the Ministry of Economic Affairs, Agriculture and Innovation (project number 07911).

A catalogue record is available from the Technische Universiteit Eindhoven Library.

ISBN: 978-94-6191-484-2

Cover Design: M. Yu, Y. Chen and HuaMing

Cover: The cover ‘Dragon warrior’ symbolizes the major topic of this thesis. The breath of the dragon represents a fuel spray and the sword of the warrior represents the laser beam which is used to measure the temperature.

Contents

1	Introduction	5
1.1	Motivation	5
1.2	2D temperature distribution in the High Pressure Cell	6
1.3	2D temperature distribution of fuel sprays	7
1.4	Outline of the thesis	8
2	Pre-combustion and cooling process of the High Pressure Cell	13
2.1	Introduction	14
2.2	The High Pressure Cell	14
2.3	Cooling process of pre-combustion residual gas	18
2.4	Conclusions	29
3	Modeling of the temperature distribution in a fuel spray	31
3.1	Motivation	32
3.2	Physical processes in a fuel spray	32
3.3	Phenomenological models of a fuel spray	36
3.4	Comparison with experiments	41
3.5	Conclusions	42
4	Laser diagnostic methods for temperature measurement	45
4.1	Temperature diagnostic specifications	47
4.2	Selection of laser diagnostics for HPC applications	47
4.3	Rayleigh Scattering	48
4.4	Raman Scattering	50
4.5	Laser-induced phosphorescence	51
4.6	Laser-induced fluorescence	56
4.7	Summary	59
5	Temperature measurements of residual gas using BAM-LIP	61
5.1	Introduction	63
5.2	Experimental	64
5.3	Aspects of quantitative measurements	68

5.4	Calibration	76
5.5	Results and discussion	78
5.6	Conclusions	80
6	Gas phase temperature measurements using Toluene LIF	85
6.1	Introduction	87
6.2	Materials/Setups	88
6.3	Aspects of quantitative measurements	93
6.4	Calibration	100
6.5	Results	103
6.6	Conclusions and recommendations	110
7	Conclusions, Recommendations and Outlook	113
7.1	2D temperature distribution in the HPC	113
7.2	2D temperature distribution of fuel sprays	115
7.3	Outlook	116
A	Implementation of the Valencia model	117
B	Toluene LIF Data processing	121

Summary

Premixed charge compression ignition (PCCI) is a promising low-emission combustion concept. By partially mixing the fuel, air and exhaust gas before auto-ignition, the soot and NO_x emissions are lower than for conventional diesel combustion. However, the fundamental aspects of the mixing process of the fuel spray with the ambient air are still not well understood, especially not in terms of the temperature distribution of the fuel/air mixture.

This thesis focuses on the 2D temperature distribution measurement of fuel sprays under conditions relevant to PCCI-mode combustion in heavy-duty Diesel engines. Experiments are performed in the High Pressure Cell (HPC), which simulates engine conditions while providing much better optical accessibility than a real engine. The temperature field which is produced by the pre-combustion technique is also measured, to characterize the ambient condition which the sprays are injected in. Advanced diagnostics are applied to provide detailed information on fuel sprays and the ambient condition, to improve the understanding of the mixing mechanism and its consequences for the combustion process.

Chapter 2 describes the pre-combustion technology of the HPC and the modeling of the cooling process. The analytical modeling is based on experimental observations, assuming that turbulent convection is dominating the cooling process. A natural and a forced convection model are used to estimate the thermal boundary layer thickness and the core temperature in the scenarios without and with fan-mixing, respectively. Without fan-mixing the heat transfer rate decays together with the turbulent kinetic energy. If fan mixing is added, a constant turbulent flow is maintained, that is, the turbulent kinetic energy is constant during the cooling process. The modeling results match experimental results very well. In the first scenario, the core temperature is about 5 – 7% higher than the bulk temperature. In the second scenario the difference is 2 – 6%. These results are reasonable when compared with experiments. The model provides a good estimation for the ambient condition during fuel spray measurements.

In Chapter 5, Laser Induced Phosphorescence (LIP) is chosen to measure the temperature field of the ambient gas prior to fuel injection. The BAM (BaMgAl₁₀O₁₇:Eu)

is chosen as a tracer phosphor for its high signal-to-noise ratio and its capability to survive the pre-combustion. A seeding device to seed the $3\ \mu\text{m}$ solid particles into gaseous flow was designed and implemented, which performed beyond expectation. Particle agglomeration was not observed, probably due to the high shear forces induced. Particle sticking is not a major concern as long as stainless steel tubing is used and Teflon material is avoided. BAM-LIP is excited by a 355 nm YAG laser. Results show that BAM-LIP can be used to measure the temperature field of the residual gas in the HPC below 650 K. The precision of the experiments is better than 30 K at 400 K and 60 K at 650 K. The spatial resolution was estimated to be 3 mm in the plane of the laser sheet and 10 mm along the line of sight, primarily determined by multiple scattering present in the experiments. Temperature field results show that there is a significant temperature gradient in the vertical direction present during the cooling phase in the HPC when the mixing fan is not used. This finding supports the interpretation of the analytical model, which overpredicts the temperature for neglecting the buoyancy effect. However the BAM-LIP method is currently not able to provide 2D temperature distribution prior to fuel injection, due to the lack of signal due to particle falling. Possible improvements have been recommended.

In Chapter 3, the physical processes in a fuel spray, as it is injected into stagnant ambient gas, are explained and two phenomenological spray models are compared in their prediction of temperature distribution in a fuel spray. The major difference between the Versaavel and the Valencia model exists in their assumptions for radial profiles of fuel concentration and velocity. The Versaavel model assumes a top-hat profile while the Valencia model assumes a Gaussian profile, which is observed by averaging multiple injections. Both models predict spray penetration very well, however, they differ considerably in their prediction of the temperature distribution. The Valencia model predicts lower central line temperatures than the Versaavel model.

Laser Induced Fluorescence (LIF) using 10% toluene as a tracer, as described in Chapter 5, is used as a tool to measure 2D temperatures during and after injection of fuel inside the HPC and an optical engine. The error analysis and evaluation of the toluene LIF method was performed on the HPC, while the calibration was performed in the optical engine. The toluene LIF method is capable of measuring temperatures up to 700 K; above that the signal becomes too weak. The precision of the spray temperature measurements is 4% and the spatial resolution is 1.3 mm. Experimental results from the HPC reveal a hot zone in the fully developed spray. Two camera configurations are compared. An opposite side camera setup seems to be beneficial over a one-side setup because it avoids the dichroic beam splitter requirement, but the precision is lower because of different light paths. The toluene LIF method offers a relatively simple and precise way to measure the 2D temperature distribution in fuel sprays. However, several improvements can be done to improve the absolute accuracy, For example using more sensitive camera and applying flat field correction with a light source of the relevant wavelength.

In general, the toluene LIF method is capable of providing 2D temperature information in a fuel spray with 4% precision, which makes it possible to detect the tem-

perature gradients in sprays. The BAM-LIP method could be used in measuring the temperature distribution in a gas-phase environment, where combustible tracers, such as toluene, are not applicable. Both methods might be applied in more applications such as in burners and internal combustion engines.

1.1 Motivation

The internal combustion engine (ICE) has been the most important transportation power source for almost a century. It will remain so in the foreseeable future. The new challenges in the ICE industry are reducing carbon dioxide emission, optimizing combustion properties for renewable fuels and minimizing pollutant emissions. Since the first EURO emission regulation was introduced for heavy duty engines in 1992, the maximum allowed emission of particulate matter has decreased by 97% to 0.01 g/kWh and that of NO_x by 95% to 0.4 g/kWh in the EURO VI norm in 2013.

The pressure of even more stringent regulations has pushed applied research on new combustion strategies. Widely investigated strategies include Homogeneous Charge Compression Ignition (HCCI) [1], Partially Premixed Combustion (PPC) [2], Low Temperature Combustion (LTC) [3] and Premixed Charge Compression Ignition (PCCI) [4, 5]. In general, these strategies share a similar approach: diluting the charge by operating lean or using high amounts of Exhaust Gas Recirculation (EGR) to achieve a lower equivalence ratio and local temperature than conventional diesel combustion [6]. For example, PCCI is realized by partially mixing fuel, air and exhaust gas before auto-ignition. In these new combustion strategies, the temperature field after fuel/air mixing, but before auto-ignition, is of critical importance to engine efficiency and emission formation.

However, the fundamental aspects of the mixing process of the fuel spray with the ambient air are still not well understood, especially in terms of the resulting temperature distribution of the fuel/air mixture. For spray measurements, the constant volume High Pressure Cell (HPC) is an established tool to simulate engine conditions, while providing much better optical accessibility than a real engine. On the other hand, new diagnostics and refinement of existing diagnostics are required to meet the new challenges. Applying advanced diagnostics in a HPC can provide detailed information on fuel sprays, to improve the understanding of the mixing mechanism and its consequences for the combustion process. This is what the present thesis is about.

1.2 2D temperature distribution in the High Pressure Cell

For fundamental research on diesel fuel sprays under engine-like temperatures and gas densities, the optically accessible constant-volume high pressure cell is a well-established experimental environment [7–10]. An international cooperation network of HPCs has been recently established [11, 12]. HPCs have been widely used for measuring spray penetration and liquid length [9, 13], temperature [10], equivalence ratio [14], spray radial profile [15], spray combustion [16, 17] and injector technology [18].

HPCs often work with the so-called pre-combustion technique [7]. Engine conditions towards the end of the compression stroke are simulated by burning a premixed charge of gaseous fuel in which O_2 is present. The walls of the cell are heated to simulate realistic wall temperatures and prevent water condensation on the windows. The composition of the premixed charge determines the chemical composition of the environment into which the spray will be injected. A lean pre-combustion is required for research on burning sprays. A stoichiometric to slightly rich pre-combustion can be used if a non-reactive spray is to be investigated. The ignition of the pre-charge creates a rapid rise of pressure and temperature to values well above engine-like conditions. After the pre-combustion, pressure and temperature decrease due to heat loss at the walls. Once the desired conditions are reached the fuel spray is injected.

The spray is always injected towards the core of the HPC. Although we can use a pressure sensor to monitor the bulk average temperature of the cell, the core temperature is still more relevant to the spray behavior. The temperature distribution in the cooling down phase of a cell was measured by Naber [13], which shows that the core temperature T_c is 4% - 8% higher than the mass averaged (or bulk) temperature T_b . The core temperature was measured with a thermocouple and bulk temperature was deduced from the pressure sensor reading. Similar results are reported by other researchers [12, 19].

However, the controlling mechanisms of the cooling process inside the cell are still unclear. The experimental investigation and further modeling of the cooling process is essential to obtain a deeper understanding and a better control of the temperature gradients present in the gas mixture after pre-combustion. The modeling of the cooling process is presented in this work. The experimental investigation of the 2D temperature distribution in the cooling process of a HPC is also attempted using laser-induced phosphorescence (LIP).

LIP measurements are based on the fact that, when excited e.g. by a laser, thermographic phosphors (TP) will emit red-shifted light carrying local temperature information. LIP has been an established method in surface temperature measurement [20–23]. If the TP is selected properly, LIP measurements bring advantages of high accuracy, high signal yield and insensitivity to oxygen quenching [24, 25]. For this reason, LIP has been extended to gas phase measurement because it is of great interest to the combustion industry [26, 27]. For gas-phase application of LIP, the seeding of TP particles has been a concern since the first attempt of Hasegawa [26], because the optical access is often blocked by the particles sticking onto surfaces. Building a better seeding device is one of the topics of this work. Other issues, such

as the effect of ‘multiple scattering’, are addressed as well.

1.3 2D temperature distribution of fuel sprays

The two-dimensional temperature distribution inside fuel sprays is a key parameter for new combustion strategies. However, non-intrusive accurate 2D temperature measurements under high temperature engine conditions have always been a challenge. Rayleigh Scattering suffers from boundary scattering and the coupling of temperature/concentration distribution. Very special methods are needed to suppress these effects [14, 28]. Raman Scattering suffers from weak signal. Many of the tracers of laser-induced fluorescence (LIF) also have weak signal at high temperature.

Various attempts to measure the fuel temperature distribution in IC engines have been made. Acetone and 3-pentanone have been used to detect fuel temperature in HPCs and optical engines [29–31]. An overview of tracer-LIF diagnostics has been published by Schulz et al. [32]. However, reports of the measurement of temperature distribution in fuel sprays are very limited.

Recent research suggests that toluene laser-induced fluorescence (LIF) is an appropriate technique for measuring fuel spray temperatures [10, 33]. Toluene has a few advantages over other tracers: it has a high fluorescence quantum yield, a relatively large red shift as function of temperature and a lower toxicity than e.g. benzene [32, 34]. Toluene LIF is further explored in this work because of the promising outlook of the technique and its relatively modest equipment requirements. A major disadvantage of toluene LIF is the decrease of its effective fluorescence lifetime as function of temperature, which decreases the total amount of fluorescence signal with increasing temperature [35].

In our research, toluene LIF is used as a tool to measure temperatures during and after injection of fuel inside the HPC and an optical engine. The error analysis and evaluation of the toluene LIF method was performed on the HPC, while the calibration was performed in the optical engine. A Large-Eddy Simulation (LES) of the same spray is used to interpret the experimental observations via the calculated velocity field.

Modeling can help to understand the physical processes and analyse the influence of injection parameters on the spray characteristics. In particular, a phenomenological model simplifies complex phenomena by capturing the major physical processes and ignoring the minor ones, combining physical insight with computational simplicity. They also allow some (cautious) extrapolation, which enables parameter studies over wider parameter ranges (model-based extrapolation is far safer than using e.g. polynomials).

In this thesis, two types of phenomenological spray models, the Versaevel [36] and Valencia models [37] are summarized and compared. The major difference between the two models is the assumption of radial profiles for fuel mass fraction and velocity. The Versaevel model assumes a uniform profile while the Valencia model assumes a Gaussian profile. The difference leads to different predictions of the temperature distribution. The toluene-LIF measurement results are used to evaluate the performance of the two models.

1.4 Outline of the thesis

The scope of this thesis includes two topics: 2D temperature distribution of the pre-combustion residual gas in the High Pressure Cell is addressed in Chapter 2, 4 and 5. Chapter 2 describes the pre-combustion technology of the HPC and the modeling of the cooling process. The requirements of temperature measurement and the selection of laser diagnostics are presented in Chapter 4. Chapter 5 focuses on the development of the LIP method to measure the 2D temperature distribution in the HPC.

The second topic, 2D temperature distribution in fuel sprays, is the subject of Chapter 3 and 6. Chapter 3 describes the physical processes of a fuel spray and compares the phenomenological spray models in terms of temperature prediction. Chapter 6 presents the development of the toluene-LIF method in the HPC and an optical engine. Chapter 7 draws conclusions regarding the measurement of temperature distributions in the HPC and in a fuel spray.

Bibliography

- [1] M. Christensen, A. Hultqvist, and B. Johansson. Demonstrating the multi fuel capability of a Homogeneous Charge Compression Ignition engine with variable compression ratio. *SAE Technical Paper*, 1999-01-3679, 1999.
- [2] C. Noehre, M. Andersson, B. Johansson, and A. Hultqvist. Characterization of Partially Premixed Combustion. *SAE Technical Paper*, 2006-01-3412, 2006.
- [3] J.E. Dec. Advanced compression-ignition engines - understanding the in-cylinder processes. *Proc. Combust. Inst.*, 32 issue 2:2727–2742, 2009.
- [4] D.L. Flowers, S.M. Aceves, and A. Babajimopoulos. Effect of charge - non-uniformity on heat release and emissions in PCCI engine combustion. *SAE Technical Paper*, 2006-01-1363, 2006.
- [5] W.L. Hardy and R.D. Reitz. A study of the effects of high EGR, high equivalence ratio, and mixing time on emissions levels in a heavy-duty diesel engine for PCCI combustion. *SAE Technical Paper*, 2006-01-0026, 2006.
- [6] K. Akihama, Y. Takatori, K. Inagaki, S. Sasaki, and A.M. Dean. Mechanism of the smokeless rich diesel combustion by reducing temperature. *SAE Technical Paper*, 2001-01-0655, 2001.
- [7] D.C. Oren, S. Wahiduzzaman, and C.R. Ferguson. A diesel combustion bomb: Proof of concept. *SAE paper*, 841358, 1984.
- [8] D.L. Siebers. Ignition delay characteristics of alternative diesel fuels: Implications on Cetane Number. *SAE Technical Paper 852102*, 1985.
- [9] R.S.G. Baert, P.J.M. Frijters, L.M.T. Somers, C.C.M. Luijten, and W. de Boer. Design and operation of a high pressure, high temperature cell for HD diesel spray diagnostics: Guidelines and results. *SAE Technical Paper*, 2009-01-0649, 2009.

-
- [10] G. Tea, G. Bruneaux, J.T. Kashdan, and C. Schulz. Unburned gas temperature measurements in a surrogate diesel jet via two-color toluene-LIF imaging. *Proceedings of the Combustion Institute*, 33(1):783 – 790, 2011. ISSN 1540-7489.
- [11] E. Hawkes. Model comparisons: n-heptane session. *ECN1 workshop*, <http://www.sandia.gov/ecn/>, 2011.
- [12] L.M. Pickett, C.L. Genzale, G. Bruneaux, L.M. Malbec, L. Hermant, C. Christiansen, and J. Schramm. Comparison of diesel spray combustion in different high-temperature, high-pressure facilities. *SAE Int. J. Engines*, 2010-01-2106: 156–181, 2010.
- [13] J.D. Naber, D.L. Siebers, S.S. Di Julio, and C.K. Westbrook. Effects of natural gas composition on ignition delay under diesel conditions. *Combustion and Flame*, 99(2):192 – 200, 1994.
- [14] A.I. Cherman and L.M. Pickett. Quantitative mixing measurements in a vaporizing diesel spray by Rayleigh imaging. *SAE Technical Paper*, 2007-01-0647, 2007.
- [15] G. Bruneaux. Liquid and vapor spray structure in high-pressure common rail diesel injection. *Atomization and Sprays*, 11:105, 2001.
- [16] J.E. Dec. A conceptual model of DI diesel combustion based on laser-sheet imaging. *SAE Technical Paper*, 970873, 1997.
- [17] B. Higgins and D. Siebers. Measurement of the flame lift-off location on DI diesel sprays using OH chemiluminescence. *SAE Technical Paper*, 2001-01-0918, 2001.
- [18] R. Payri, F.J. Salvador, J. Gimeno, and J. de la Morena. Effects of nozzle geometry on direct injection diesel engine combustion process. *Applied Thermal Engineering*, 29(10):2051 – 2060, 2009. ISSN 1359-4311.
- [19] R. P. Durrett, D. C. Oren, and C. R. Ferguson. A multidimensional data set for diesel combustion model validation: I - initial conditions, pressure history and spray shapes. *SAE Technical Paper Series*, (872087), 1987.
- [20] S.W. Allison and G.T. Gilles. Remote thermometry with thermographic phosphors: Instrumentation and applications. *Rev. Sci. Instrum.*, 68(7):2615, 1997.
- [21] J. Brübach, J. Zetterberg, A. Omrane, Z.S. Li, M. Aldén, and A. Dreizler. Determination of surface normal temperature gradients using thermographic phosphors and filtered Rayleigh scattering. *Applied Physics B: Lasers and Optics*, 84: 537–541, 2006. ISSN 0946-2171.
- [22] A.L. Heyes, S. Seefeldt, and J.P. Feist. Two-colour phosphor thermometry for surface temperature measurement. *Optics & Laser Technology*, 38(4 - 6):257 – 265, 2006.
- [23] M. Aldén, A. Omrane, M. Richter, and G. Särner. Thermographic phosphors for thermometry: A survey of combustion applications. *Progress in Energy and Combustion Science*, 37(4):422 – 461, 2011. ISSN 0360-1285.

-
- [24] G. Särner. *Laser-Induced Emission Techniques for Concentration and Temperature Probing in Combustion*. PhD thesis, Lund University, 2008.
- [25] J. Brübach, A. Dreizler, and J. Janicka. Gas compositional and pressure effects on thermographic phosphor thermometry. *Measurement Science and Technology*, 18(3):764, 2007.
- [26] R. Hasegawa, I. Sakata, H. Yanagihara, B. Johansson, A. Omrane, and M. Aldén. Two-dimensional gas-phase temperature measurements using phosphor thermometry. *Applied Physics B: Lasers and Optics*, 88, 2007.
- [27] A. Omrane, P. Petersson, M. Aldén, and M.A. Linne. Simultaneous 2D flow velocity and gas temperature measurements using thermographic phosphors. *Applied Physics B: Lasers and Optics*, 92:99–102, 2008.
- [28] D. Hoffman, K.-U. Münch, and A. Leipertz. Two-dimensional temperature determination in sooting flames by filtered Rayleigh scattering. *Opt. Lett.*, 21(7):525–527, Apr 1996.
- [29] F. Grossmann, P. B. Monkhouse, M. Ridder, V. Sick, and J. Wolfrum. Temperature and pressure dependences of the laser-induced fluorescence of gas-phase acetone and 3-pentanone. *Applied Physics B: Lasers and Optics*, 62:249–253, 1996. ISSN 0946-2171.
- [30] M.C. Thurber, F. Grisch, and R.K. Hanson. Temperature imaging with single- and dual-wavelength acetone planar laser-induced fluorescence. *Opt. Lett.*, 22(4):251–253, 1997.
- [31] S. Einecke, C. Schulz, and V. Sick. Measurement of temperature, fuel concentration and equivalence ratio fields using tracer LIF in IC engine combustion. *Applied Physics B: Lasers and Optics*, 71:717–723, 2000. ISSN 0946-2171.
- [32] C. Schulz and V. Sick. Tracer-LIF diagnostics: quantitative measurement of fuel concentration, temperature and fuel/air ratio in practical combustion systems. *Progress in Energy and Combustion Science*, 31(1):75 – 121, 2005. ISSN 0360-1285.
- [33] J. Mannekutla, A. van Vliet, R. Klein-Douwel, N.J. Dam, and H. ter Meulen. The temperature field just before combustion in a diesel engine. *European Combustion meeting*, 2011.
- [34] K. Mohri, M. Luong, G. Vanhove, T. Dreier, and C. Schulz. Imaging of the oxygen distribution in an isothermal turbulent free jet using two-color toluene LIF imaging. *Applied Physics B: Lasers and Optics*, 103:707–715, 2011. ISSN 0946-2171.
- [35] W. Koban, J.D. Koch, R.K. Hanson, and C. Schulz. Toluene LIF at elevated temperatures: implications for fuel air ratio measurements. *Applied Physics B: Lasers and Optics*, 80:147–150, 2005. ISSN 0946-2171.

-
- [36] P. Versaevel, P. Motte, and K. Wieser. A new 3D model for vaporizing diesel sprays based on mixing-limited vaporization. *SAE Tech. Paper 2000-01-0949*, 2000.
- [37] J.V. Pastor, J.J. López, J.M. García, and J.M. Pastor. A 1D model for the description of mixing-controlled inert diesel sprays. *Fuel*, 87:2871–2885, 2008.

Pre-combustion and cooling process of the High Pressure Cell

In the High Pressure Cell (HPC), the pre-combustion technique is used to simulate diesel engine conditions: pressure, temperature and ambient gas composition. In this chapter we analyze the cooling process that is initiated by pre-combustion in the HPC. This is important for experimental research connected to spray combustion in Diesel engines. The analysis is based on experimental observations and analytical modeling.

We consider two scenarios: with and without forced mixing by a rotating fan. Without forced mixing, turbulent convective heat transfer is the dominant factor in the heat transfer at the cell walls. The modeled temperature curve matches the experimental results when assuming that the decay rate of turbulent kinetic energy is proportional to the 1.5th power of the turbulent kinetic energy itself; it does not depend on the density and composition. In the second scenario, the mixing fan creates a constant turbulent flow inside the HPC. Comparison with experimental results confirms that the self-decaying mechanism doesn't apply anymore. Instead, the turbulent flow created by the mixing fan dominates convective cooling.

For the two scenarios, the thermal boundary layer thicknesses and the differences between core temperature and bulk averaged temperature are analyzed. Without fan mixing, the core temperature is about 5 - 7% higher than the bulk temperature. With fan mixing, the difference is only 2 - 6%, which matches well with measurement results.

Publication of this chapter is in preparation.

2.1 Introduction

For fundamental research on diesel fuel sprays under engine-like temperatures and gas densities, the optically accessible constant volume cell is a well-established experimental environment [1]. Engine conditions towards the end of the compression stroke are simulated by burning a lean pre-charge of gaseous fuel, and the walls of the cell are heated up electrically to simulate realistic wall temperatures. This is the so-called pre-combustion technique [1]. At Eindhoven University of Technology, a similar setup, the HPC, has been built recently, a detailed description can be found in Section 2.2. A clear understanding of the pre-combustion process is essential for simulating engine-like conditions. The ignition of a combustible mixture (with a typical composition as presented in Table 2.1) initially causes a rapid rise of pressure and temperature to values well above engine-like conditions at the moment of fuel spray injection. The fuel spray is injected into an ambient gas that consists of the residual gas of the pre-combustion. By adjusting the composition of the premixed charge, the composition of this residual gas can be varied. A lean pre-combustion is required for research of burning sprays. A stoichiometric to slightly rich pre-combustion can be used if a non-reactive spray is investigated. After the pre-combustion, pressure and temperature decrease due to heat loss at the walls. Once the desired conditions are reached the diesel fuel spray is injected.

To determine the right moment of injection, the time evolution of the average pressure is recorded (Fig. 2.1). From this pressure, the bulk-averaged temperature is straightforwardly obtained. However, the controlling mechanism of the cooling process inside the cell is still unknown. The experimental investigation and further modeling of the cooling process is essential to obtain a deeper understanding and a better control of the temperature gradients present in the gas mixture after pre-combustion. These are needed to establish unambiguous boundary conditions for the injected fuel sprays, which is one of the efforts of the Engine Combustion Network [2].

Preliminary investigations [3] have shown that turbulent convection dominates the cooling in early phases of the cooling process; later, natural convection might take over, as velocities become smaller due to turbulence decay. This initial turbulence arises from two sources: one is a mixing fan that is used to improve homogeneity of the mixture before pre-combustion; the other is the creation of large temperature gradients by the pre-combustion flame itself, which contributes to the initial turbulence.

In this chapter we discuss the modeling of the cooling phase of pre-combustion in the HPC. The HPC is described in Section 2.2. In Section 2.3, we describe the cooling model based on turbulent heat transfer and show that the average temperature decay can be correlated to the decay of turbulent kinetic energy. The difference between the core-zone temperature and the bulk-averaged temperature is also analyzed.

2.2 The High Pressure Cell

The core of the HPC is a cubically shaped combustion chamber produced through spark erosion inside a stainless steel cube. The holes on each side of the combustion chamber can be fitted either with a window or with a flat metal plug. The HPC is equipped with sub-systems for heating & cooling, fuel injection, gas supply, controlling

Table 2.1: Typical initial gas composition in the HPC for non-reacting spray conditions. The total density is 12.4 kg/m^3 , and can be scaled by adjusting all components proportionally.

Reactants	O ₂ [mg]	C ₂ H ₂ [mg]	N ₂ [mg]	Ar [mg]		
	2067	924	11135	1457		
Products	O ₂ [mg]	C ₂ H ₂ [mg]	N ₂ [mg]	Ar [mg]	CO ₂ [mg]	H ₂ O [mg]
	0	252.2	11135	1457	2273.7	465.1

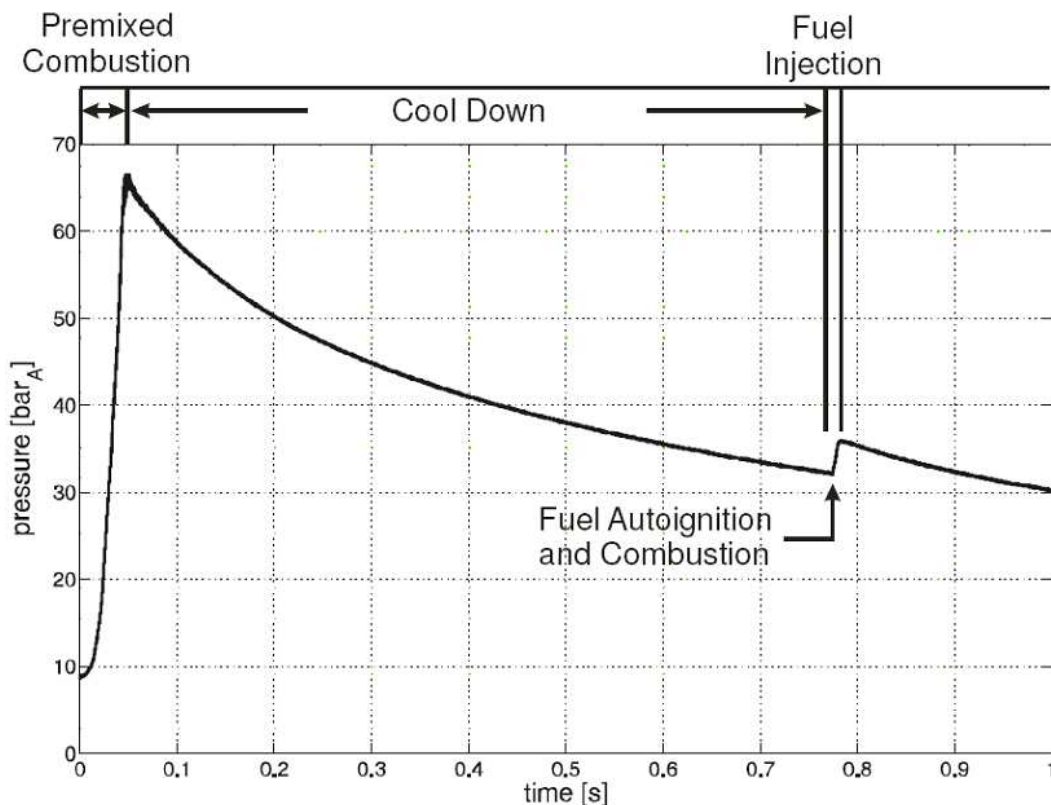


Figure 2.1: Principle of the pre-combustion technique [4].

& data acquisition and optical diagnostics. A schematic drawing of the HPC and auxiliary equipment is shown in Fig. 2.2. The heating & cooling system is not shown. A photo of the HPC is shown in Fig. 2.3. A front view of a middle section of the HPC is shown in Fig. 6.3, in which the mixing fan and the pressure sensors are not shown, because they are installed on the corners.

The main properties of the HPC are listed in Table 6.3. A more detailed description is given in a recent paper of Baert et al. [4]. The laser diagnostic systems will be described in Chapters 4 - 6.

The gas supply system is based on four Mass Flow Controllers, which enable us to fill the pure gases one by one to prepare the premixed charge inside the HPC. The filling process is monitored by the gas pressure sensor. A fan is used to enhance mixing. We

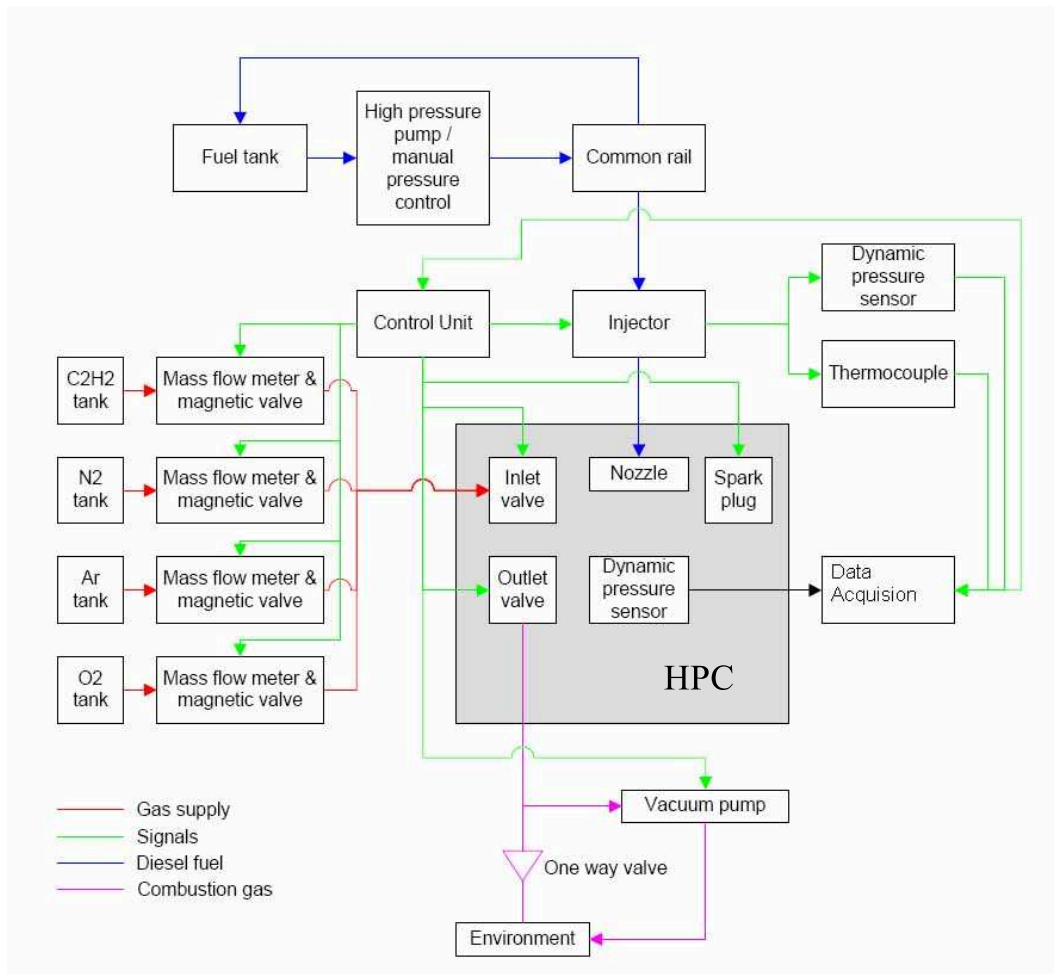


Figure 2.2: Schematic drawing of the HPC system.

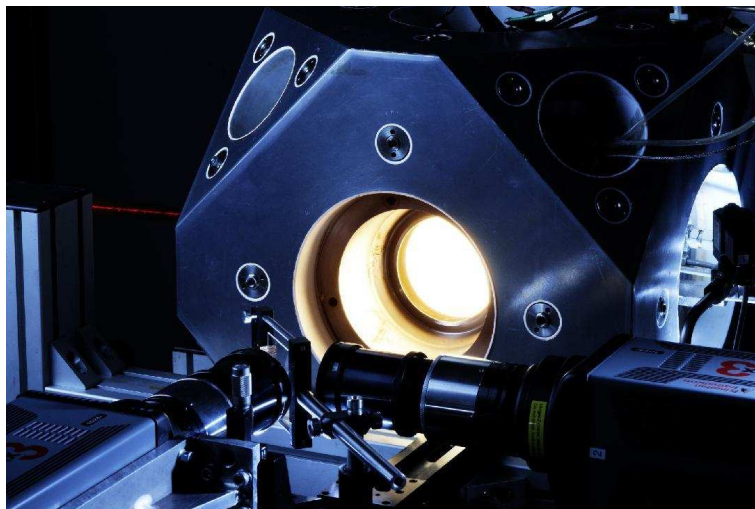


Figure 2.3: A photo of the HPC.

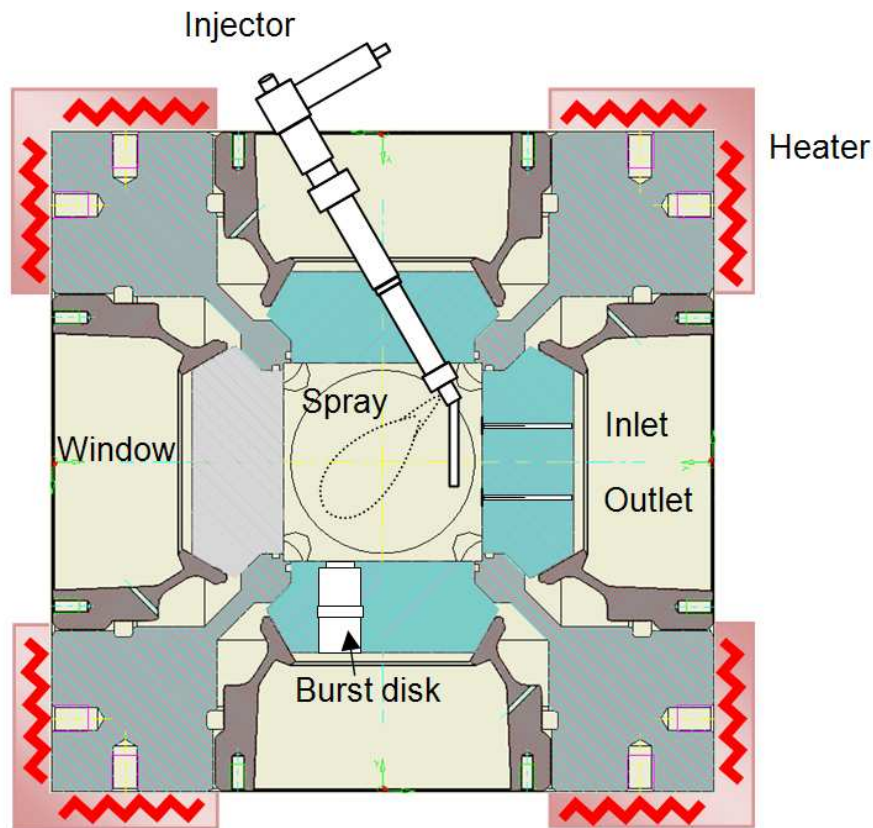


Figure 2.4: Vertical cross section of the HPC.

use C_2H_2 , O_2 , N_2 and Ar to form a mixture, which, after pre-combustion, produces the same density, O_2 mass fraction and heat capacity as the desired engine condition. For safety reasons, C_2H_2 is filled in first, because it is unstable above 2 bar. The oxygen is filled in last, to make sure that its mole fraction is never too high in the mixture, to prevent detonation. The pre-combustion is spark-ignited. After that, typically in about 1 - 2 seconds, the residual gas of pre-combustion cools down to the desired temperature, and the fuel is injected. The optical diagnostic system is also synchronized with the injection.

A typical procedure to do an experiment is

1. Heat up the HPC for 1.5 hours so the setup is in thermal equilibrium;
2. Evacuate the HPC;
3. Prepare the gases for the premixed charge;
4. Prepare the fuel injection system;
5. Ignition, fuel injection and data acquisition;
6. Flush the HPC;
7. Repeat from 2 as desired.

Table 2.2: The parameters of the HPC

Basic parameters	
Shape of the chamber	108×108×108 mm ³
Window size	50 mm thick, 100 mm diameter
Maximum pressure	130 bar (quartz) or 300 bar (sapphire)
Spark plug	EYQUEM EQA66
Ignition system	Delphi coil-near plug (19005218)
Fan speed	about 3000 rev/min, can varies a lot
Fan diameter	45 mm
Heating and Cooling system	
Wall temperature	293 K - 473 K
Fuel temperature	313 K - 423 K
Injector holder temperature	333 K
Temperature of the piëzo-electric sensor	Cooled but not specified
Fuel supply system	
Injector	Delphi single-nozzle, TiN coated
Common rail pressure	300 bar - 2000 bar
Injection duration	1.5 ms - 5 ms
Injector nozzle	150 μ m
C_d	0.86 (at 800 bar)
C_m	0.77 (at 800 bar)
Controlling and data acquisition system	
Hardware	TUeDACS/3 system
Software	LabWindows/CVI and Matlab
Data acquisition rate	100 kHz
Gas pressure sensor	Piëzo-resistive, Druck PMP 4070 (0-70 bar)
Injection pressure sensor	Piëzo-resistive, Kistler 4067A5000
Pre-combustion pressure sensor	Kistler 6041 AU20 (0-250 bar)

2.3 Cooling process of pre-combustion residual gas

The cooling process of pre-combustion residual gas is introduced in this section. An analytical model was developed to describe the cooling process, which matches the experimental results very well. The difference between the core-zone temperature and the bulk averaged temperature is also discussed in Section 2.3.3.

2.3.1 Bulk averaged temperature without fan-mixing

A typical decay curve of bulk averaged temperature is shown in Fig. 2.5. It is obtained from the recorded pressure curve using the ideal gas law at the appropriate mass density and composition. The initial cell condition for the measurement of this curve is as listed in Table 2.1.

For constant statistics of the flow inside the cell, e.g. stagnant or constant turbulence (no decay), constant thermal conductivity and constant heat capacity, the tempera-

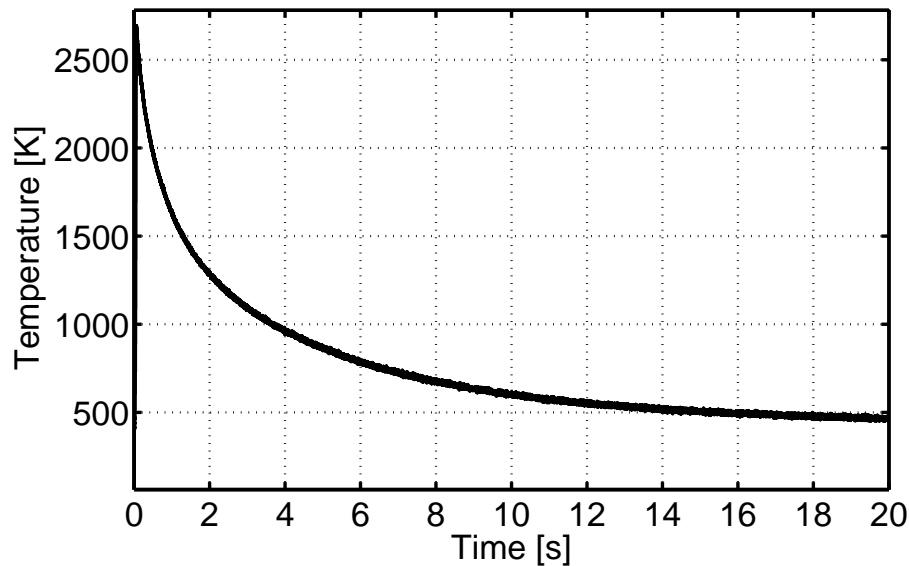


Figure 2.5: Typical bulk averaged temperature decay curve after pre-combustion in the cell. (See Table 2.1 for the initial gas composition.)

ture decay rate is proportional to the temperature difference. One would expect the temperature to decay exponentially in time.

As the result of strongly turbulent combustion, the initial turbulence will determine the convective heat transfer near the wall. However, the turbulence will decay with time due to viscous dissipation, which partly contributes to the decrease of the heat transfer coefficient itself. Since the total turbulent kinetic energy of the gas is much smaller than the energy transfer from cooling, it is reasonable to assume that the heat generated by viscous dissipation is negligible. The gas composition is considered to be uniform. The mass in the cell, m , remains constant. The heat capacity c_v and thermal conductivity λ vary with temperature. Because of the very large ratio of the heat capacity of the enclosing material compared to the gas inside the cell we may assume a constant wall temperature T_w . The heat transfer coefficient h is given by

$$h = \frac{\lambda Nu}{L}, \quad (2.1)$$

where $L = 0.108$ m is a characteristic length, the length of the edge of the cell. The averaged Nusselt number, Nu , by definition, is the dimensionless perpendicular gradient of temperature on the surface. So the average temperature in the volume, T_b , is governed by

$$dT_b = \frac{hA}{mc_v}(T_w - T_b)dt = \frac{\lambda Nu}{L} \cdot \frac{6L^2}{mc_v}(T_w - T_b)dt = \frac{6\lambda Nu L}{mc_v}(T_w - T_b)dt, \quad (2.2)$$

where $c_v(T)$ of the mixture (Table 2.1) is obtained from the DIPPR database [5]. The thermal conductivity $\lambda(T)$ is calculated by Chung's method [6, 7]. A is the total internal surface area of the combustion chamber.

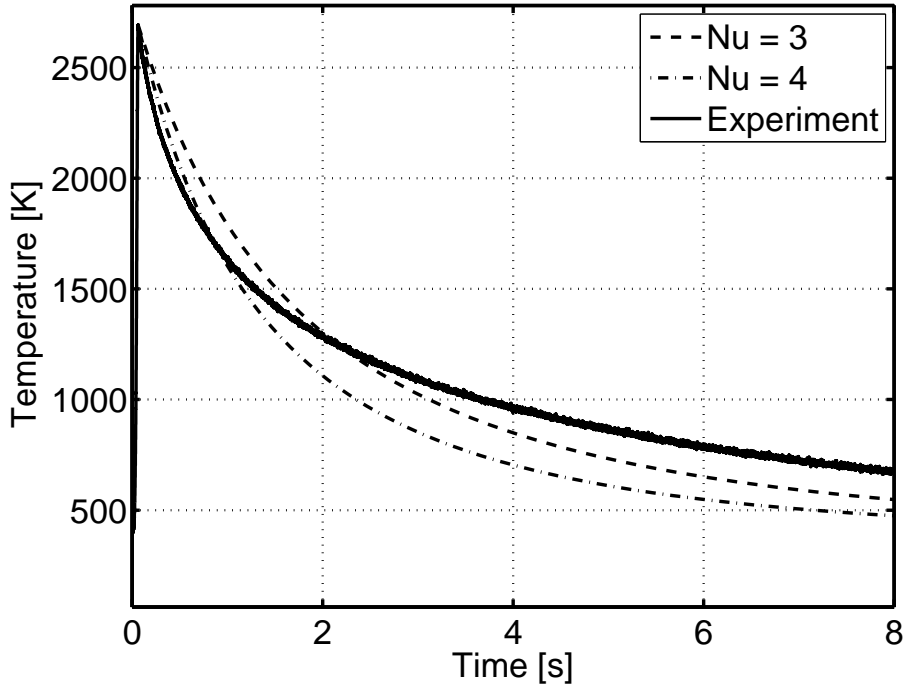


Figure 2.6: Cooling down determined by a constant turbulent kinetic energy.

In Fig. 2.5, we show a typical temperature decay as derived from the pressure trace in the high pressure cell. The measurement shows a temperature decay starting at T_0 of 2700 K towards $T_\infty = T_w = 380$ K. Eq. (2.2) is solved numerically and plotted together with the experimental results in Fig. 2.6, assuming a constant Nusselt number. A larger Nu transports energy faster, thus results in a faster temperature decrease. However, the model results do not approach experiments very well.

In practice, Nu highly depends on the geometry of the surface and the flow field structure. For the experiments in the HPC, the geometry is the same and turbulence dominates the convection. So Nu is assumed to depend on the turbulent kinetic energy k when k is high enough. As we stated, the flow inside the HPC is initialized by pre-combustion and naturally cools down from the resulting temperature difference. For natural convection in a closed cell, Nu is proportional to the 1/3 power of the Rayleigh number: $Nu \propto Ra^{1/3} \propto Re^{2/3} Pr^{1/3}$ [8], in which Re is the Reynolds number and the Prandtl number $Pr = 0.7$ is constant for diatomic gases. For CO_2 the Pr value is also very close to 0.7 in the relevant pressure and temperature. The mass fraction of H_2O is very small. So it is reasonable to use $Pr = 0.7$. For local values, Re changes with $k^{1/2}$, where k is defined as $k = \frac{1}{2}u'_i u'_i$, ($i = x, y, z$). u'_i is the velocity in one of the directions. In short, we have:

$$Nu \propto Ra^{1/3} \propto Re^{2/3} \propto k^{1/3}. \quad (2.3)$$

So we assume:

$$Nu = C_1 k^{1/3}, \quad (2.4)$$

where C_1 is a proportionality constant. If the initial turbulence level is sufficiently high, buoyancy effects can be neglected till the initial turbulence decays significantly.

It can be shown that for isotropic turbulence in an enclosed volume, the decay rate of kinetic energy is related to the kinetic energy itself by [9]:

$$dk/dt = -C_2 k^{3/2}, \quad (2.5)$$

where C_2 indicates the decay constant. After integration, we end up with a kinetic energy:

$$k(t) = \frac{1}{\left(\frac{C_2}{2}t + \frac{1}{\sqrt{k_0}}\right)^2}. \quad (2.6)$$

With this equation, and using Eq. (2.4), the governing equation Eq. (2.2) becomes

$$dT_b = \frac{6C_1 L \lambda}{m c_v \left(\frac{C_2}{2}t + \frac{1}{\sqrt{k_0}}\right)^{2/3}} (T_w - T_b) dt, \quad (2.7)$$

and the solution for the average temperature as a function of time is again numerically calculated and plotted in Fig. 2.7. The values of C_2 , k_0 and C_1 are coupled. For simplicity, we take $C_1 = 1$ (s/m)^{2/3} here. The value of k_0 and C_2 are determined accordingly. In practice, k_0 can be experimentally obtained and the values of C_1 and C_2 can be determined. From empirical fit to the measurement, we take the coefficients $k_0 = 104$ m²/s² and $C_2 = 0.19$ m⁻¹. Larger C_2 results in faster decay of k and thus slower temperature decrease. The error is less than 50 K over the relevant period of time. For comparison, the curve with $C_2 = 0.25$ m⁻¹ is also plotted. After 7 seconds, the model tends to overpredict the temperature. That is probably because the natural convection effect is not considered in the model, which takes some time to build up and then starts to play an important role in the heat transfer. So the model underestimates the heat transfer rate by not considering the buoyancy effect in the later phase, when normally the injection has already finished.

Two other conditions of pre-combustion cooling rate are also modeled and compared with experimental data in Fig. 2.8 and Fig. 2.9. All three experimental conditions are listed in Table 2.3. The three cases are different in density and composition, so the initial turbulent kinetic energy k_0 is different. But the interesting phenomenon is that the decay coefficients C_2 , in three cases are all comparable. This indicates that the decay rate of turbulence is not affected by the density and composition of the mixture.

Table 2.3: Summary of the conditions of the pre-combustion residual gas of the five cooling cases. Fan-on cases are discussed in section 2.3.2

	O ₂	C ₂ H ₂	N ₂	Ar	CO ₂	H ₂ O	density	k_0	C_2	Fan
	[mg]	[mg]	[mg]	[mg]	[mg]	[mg]	[kg/m ³]	[m ² /s ²]	[m ⁻¹]	
1	0	252	11135	1457	2274	465	12.4	104	0.19	Off
2	2323	0	6396	1181	1848	378	9.6	450	0.15	Off
3	1228	0	3341	645	894	183	5.0	125	0.20	Off
4	179	0	18799	2528	3652	747	21	2460	-	On
5	123	0	5553	735	1070	219	6.1	512	-	On

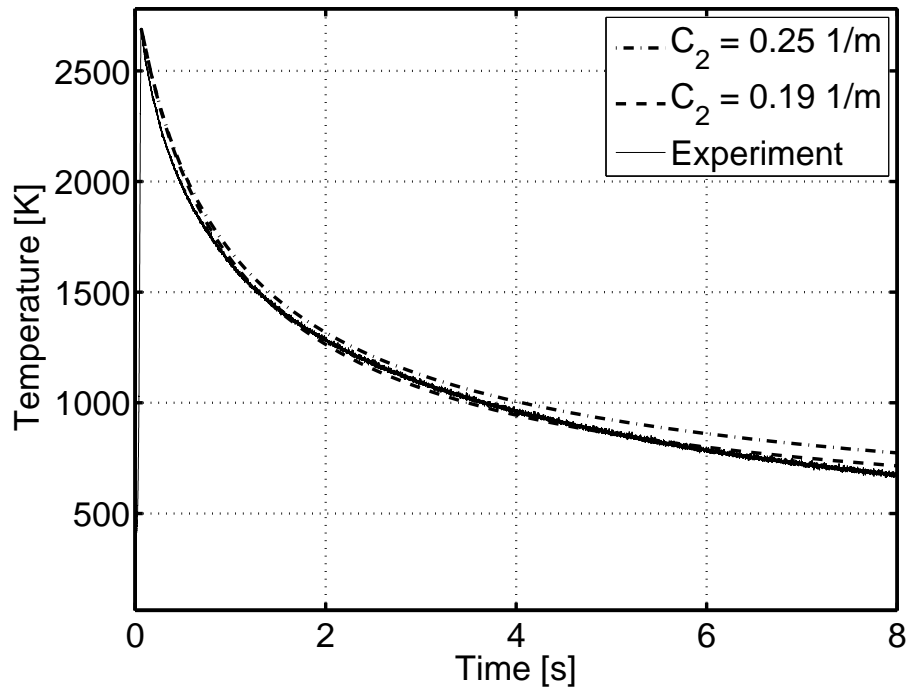


Figure 2.7: Cooling down determined by the decaying turbulent kinetic energy (case 1).

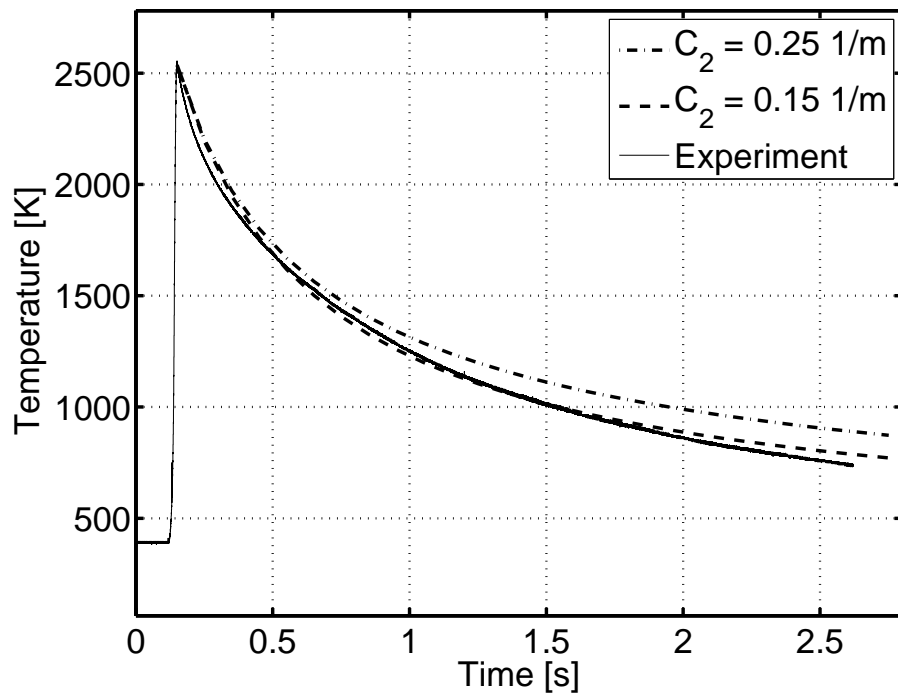


Figure 2.8: Cooling down determined by the decaying turbulent kinetic energy (case 2).

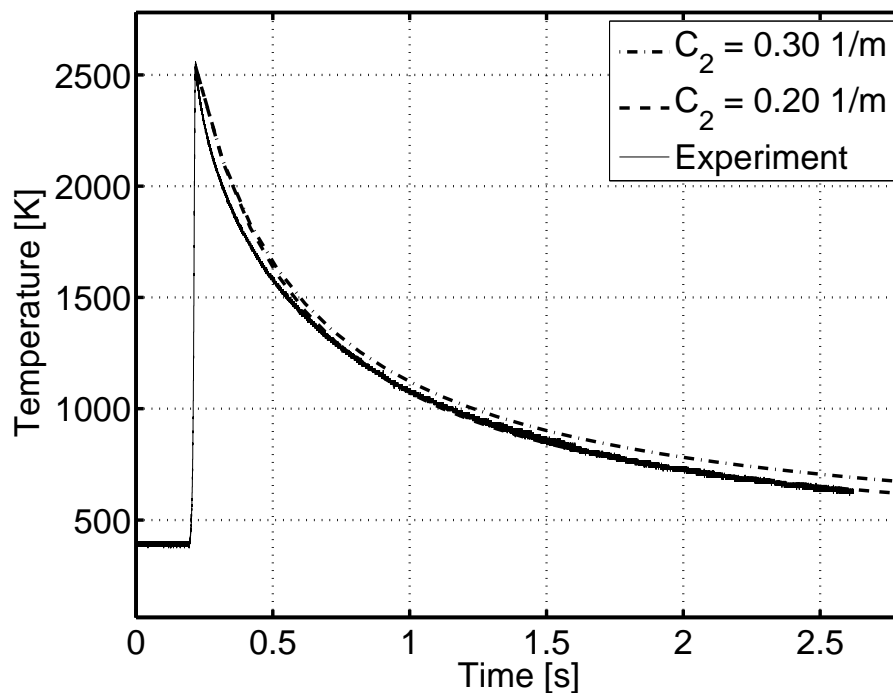


Figure 2.9: Cooling down determined by the decaying turbulent kinetic energy (case 3).

2.3.2 Bulk averaged temperature with fan-mixing

In most of the experiments, the mixing fan is turned on to obtain a uniform temperature field. In this scenario, the turbulence is induced by both pre-combustion and the fan. A turbulent flow with constant turbulent kinetic energy k is driven by the mixing fan, so the self decaying mechanism of k does not apply any more.

To evaluate the contribution of the two sources of turbulent kinetic energy, two kinds of assumptions are compared in Fig. 2.10 (case 4). Firstly by assuming that k is the combination of partly constant and partly decaying turbulent kinetic energy, the dashed curve is plotted. For the decaying part, $k_0 = 1460 \text{ m}^2/\text{s}^2$ is chosen, based on Table 2.3. On the other hand, by assuming that the mixing fan is dominating the flow inside the HPC, which means k is constant, a dashed curve is plotted. For both curves, the total initial turbulent kinetic energy is $2460 \text{ m}^2/\text{s}^2$. It is clear that assuming a constant k matches the experiments better than assuming a combination. The same conclusion can also be drawn for case 5, while assuming $k_0 = 512 \text{ m}^2/\text{s}^2$. The influence of Nusselt number ($Nu = C_1 k_0^{1/3}$) is also compared in Fig. 2.11 and Fig. 2.12. As before, a smaller Nu leads to a slower temperature decay.

2.3.3 The core temperature

As indicated in Fig. 6.3, the spray is always injected towards the core of the HPC. Although we can use a pressure sensor to monitor the bulk average temperature of the cell, the core temperature is still more relevant to the spray behavior. The temperature distribution in the cooling down of a cell was measured by Naber [10], who showed that the core temperature T_c is 4% - 8% higher than the mass averaged (or bulk)

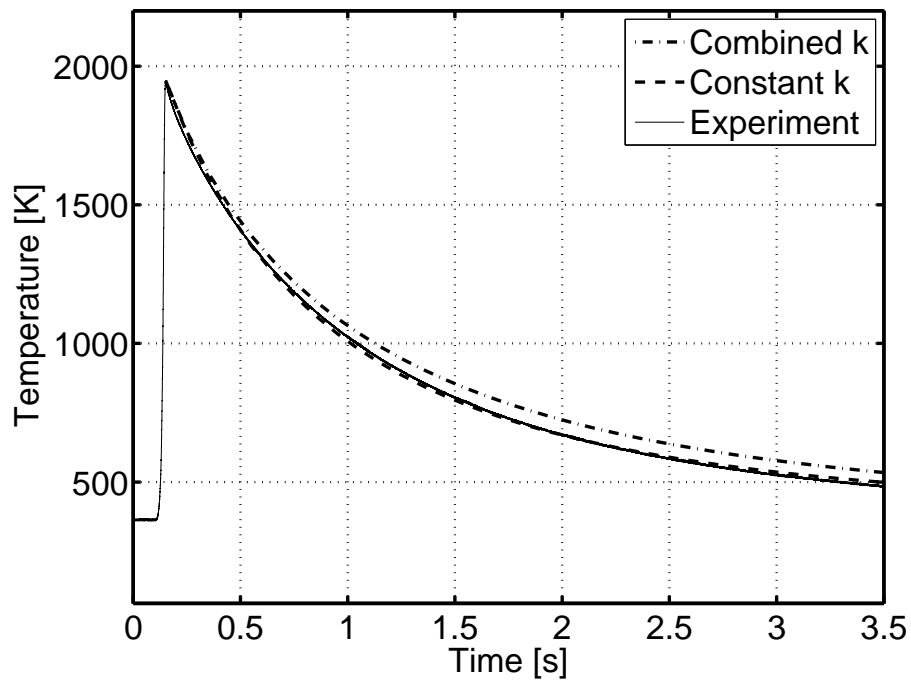


Figure 2.10: Cooling down determined by the driving turbulence of the mixing fan. $Nu = 13.5$ (case 4).

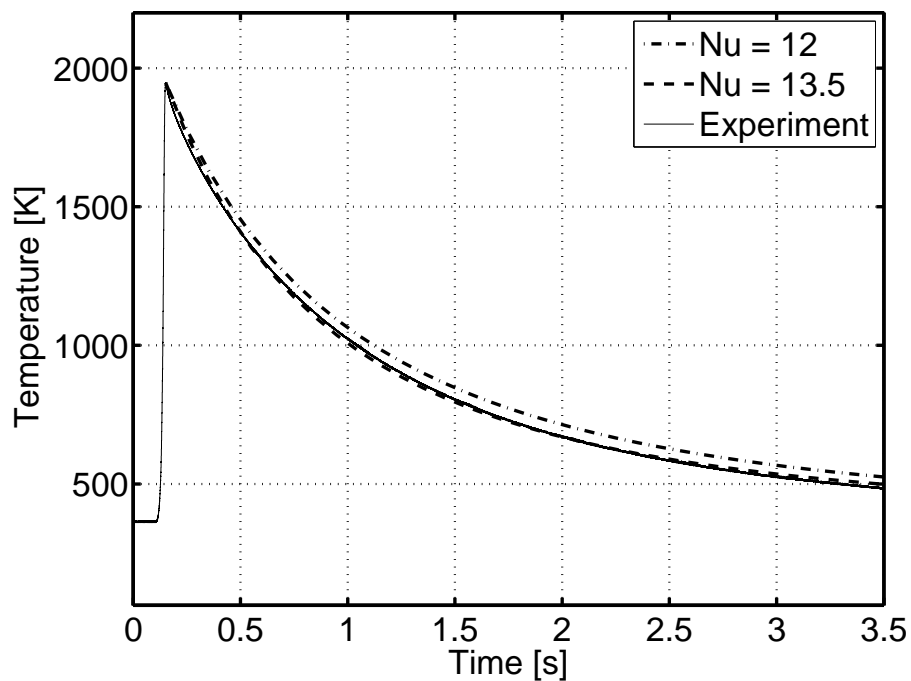


Figure 2.11: Cooling down determined by the constant turbulent kinetic energy driven by the mixing fan (case 4).

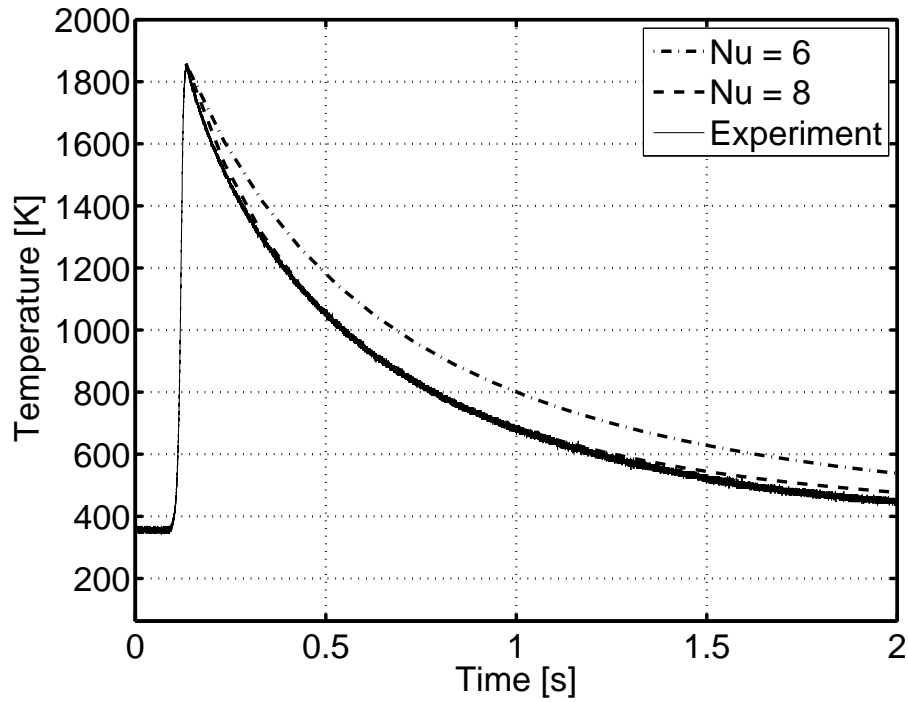


Figure 2.12: Cooling down determined by the constant turbulent kinetic energy driven by the mixing fan (case 5).

temperature T_b with the help of a mixing fan. Gimenes [3] and Meijer [11] studied the difference between core temperature and bulk temperature by analytical modeling and experiments, respectively. Gimenes' work on deriving the core-bulk temperature relation is used here.

Conservation of mass provides a relation between the volumes and temperatures, assuming that the pressure and molar mass are uniform in the cell. Dividing the volume of the cell in core volume (V_c) and boundary layer volume (V_{bl}), we have:

$$\frac{V}{T_b} = \frac{V_c}{T_c} + \int_{bl} \frac{dV_{bl}}{T_{bl}} = \frac{V}{T_c} + \int_{bl} \left(\frac{1}{T_{bl}} - \frac{1}{T_c} \right) dV_{bl} \quad (2.8)$$

where T_{bl} and V_{bl} are the temperature profile and volume of the boundary layer. To solve Eq. (2.8) and determine T_c , the relation between T_b , T_c and T_w is needed, which depends on the convection process involved. The walls of the HPC are at a constant temperature ($T_w = 380$ K).

Boundary layer theory describes the temperature in a turbulent boundary layer, $T_{bl}(x)$, as a function of time and boundary layer thickness δ [12]:

$$\frac{T_{bl} - T_w}{T_c - T_w} = \begin{cases} \left(\frac{x}{\delta} \right)^{\frac{1}{7}} & (x \leq \delta) \\ 1 & (x > \delta) \end{cases} \quad (2.9)$$

Then the integral in Eq. (2.8) can be rewritten as:

$$\int_{bl} \left(\frac{1}{T_{bl}} - \frac{1}{T_c} \right) dV_{bl} = \frac{cA\delta}{T_c} \int_0^1 \frac{1 - y^{\frac{1}{7}}}{1 + cy^{\frac{1}{7}}} dy \quad (2.10)$$

where $c = \frac{T_c}{T_w} - 1$ and $y = \frac{x}{\delta}$.

Inserting Eq. (2.10) into Eq. (2.8), we get the ratio of T_c and T_b :

$$\frac{T_c}{T_b} = 1 + \frac{A\delta}{V}\Psi(c), \quad (2.11)$$

in which $\Psi(c)$ is obtained from the integral of Eq. (2.10),

$$\Psi(c) = \frac{c+1}{60c^7} \left[-60 \frac{c^7}{c+1} + 70c^6 - 84c^5 + 105c^4 - 140c^3 + 210c^2 - 420c + 420 \ln(c+1) \right] \quad (2.12)$$

The last component to be solved in Eq. (2.11) is the boundary layer thickness δ . Heat transfer inside the HPC is dominated by turbulent flow. According to Incropera et al. [13], the boundary thickness based on characteristic length L is

$$\delta = 0.37L/Re_L^{\frac{1}{5}} \quad (2.13)$$

where the Reynolds number Re_L is obtained from the average Nusselt number Nu and the Prandtl number Pr . Subscript L refers to the value on the characteristic length. For the natural and forced convection in an enclosed cell, Nu is:

$$Nu = \begin{cases} 0.060Ra_L^{1/3} = 0.060Re_L^{2/3}Pr^{1/3} & (\text{natural convection [8]}) \\ 0.30Re_L^{1/2}Pr^{1/3} & (\text{forced convection [13]}) \end{cases} \quad (2.14)$$

where Pr is 0.7 for diatomic gases. Ra_L is Rayleigh's number. For known Nu , Re_L is obtained from Eq. (2.14). So the boundary layer thickness is:

$$\delta = \begin{cases} \frac{0.16LPr^{1/10}}{Nu^{3/10}} & (\text{natural convection}) \\ \frac{0.23LPr^{2/15}}{Nu^{2/5}} & (\text{forced convection}) \end{cases} \quad (2.15)$$

δ is time dependent because Nu is time dependent.

For the scenario without fan-mixing, the calculation is based on the condition of case 2 using the natural convection model. The development of boundary thickness is shown in Fig. 2.13. The difference between T_c and T_b is shown in Fig. 2.14 and Fig. 2.15. The boundary layer grows with time and the temperature difference decreases during the cooling process, and in general, the temperature difference is about 5 - 7%. The boundary layer thickness gradually increases while k decreases.

For the scenario with fan-mixing, the calculation is based on the condition of case 4 using the forced convection model. The boundary layer thickness is constant here as a consequence of a constant Nu . The difference between T_c and T_b is shown in Fig. 2.16 and Fig. 2.17. The boundary layer thickness stays constant and the temperature difference decreases during the cooling process, and in general, the temperature difference is about 2 - 6%, which is similar to Naber's measurement results (4 - 8%) [10].

It should be noticed that the boundary layer thickness highly depends on the turbulent kinetic energy. So the temperature ratio can be different at different compositions. The value of k is believed to be strongly related to the flame velocity of the pre-combustion. However, this is not in the scope of this work. k can be obtained by measuring the velocity field to check the assumptions related to the $Nu \sim k$ relation. To apply this model in a different setup with different geometry, the $Nu \sim k$ relation can be different.

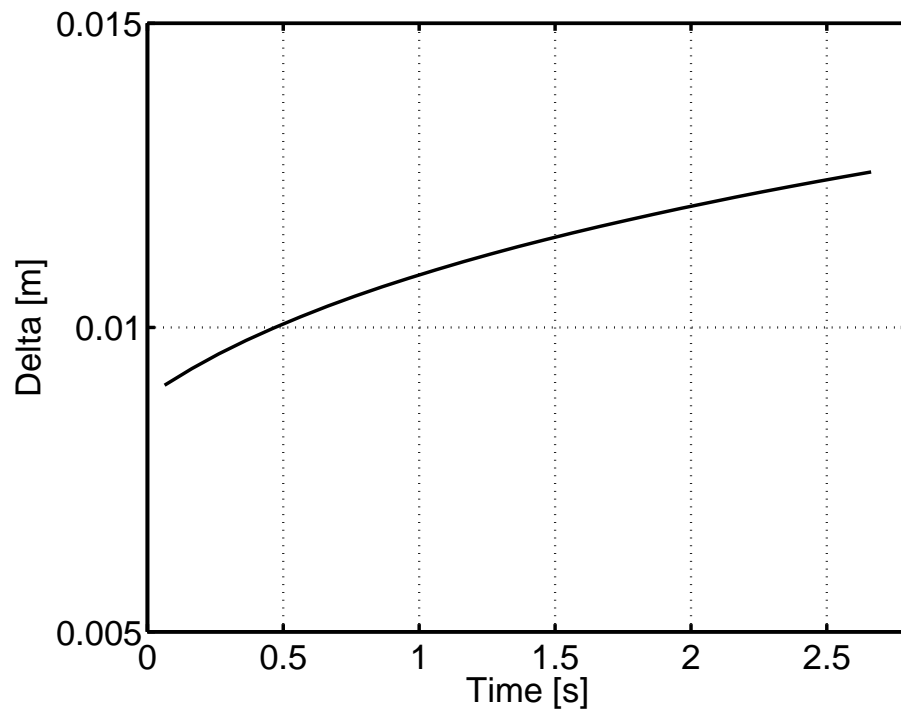


Figure 2.13: Development of boundary layer thickness without fan-mixing (case 2).

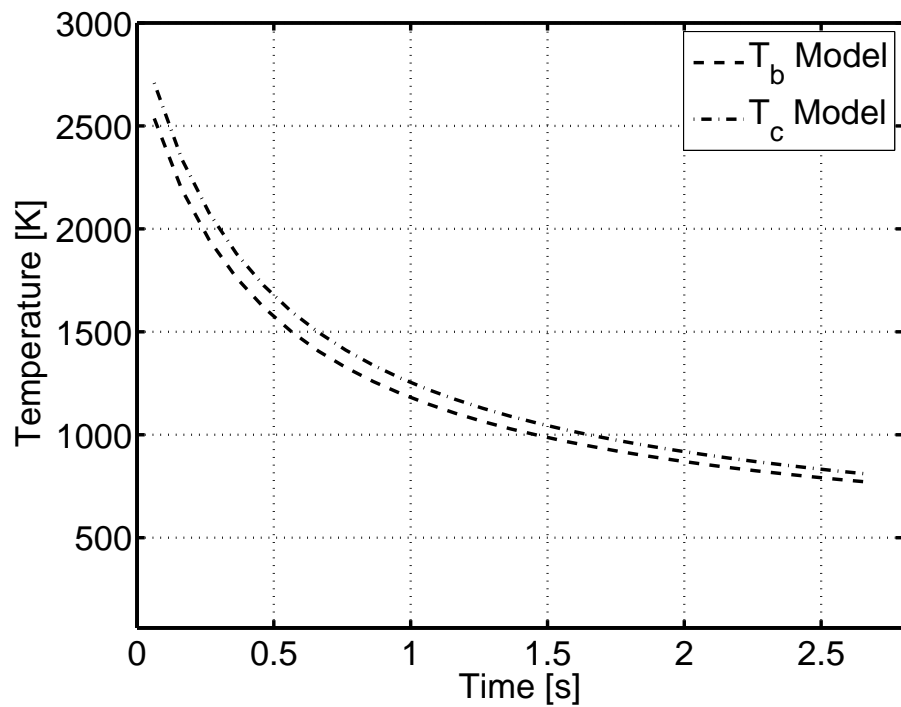


Figure 2.14: Comparison of the core temperature and the bulk averaged temperature without fan-mixing (case 2).

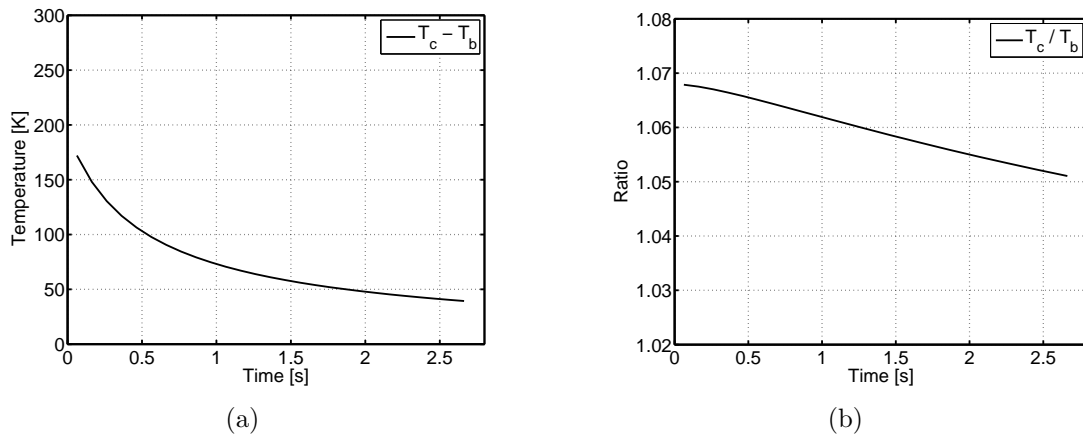


Figure 2.15: Difference between T_c and T_b using natural convection models (case 2).

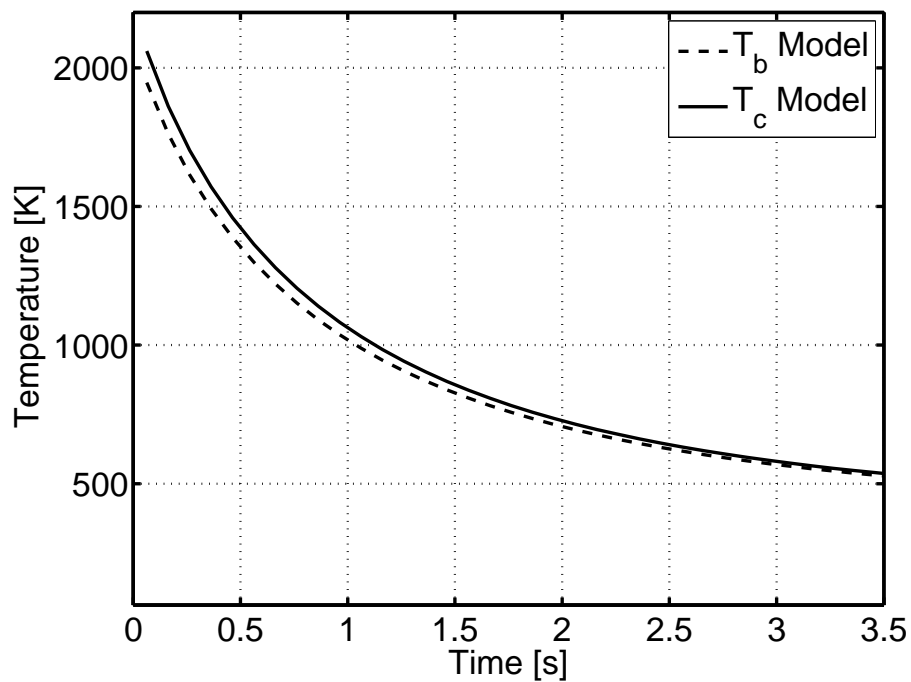


Figure 2.16: Comparison of the core temperature and the bulk averaged temperature with fan-mixing (case 4).

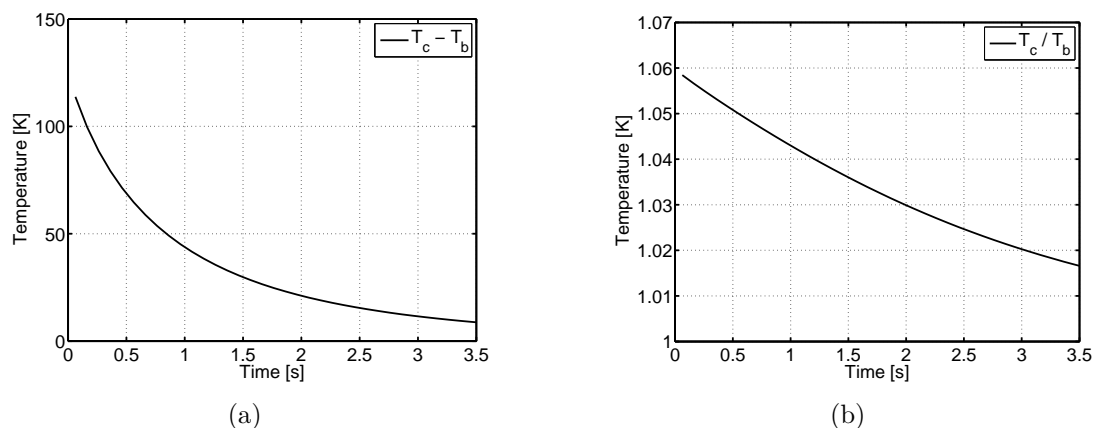


Figure 2.17: Difference between T_c and T_b using forced convection models (case 4).

2.4 Conclusions

The cooling process of the residual gas obtained after combustion of a premixed gas mixture in a closed volume cell has been studied, combining experiments with an analytical model. It can be observed that turbulent convection is dominating the cooling process. Without fan-mixing the heat transfer rate decays together with the turbulent kinetic energy. By assuming the decay rate of turbulent kinetic energy is proportional to the 1.5th power of turbulent kinetic energy itself, the cooling model can describe the cooling process with an accuracy of 50 K.

If fan mixing is on, a constant turbulent flow is delivered. So the turbulent kinetic energy is constant during the cooling process. With this assumption, the modeling results match experimental results very well for cases with fan on.

A natural and a forced convection model are used to estimate the thermal boundary layer and the core temperature in the scenarios without and with fan-mixing, respectively. In the first scenario, the core temperature is about 5 - 7% higher than the bulk temperature. In the second scenario the difference is 2 - 6%. The results is reasonable when compared with experiments.

Bibliography

- [1] D.C. Oren, S. Wahiduzzaman, and C.R. Ferguson. A diesel combustion bomb: Proof of concept. *SAE paper*, 841358, 1984.
- [2] L.M. Pickett, C.L. Genzale, G. Bruneaux, L.M. Malbec, L. Hermant, C. Christiansen, and J. Schramm. Comparison of diesel spray combustion in different high-temperature, high-pressure facilities. *SAE Int. J. Engines*, 2010-01-2106: 156–181, 2010.
- [3] T. Gimenes. Characterization of diesel sprays in the eindhoven high pressure cell. *Internal report, Department of Mech. Eng., Eindhoven University of Technology*, 2006.
- [4] R.S.G. Baert, P.J.M. Frijters, L.M.T. Somers, C.C.M. Luijten, and W.A. de Boer.

- Design and operation of a high pressure, high temperature cell for HD diesel spray diagnostics: Guidelines and results. *SAE Paper 2009-01-0649*, 2009.
- [5] Brigham Young University. Dippr database. <http://dippr.byu.edu/>.
- [6] T.H. Chung, L.L. Lee, and K.E. Starling. Applications of kinetic gas theories and multiparameter correlation for prediction of dilute gas viscosity and thermal conductivity. *Industrial & Engineering Chemistry Fundamentals*, 23(1):8–13, 1984.
- [7] T.H. Chung, M. Ajlan, L.L. Lee, and K.E. Starling. Generalized multiparameter correlation for nonpolar and polar fluid transport properties. *Industrial & Engineering Chemistry Research*, 27(4):671–679, 1988.
- [8] N.C. Markatos and K.A. Pericleous. Laminar and turbulent natural convection in an enclosed cavity. *Int. J. Heat Mass Transfer*, 27(5):755 – 772, 1983.
- [9] U. Frisch. *Turbulence: The legacy of A.N. Kolmogorov*. Cambridge University Press, 1995.
- [10] J.D. Naber, D.L. Siebers, S.S. Di Julio, and C.K. Westbrook. Effects of natural gas composition on ignition delay under diesel conditions. *Combustion and Flame*, 99(2):192 – 200, 1994.
- [11] M. Meijer, R.J. Christians, J.G.H. van Griensven, L.M.T. Somers, and L.P.H. de Goey. Engine combustion network: implementation and analysis of combustion vessel spray a conditions. *ILASS-Americas 23rd Annual Conference on Liquid Atomization and Spray Systems*, 2011.
- [12] P.J. Pritchard. *INTRODUCTION TO FLUID MECHANICS (8th ed.)*. JOHN WILEY & SONS, INC., 2011.
- [13] F.P. Incropera, D.P. De Witt, T.L. Bergman, and A.S. Lavine. *Fundamentals of Heat and Mass Transfer*. Sixth Edition. John Wiley & Sons, Inc., 2007.

Modeling of the temperature distribution in a fuel spray

In this chapter, the physical process of a fuel spray, being injected into stagnant ambient gas, is studied and two phenomenological models are summarized. The differences between the models are discussed. Both models predict spray penetration very well, however, they differ considerably in their prediction of the temperature distribution. The Valencia model predicts lower central line temperatures than the Versaevel model because of the assumption of a Gaussian enthalpy distribution. Experimental results do not show a Gaussian profile as well, which might be because the turbulence in a fuel spray is so strong that the multiple-injection-averaged Gaussian profile is not observable. Detailed evaluation of these two assumptions is needed in future.

3.1 Motivation

Modeling can help to understand the physical process and to analyse the influence of injection parameters on the spray characteristics. For spray modeling, Computational Fluid Dynamics (CFD) has the capability of simulating complex phenomena, including turbulence, combustion and complex geometry. However, CFD still has limitations concerning the atomization process and computational efficiency [1, 2]. On the other hand, a good phenomenological model always simplifies complex phenomena by capturing the major physical processes and ignoring the minor ones. For example, in spray models, the droplet size distribution is often ignored, because in modern diesel sprays, the droplets, resulting from breakup, are so small that the evaporation happens almost instantly depending mainly on the air entrainment rate [3]. These simplifications have been validated by spray liquid length and penetration measurement [3, 4], but the temperature distribution has not been validated yet. After comparing with experimental results, it is possible to evaluate the physical assumptions of the model and determine where it is applicable.

3.2 Physical processes in a fuel spray

In an internal combustion engine, a fuel spray is formed by discharging high-pressure liquid fuel through a small nozzle into relatively stagnant ambient gas: the velocity of a spray is much larger than that of the gas. The liquid jet breaks up into small droplets while it penetrates into the hot gas. Evaporation and mixing are the dominating processes after break-up. Here we will only discuss a phenomenological model that intends to capture the main physical processes with the necessary simplifications involved.

3.2.1 Nozzle discharge

The characteristics of the nozzle are important parameters to define the initial and boundary conditions for all spray models [5, 6].

The flow through an injector nozzle hole is basically governed by Bernoulli's law. The theoretical exit velocity U_{th} and the pressure difference Δp over the nozzle hole are coupled according to

$$U_{th} = \sqrt{\frac{2\Delta p}{\rho_f}}, \quad (3.1)$$

where ρ_f is the (liquid) fuel density. The resulting (theoretical) mass flow rate of the nozzle hole with diameter d_0 equals $\dot{m}_{th} = \rho_f U_{th} A_0$, where $A_0 = \pi d_0^2/4$ is the geometrical cross-sectional area of the circular nozzle hole with diameter d_0 . Bernoulli's law is only valid for incompressible, frictionless flow, which is not fully true during nozzle discharge. However, the difference can be "repaired" by relatively simple corrections. What actually happens in a nozzle hole is depicted in Fig. 3.1, taken from Payri *et al.* [7]. Fuel from the pressure reservoir rounds the inner corner, and strongly accelerates because of pressure difference. Due to the resulting high velocities, the

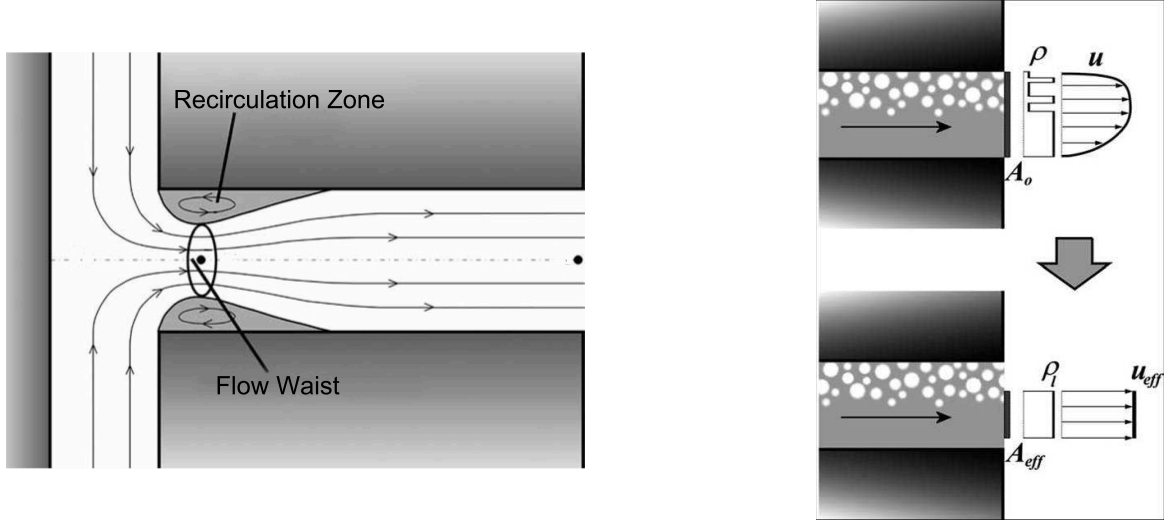


Figure 3.1: Left: schematic overview of internal nozzle flow with flow separation. Right: definition of effective velocity and surface area. (adapted from [7])

dynamic pressure strongly increases, possibly causing local static pressure to drop below the fuel's saturation pressure. Consequently, the flow may be cavitating. The bubbles formed are partly transported downstream with the fuel, changing the average density of the flow, as depicted on the right hand side of Fig 3.1. This can be interpreted as if the flow experiences an effectively smaller outflow area for fuel of (liquid-only) density ρ_l . The ratio of this effective area A_{eff} and the geometric area is $C_a = A_{eff}/A_0$, known as the *area contraction coefficient*. Below, we use $_{eff}$ to denote the actual value that is obtained from experiments, which is used in equations rather than the theoretical value.

The assumption of frictionless flow is also not fully correct: the exit velocity is smaller than the value obtained from Eq. (3.1). The difference is expressed in terms of the *velocity contraction coefficient*, $C_v = U_{eff}/U_{th}$. Combining both effects, the real mass flow from the nozzle hole can be written as $\dot{m} = \rho_f U_{eff} A_{eff}$. We can then define the ratio between the actual and theoretical mass flow; this is the *discharge coefficient* C_d , defined by

$$C_d = \frac{\dot{m}}{\dot{m}_{th}} = \frac{U_{eff}}{U_{th}} \cdot \frac{A_{eff}}{A_0} = C_v \cdot C_a. \quad (3.2)$$

Following similar arguments, we can also compare the real momentum flux with the theoretical one. The latter obviously is $\dot{M}_{th} = \rho_f U_{th}^2 A_0$; similarly, the effective momentum flux is $\dot{M} = \rho_f U_{eff}^2 A_{eff}$. Comparing the two in a ratio provides the *momentum coefficient* C_M , given by

$$C_M = \frac{\dot{M}}{\dot{M}_{th}} = \left(\frac{U_{eff}}{U_{th}} \right)^2 \cdot \frac{A_{eff}}{A_0} = C_v^2 \cdot C_a = C_d \cdot C_v. \quad (3.3)$$

\dot{m} and \dot{M} can be measured to determine C_M , C_m and C_d .

3.2.2 Spray penetration

The fuel, emanating from a nozzle hole in a modern diesel injector, exits with a velocity of several hundred meters per second and generally contains cavitation bubbles. Both lead to a vigorous breakup process of the liquid core. The process is subdivided into primary and secondary breakup. During primary breakup, the remaining part of the intact liquid core is torn apart into ligaments and (relatively large) droplets. Secondary breakup is the process by which these droplets are broken up into smaller ones. In a review paper by Smallwood and Gülder [8], ample evidence is provided that breakup in contemporary diesel sprays has fully taken place after only a few nozzle diameters and is no longer a limitation for the subsequent physical processes. Such a spray is often called “mixing-controlled” [9, 10], since the vaporization rate is controlled by the slowest physical process, the rate of mixing.

Vaporization happens together with breakup. The liquid phase initially travels together with the vapor phase [11], but after some distance no liquid is observed anymore. This distance remains quasi-steady (apart from turbulent fluctuations) when the injection pressure is steady, and is commonly denoted as “liquid length” L [3, 12, 13], see Fig. 3.2.

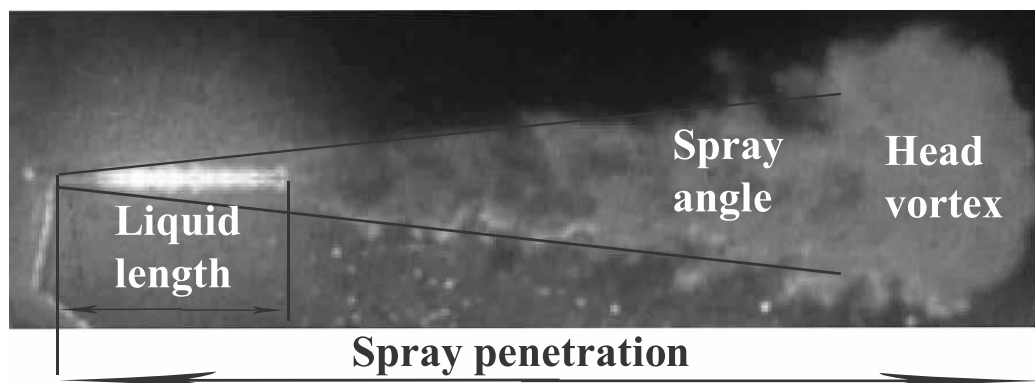


Figure 3.2: Picture of fuel spray (HPC data) showing penetration length S , cone angle θ and liquid length L .

Spray penetration can be characterized as follows. After leaving the nozzle, the spray quickly breaks up and the resulting mixture of (very small, continuously evaporating) droplets and entrained air penetrates into the combustion chamber. The head of the spray continuously meets stagnant air, and as a result develops a “head vortex”. A typical example is shown in Fig. 3.2, together with the definitions of spray penetration length S and spray (cone) angle θ .

Behind the head vortex, spray edges are relatively straight, with the exception of intermittently developing smaller side vortices. This region is commonly denoted as “quasi-steady”: although it grows in length (following behind the head vortex), processes in that region are invariant with time, apart from turbulent variations, when the injection pressure is stable.

The mixing process of a spray determines the rate of evaporation in the spray and the resulting equivalence ratio field throughout the spray. Therefore, it is of key importance to the efficiency and emissions of the combustion process. A quasi-steady cone angle means that there is a quasi-constant rate of air entrainment. As a result,

the overall mass contained in the spray in each cross-section is proportional to its position x . Due to conservation of momentum (total mass times velocity = constant), we have $x dx/dt = \text{const.}$, leading to $x \propto t^{1/2}$. Injection starts at $t = 0$. In other words, further away from the nozzle, spray penetration should scale with the square root of time due to momentum conservation. For different ambient conditions, the spray cone angle in all cases depends on the density ratio between ambient gas and liquid fuel [14–16]. The spray cone angle θ plays an essential role in the models to be discussed in section 3.3.

3.2.3 Spray radial profile

The radial profile of a spray during penetration has been experimentally investigated by several researchers [17–19]. Results have shown that, from downstream of the liquid length to upstream of the head vortex region, the individual profiles have significant run-to-run variations. But by averaging the individual profiles, a Gaussian cross sectional profile can be shown for both fuel concentration and velocity of a spray, see Fig. 3.3 and Fig. 3.4. For example, the velocity field is described as

$$U(x, r) = U_{cl}(x) \exp \left[-\alpha \left(\frac{r}{R} \right)^2 \right]. \quad (3.4)$$

At the edge of a spray, $r = R$, the shape factor $\alpha = \ln(U_{cl}/U(R))$. So α indicates the ratio of velocity on axis and edge. The radial width R of the velocity profile depends on spray cone angle θ , the relation being

$$R = x \tan(\theta/2). \quad (3.5)$$

The spray cone angle is obtained from experiments or empirical models.

A physical justification for the Gaussian profile lies in the Central Limit Theorem. This states that a combination (convolution) of many arbitrary statistical distributions will always give an overall Gaussian profile. Also experimentally, Gaussian profiles are always observed for fuel concentration and velocity.

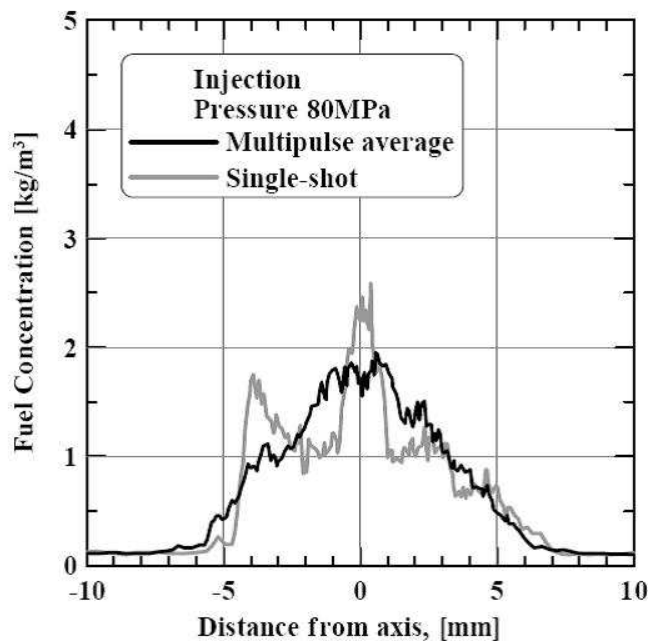


Figure 3.3: Comparison of single-shot and average radial profiles of fuel concentration [17].

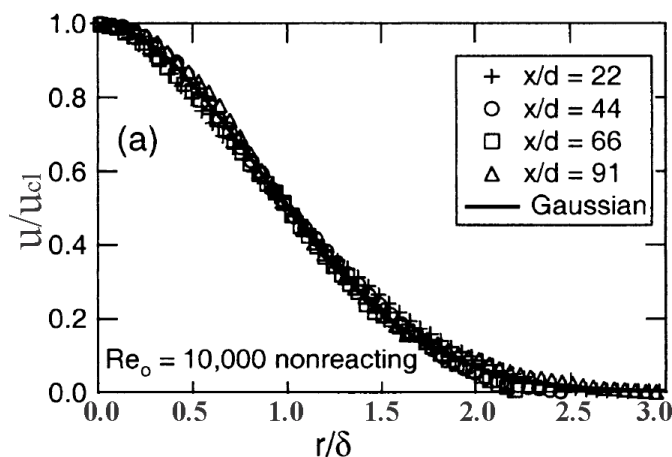


Figure 3.4: Radial profiles of the mean axial velocity normalized by the mean centerline velocity [18].

3.3 Phenomenological models of a fuel spray

Phenomenological models do not claim to be rigorous, but try to capture the most relevant physics in a way that is simplified to various degrees. Typically, they result in zero- to one-dimensional problems, which can be solved (semi-)analytically.

Phenomenological models are thus appealing, since they combine physical insight with computational simplicity. They also allow some (cautious) extrapolation, which enables parameter studies over wider parameter ranges. Last but not least, some researchers combine the strengths of phenomenological spray models and CFD to obtain more accurate results [4, 20].

In this section, two types of phenomenological spray models, the Versaevel and Valencia models are summarized and compared.

3.3.1 Summary of the Versaevel and Valencia spray models

The 1D quasi-steady spray model of Versaevel et al. [4] is an extension of work at Sandia National Laboratories (California, USA). The model started with the work of Naber and Siebers on non-vaporizing spray penetration [21], and was later extended to include liquid length, based on mixing-limited vaporization [9], and equivalence ratio at lift-off [22]. However, in these early Sandia models, thermodynamic equilibrium is not assumed from the nozzle exit to the liquid length. Versaevel et al. extended the thermodynamics to the whole system.

The basic assumptions of Versaevel model are:

- No velocity slip between gas and liquid phases;
- Whole system at constant pressure;
- Top-hat velocity, density and temperature radial profiles;
- Constant spray angle;
- Whole system at thermodynamic equilibrium.

The first four are the same as those made by Naber [21] and Siebers [9].

The Valencia model (Universidad Politécnica de Valencia) has been published, and gradually improved, in a series of publications over the last 7 years. The model started with the work of Desantes [6], using the concept of a non-vaporizing isodensity spray. In 2007, the isodensity concept was abandoned and evaporation was included [23, 24]. The coupling of evaporation and spray penetration as well as a transient 1D model was developed by Pastor and Desantes [10, 25].

Central to the quasi-stationary Valencia model is a number of assumptions:

- The fuel spray enters a stagnant environment, with constant and uniform ambient conditions (ρ_a, T_a) .
- Fuel mass flow rate \dot{m}_f , momentum flux \dot{M}_0 and spray velocity U_0 at the nozzle exit are constants and can be separately measured.
- The spray cone angle θ is constant and is obtained from measurements.
- Profiles of velocity, fuel mass fraction and enthalpy difference between axis and ambient gas over each cross-section of the spray are Gaussian; moreover they are self-similar, meaning that they are the same for every position in terms of appropriately scaled variables.
- Spray evolution is controlled by fuel-air mixing rates.

An important step in the development of both the Sandia/Versaevel model and the Valencia model is the coupling of thermodynamics (energy conservation) and spray

dynamics (mass and momentum conservation). Decoupling of these two physical processes leads to an underprediction of liquid length, due to the fact that realistic local densities in the spray are higher than predicted by such models (due to evaporative cooling). The too low model density results in too high velocities, stretching all relevant parameters (including liquid length) in axial direction [26].

The major difference between the two models lies in their assumption of radial profiles. The Versaevel model assumes top-hat radial profiles (Fig. 3.5) for fuel concentration and velocity, while the Valencia model assumes Gaussian profiles (Fig. 3.6). As a compensation for its simplification, the Versaevel model has to include two fit parameters, one for the cone angle (determining spray penetration) and an additional one for the liquid length prediction. As a benefit of Gaussian radial profile assumption, the Valencia model only needs to get the cone angle from experiments.

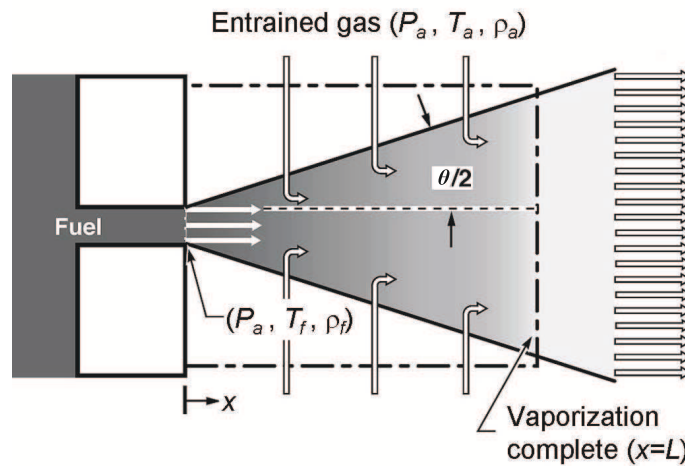


Figure 3.5: Schematic picture of the Sandia model with top-hat radial profiles [5]. The same profile is assumed in the Versaevel model [4].

Both the Versaevel and Valencia models had been compared against experimental results on liquid length and spray penetration. However, these comparisons can not reveal the difference on spray profile assumption: top-hat or Gaussian. Both assumptions are either based on single shot or averaged experimental measurements. One comparison was made by Kim et al. [19], who showed that the measured mean centerline equivalence ratio is higher than the value predicted by Sandia/Versaevel model [21]. The difference was attributed to the assumed steady injection rate in the model and the actual time-varying rate of the experiments. This is reasonable, because the averaged experimental results show a Gaussian profile, which should show higher equivalence ratio on the central line than the Versaevel model which assumes a top-hat profile.

3.3.2 Temperature distribution of a fuel spray

For both Versaeval and Valencia models, the temperature prediction is based on the enthalpy conservation at all cross sections. The local temperature of the spray is determined by the fuel mass fraction, liquid and vapor phase, in the mixture. So the

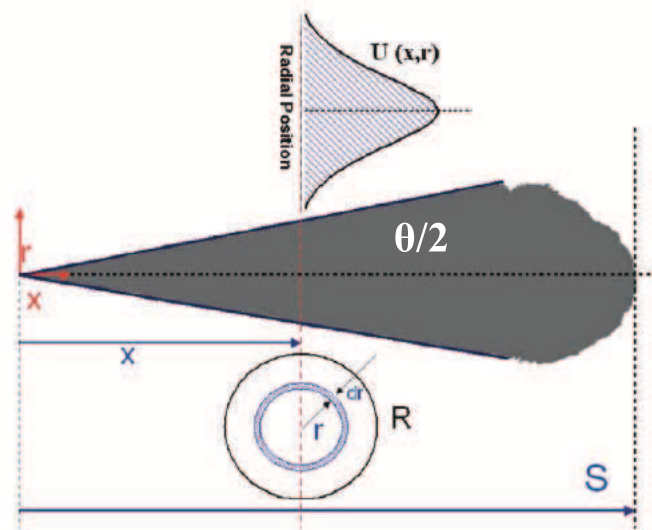


Figure 3.6: Schematic picture of the Valencia spray model with Gaussian radial profiles [6].

difference in fuel concentration profile leads to a different temperature profile. In this section the temperature distribution in fuel sprays are calculated from both Versaavel and Valencia models.

The Versaavel model was implemented by Bekdemir [27]. The Valencia model is implemented here based on the steady spray formation [25]. The scheme and script of the model can be found in Appendix A. N-heptane is used as a surrogate fuel for diesel. Despite the fact that n-heptane is more volatile than diesel, it is widely used as a surrogate fuel in modeling. The model is checked by reproducing the same results in the same condition as the original paper [25]. A modification to the model is that in the original paper, the spray angle is obtained from experiments while here it is calculated from Siebers' empirical relation [21]:

$$\tan(\theta/2) = ac \left[\left(\frac{\rho_a}{\rho_f} \right)^{0.19} - 0.0043 \left(\frac{\rho_f}{\rho_a} \right)^{0.5} \right], \quad (3.6)$$

which was obtained by fitting experimental results ($ac = 0.29$). Somewhat arbitrarily, the edge of the spray is defined here as the radius where the velocity has dropped to $\alpha = 1\%$ of the centerline value. With θ and α , the radial profile is determined.

The same relation is also used in the Versaavel model. However, $ac = 0.1$ has to be used to predict liquid length, otherwise it will be underpredicted. This arises a difficulty in predicting temperature distribution: the spray is calculated twice with the two 'ac' values. The spray is divided into two regions: within the liquid length, the temperature is calculated with the smaller $ac = 0.1$ value; in the vapor-phase region, $ac = 0.29$. The conservation laws exist on each cross section. However, at the point of liquid length, the continuity of spray angle is interrupted. This is a weakness of the Versaavel model.

The conditions of calculation are listed in Table 3.1. T_a and ρ_a are the temperature and density of ambient gas, respectively. P_{inj} is the injection pressure and d is the

diameter of the nozzle. The mass fractions of ambient gas are similar to those of experiments in Chapter 6, Fig 6.19.

Table 3.1: Calculation conditions (Compositions are given in mass fractions.)

T_a [K]	ρ_a [kg/m ³]	P_{inj} [bar]	d [mm]	N ₂	CO ₂	H ₂ O
590	20	900	0.15	0.83	0.14	0.03

Firstly, the spray penetration is compared, as shown in Fig. 3.7. Both models perform very similar in predicting the spray penetration. However, when looking at the temperature distribution along the central line of the spray, significant difference can be found in Fig. 3.8. The Versaevel model predicts higher temperature than that is predicted by the Valencia model.

For the Valencia model, the radial temperature distribution of the spray is shown in Fig. 3.9. The relatively high fuel concentration on the central line leads to relatively low temperatures. In the two locations downstream of the nozzle, the central axis temperature is 100 - 200 K lower than that in the outer wings of the spray.

Both models ignore conductive and radiative heat transfer processes. This simplification might be replaced by the top-hat assumption of Versaevel's model, which implies infinite mixing rate in the radial direction. The effect of this simplification should be examined. However, this is beyond the scope of this work.

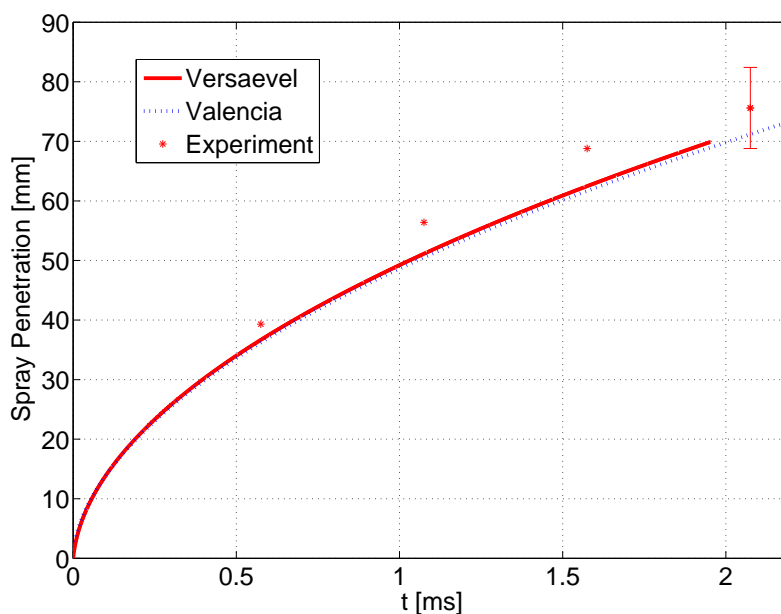


Figure 3.7: Comparison of spray penetration from models and experiments of Chapter 6.

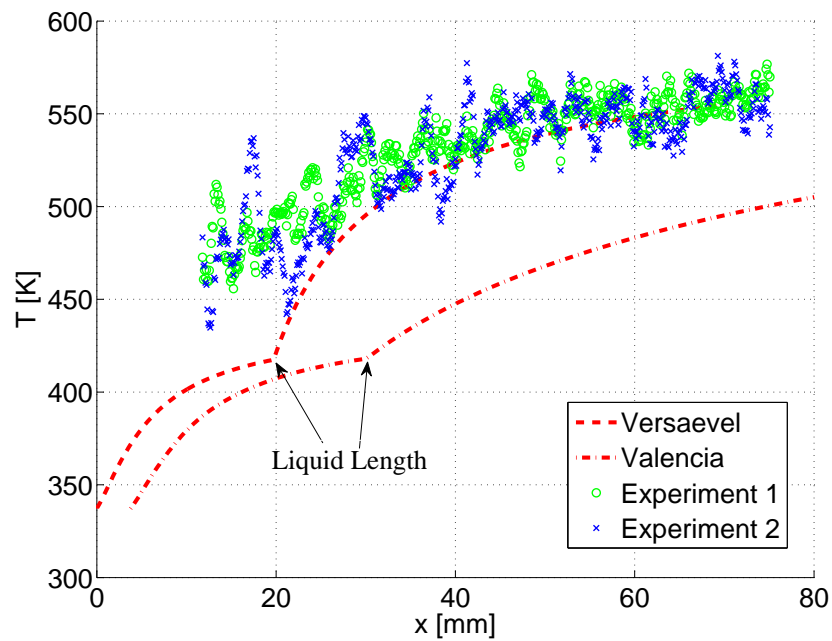


Figure 3.8: Comparison of temperature distribution along the central line of a fuel spray.

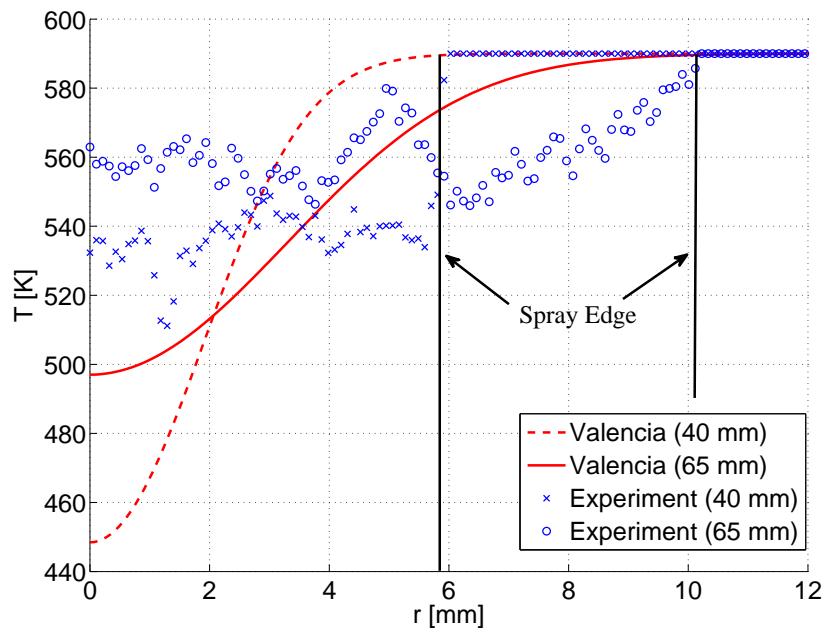


Figure 3.9: Radial temperature distributions at two cross sections of a steady n-heptane spray injected into hot gas, Valencia model versus experiments using LIF, see Table 3.1 for conditions.

3.4 Comparison with experiments

The model predictions are compared here with experimental results from Chapter 6 using laser-induced fluorescence (LIF), in which the details of the experiments can

be found. It should be noticed that the precision of the results is 4%, however the absolute accuracy is only validated at the edges of the sprays. The strong turbulence in the sprays also results in strong temperature variances.

Firstly, the spray penetration is compared with experiments, as shown in Fig. 3.7. The experimental spray penetration is taken from two separate runs. The predicted values are within the experimental accuracy. However, when looking at the temperature distribution along the central line of the spray, significant difference can be found in Fig. 3.8. The two experimental results are obtained from LIF measurements at 2.2 ms after injection.

The measured radial temperature distributions at two locations are shown in Fig. 3.9. The predicted spray edge is quite close to the experimental results, as indicated in the figure. The experimental data seems to demonstrate a top-hat distribution as assumed by the Versaevel model.

Nevertheless, it is still not conclusive to say that the Versaevel model predicts temperature better than the Valencia model. However, it is clear that the strong turbulence structure in single shot measurement dominates the temperature distribution, so that the multiple-averaged Gaussian assumption does not work better than the top-hat assumption to describe a single shot measurement.

3.5 Conclusions

Two phenomenological spray models were described and compared. The major difference exists in their assumptions for radial profiles of fuel-concentration and velocity. The Versaevel model assumes a top-hat profile while the Valencia model assumes a Gaussian profile.

The steady version of the Valencia model is implemented and compared with the Versaevel model, together with experimental results. Both models predict spray penetration very well, however, they differ considerably in their prediction of temperature distribution. The Valencia model seems to underpredict the central line temperature which might be because the turbulent structure in a fuel is so strong that the multiple-averaged Gaussian profile is not observable.

Bibliography

- [1] G. Stiesch. *Modeling engine spray and combustion process*. Heat and Mass Transfer. Springer, Berlin Heidelberg, 2003.
- [2] C. Baumgarten. *Mixture formation in internal combustion engines*. Heat and Mass Transfer. Springer, Berlin Heidelberg, 2006.
- [3] D.L. Siebers. Liquid-phase fuel penetration in diesel sprays. *SAE Tech. Paper 980809*, 1998.
- [4] P. Versaevel, P. Motte, and K. Wieser. A new 3D model for vaporizing diesel sprays based on mixing-limited vaporization. *SAE Tech. Paper 2000-01-0949*, 2000.

-
- [5] J. D. Naber and D. L. Siebers. Effects of gas density and vaporization on penetration and dispersion of diesel sprays. *SAE Paper 960034*, pages 59–88, 1996.
- [6] J.M. Desantes, R. Payri, F.J. Salvador, and A. Gil. Development and validation of a theoretical model for diesel spray penetration. *Fuel*, 85:910–917, 2006.
- [7] R. Payri, J.M. García, F.J. Salvador, and J. Gimeno. Using spray momentum flux measurements to understand the influence of diesel nozzle geometry on spray characteristics. *Fuel*, 84:551–561, 2005.
- [8] G.J. Smallwood and Ö.L. Gülder. Views on the structure of transient diesel sprays. *Atomization and Sprays*, 10:355–386, 2000.
- [9] D.L. Siebers. Scaling liquid-phase fuel penetration in diesel sprays based on mixing-limited vaporization. *SAE Tech. Paper 1999-01-0528*, 1999.
- [10] J.M. Desantes, J.V. Pastor, J.M. García-Oliver, and J.M. Pastor. A 1D model for the description of mixing-controlled reacting diesel sprays. *Combust. Flame*, 156:234–249, 2009.
- [11] L.M. Pickett, S. Kook, and T.C. Williams. Visualization of diesel spray penetration, cool-flame, ignition, high-temperature combustion, and soot formation using high-speed imaging. *SAE Tech. Paper 2009-01-0658*, 2009.
- [12] D. Verhoeven, J.L. Vanhemelryck, and T. Baritaud. Macroscopic and ignition characteristics of high-pressure sprays of single-component fuels. *SAE Tech. Paper 981069*, 1998.
- [13] J.V. Pastor, J.M. García, J.M. Pastor, and L.D. Zapata. Evaporating diesel spray visualization using a double-pass shadowgraphy/schlieren imaging. *SAE Tech. Paper 2007-24-0026*, 2007.
- [14] H. Hiroyasu and M. Arai. Structures of fuel sprays in diesel engines. *SAE Tech. Paper 900475*, 1990.
- [15] R.D. Reitz and F.V. Bracco. On the dependence of spray angle and other spray parameters on nozzle design and operating conditions. *SAE Tech. Paper 790494*, 1979.
- [16] S. di Stasio and L. Allocca. Influence of the gas ambient nature on diesel spray properties at high injection pressure: experimental results. In J. Whitelaw, F. Payri, and J.-M. Desantes, editors, *THIESEL 2000. Thermo- and Fluid-dynamic processes in Diesel engines*, pages 95–108, Valencia, 2000. Springer.
- [17] G. Bruneaux. Liquid and vapor spray structure in high-pressure common rail diesel injection. *Atomization and Sprays*, 11:105, 2001.
- [18] L. Muniz and M.G. Mungal. Effects of heat release and buoyancy on flow structure and entrainment in turbulent nonpremixed flames. *Combustion and Flame*, 126(1-2):1402 – 1420, 2001.

-
- [19] T. Kim and J.B. Ghandhi. Characterization of evaporating diesel sprays using exciplex laser-induced fluorescence measurements. *Atomization and Sprays*, 13: 535–559, 2003.
- [20] C. Bekdemir, E. Rijk, B. Somers, L.P.H. de Goey, and B. Albrecht. On the application of the 'flamelet generated manifold (FGM)' approach to the simulation of an igniting diesel spray. *SAE Tech. Paper 2010-01-0358*, 2010.
- [21] J.D. Naber and D.L. Siebers. Effects of gas density and vaporization on penetration and dispersion of diesel sprays. *SAE Tech. Paper 960034*, 1996.
- [22] D. Siebers and B. Higgins. Flame lift-off on direct-injection diesel sprays under quiescent conditions. *SAE Tech. Paper 2001-01-0530*, 2001.
- [23] J.M. Desantes, J.J. López, J.M. García, and J.M. Pastor. Evaporative diesel spray modeling. *Atomization and Sprays*, 17:193–231, 2007.
- [24] J.M. Desantes, R. Payri, J.M. García, and F.J. Salvador. A contribution to the understanding of isothermal diesel spray dynamics. *Fuel*, 86:1093–1101, 2007.
- [25] J.V. Pastor, J.J. López, J.M. García, and J.M. Pastor. A 1D model for the description of mixing-controlled inert diesel sprays. *Fuel*, 87:2871–2885, 2008.
- [26] C.C.M. Luijten and C. Kurvers. Real gas effects in mixing-limited diesel spray vaporization models. *Atomization and Sprays*, 20(7):595–609, 2010.
- [27] C. Bekdemir. Numerical modeling of diesel spray formation and combustion. Technical Report WVT 2008.15, Eindhoven University of Technology, 2008.

Laser diagnostic methods for temperature measurement

Various methods for temperature measurement have been applied. Compared with probing techniques, laser diagnostic methods have the advantage of being nonintrusive and instantaneous. Compared with other optical methods such as natural emission, laser diagnostics can give two dimensional or single-point measurements.

In this chapter, the process of selecting and optimizing laser diagnostic methods for two-dimensional temperature field measurement, of the pre-combustion residual gas and of non-reacting sprays, are described. The requirements of the diagnostics such as uncertainty, spatial and temporal resolution and operating range are specified and the candidate methods are tested and selected.

The subsection 4.5.1 is taken from:

M. Yu, G. Särner, C.C.M. Luijten, M. Richter, L.E.M. Aldén, R.S.G. Baert and L.P.H. de Goey, Survivability of thermographic phosphors (YAG:Dy) in a combustion environment, *Meas. Sci. Techn.*, 21(3), 037002.

Minor edits have been made to improve the quality.

4.1 Temperature diagnostic specifications

As stated in Chapter 1, temperature measurements are meant to provide more details for the new combustion concepts, such as Premixed Charge Compression Ignition (PCCI), which use relatively low ambient temperature to give more mixing time to the fuel before combustion. So the accuracy of the technique in the PCCI temperature range (<700 K) is highly important.

The temperature distribution in a fuel spray is influenced by both injection conditions, such as pressure, nozzle size, injection duration and ambient gas parameters such as temperature, density, specific heat, composition, etc. Some selected parameters of the ambient gas and the fuel spray in the High Pressure Cell (HPC) are listed in Table 4.1, the rest can be found in Chapter 2. The temporal resolution for spray experiments needs to be high enough because the spray velocity can be more than 100 m/s at the nozzle. So in 100 ns, the spray can propagate about 10 μ m or less. The image size is chosen to be about 50 mm * 25 mm to cover the vapor part of the spray.

Table 4.1: Specifications for spray temperature diagnostic

Imaging parameter	Value
Image size	≥ 50 mm \times 25 mm (spray measurement) ≥ 100 mm \times 100 mm (precombustion gas)
Spatial resolution	1 \sim 2 mm
Temporal resolution	100 ns (Spray measurement) 1 μ s (pre-combustion gas)
Precision	≤ 50 K
The HPC parameter	Value
Fuel	non-fluorescent diesel surrogate
Ambient density	~ 20 kg/m ³
$T_{ambient}$ at injection	500 \sim 700 K

4.2 Selection of laser diagnostics for HPC applications

Since the birth of the constant volume cell for spray combustion studies [1], much effort has been devoted to define the temperature field of the pre-combustion residual gas. The bulk averaged temperature (T_{bulk}) was calculated from the molecular weight of the pre-combustion products and the instantaneous test cell pressure [2]. Due to heat losses on the boundary, the gas temperature in the core (T_{core}) is higher than the gas temperature at the boundary. T_{core} was measured by thermocouples [3, 4]. An analytical model describing the cooling process was developed in this work (see Chapter 2). However, neither models nor the measurement of the two-dimensional temperature distribution have been reported in literature so far.

Two-dimensional temperature diagnostic methods include, but are not limited to, Rayleigh Scattering, Raman Scattering, laser-induced fluorescence (LIF) and laser-induced phosphorescence (LIP). There are two principles on the base of which to select the diagnostic method: firstly it should be able to meet the specifications stated in Table 4.1 and secondly the simpler experimental setup is preferred.

The four mentioned methods all potentially have the capability to meet the specifications. However, each method has its limitations: Rayleigh Scattering suffers from high background; Raman Scattering suffers from weak signal; many of the tracers of LIF cannot survive the pre-combustion; LIP faces the challenge to seed the solid phosphors into the ambient gas.

All these four methods were tested in the HPC. In the end, LIP turned out to be the optimal choice for measuring the ambient gas temperature. We use BaMgAl₁₀O₁₇:Eu (BAM) as the phosphor. The LIF method was chosen to measure the temperature distribution of the non-reacting n-heptane spray, using toluene as a tracer. The major characteristics of these methods, such as signal-noise ratio (SNR), are listed in Table 4.2. More details about selecting the phosphors and tracers are stated in sections to come.

Table 4.2: Main characteristics of the laser diagnostics applied to temperature measurement in the HPC.

Name	Rayleigh Scattering	Raman Scattering	LIP	LIF
Laser	532 nm	532 nm	355 nm	248 nm
Excited species	all species	major species	phosphor	tracers
Signal type	elastic	(anti-)stokes branch	red shift	red shift
Signal Intensity	strong	weak	strong	strong
SNR	low	low	high	high
Signal Lifetime	same as laser	same as laser	~ 1 μ s	~ 100 ns

4.3 Rayleigh Scattering

Rayleigh scattering is elastic: the scattered light has (almost) the same wavelength as the incident light. This fact brings convenience into the theory of Rayleigh scattering, but also makes it non-species-specific. The Rayleigh scattering intensity (I_R) is given by

$$I_R = CI_l N \left(\frac{\partial \sigma}{\partial \Omega} \right)_{mix}, \quad (4.1)$$

where C is a calibration constant, I_l is the intensity of the incident laser light and N is the number density of the gas. $\left(\frac{\partial \sigma}{\partial \Omega} \right)_{mix}$ is the total differential Rayleigh cross section, which indicates the power scattered in a particular direction $\partial \Omega$. The scattering cross section σ is defined as $\sigma = P/I_l$, where P is the total power scattered from one scatter, e.g. a molecule. Assuming the ideal gas law, $p = NkT$, we can deduce the

relation between temperature and Rayleigh scattering intensity. Assuming pressure and composition are uniform in the cell, temperature is proportional to the reciprocal of local number density N , which gives:

$$T_f = \frac{T_{ref} N_{ref}}{N_f}, \quad (4.2)$$

where the index ref is for reference data and f is for measured data. Combining this formula with Eq.(4.1), we get:

$$T_f = \frac{T_{ref} I_{ref} \left(\frac{\partial \sigma}{\partial \Omega} \right)_f}{I_f \left(\frac{\partial \sigma}{\partial \Omega} \right)_{ref}}, \quad (4.3)$$

given that the laser intensity and the optical collection system are both the same in reference and in measurement.

Rayleigh Scattering is a simple technique which only requires a single laser with a fixed frequency and a single camera to measure the temperature field. Fourquette et al. [5] have used this technique to obtain temperature fields over the range of 300 to 2000 K in a turbulent flame. However, the major drawback is that scattered laser light from particles in the flow and from the boundaries can saturate the camera and obscure the image. Filtered Rayleigh Scattering (FRS) was then developed, which uses a very narrow notch filter to suppress the scattered light from particles and boundaries [6]. The designing of a reliable and repeatable filter greatly increased the complexity of the FRS setup.

Another important source of uncertainty is shot-to-shot fluctuations in the laser profile and energy. The scattering signal is proportional to the intensity of each pulse, which varies from pulse to pulse. The energy per pulse can be detected by a photo-detector, and compensated for in data processing. However, the laser intensity profile, energy distribution over the laser sheet, is unknown. The estimated uncertainty of laser intensity profile can cause around 12% SNR of the result [7]. An example is shown in Fig. 4.1, where scattered light from the back wall and dust strongly interfere with the measurement.

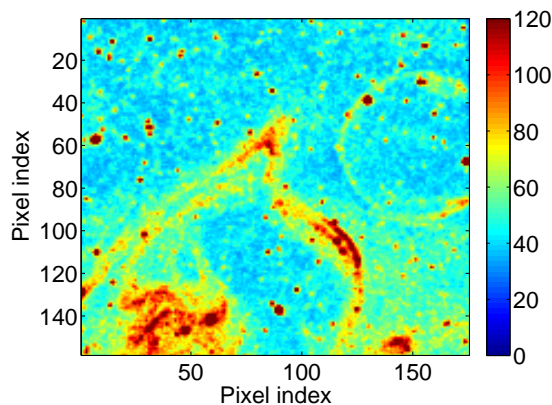


Figure 4.1: An example of the influence of boundary and particles in Rayleigh Scattering. The bright points are dust in the HPC and the valve on the back wall is clearly seen.

In summary, Rayleigh Scattering is a simple method to measure temperature. However, the low SNR caused by particle/boundary reflection and laser shot-to-shot fluctuations are serious drawbacks. Although it is possible to overcome these problems by increasing the complexity of the setup, this does not seem to be the best option.

4.4 Raman Scattering

Raman Scattering, contrary to Rayleigh Scattering, involves inelastic scattering of photons. The difference between Raman Scattering and Rayleigh Scattering is illustrated in Fig. 4.2. When a photon hits a molecule, three possibilities exist for the outcome. It can scatter without any energy exchange (Rayleigh Scattering), lose energy to the molecule (Stokes Scattering) or gain energy from the molecule (Anti-Stokes Scattering). The latter two phenomena are called Raman Scattering, named after Sir C.V. Raman.

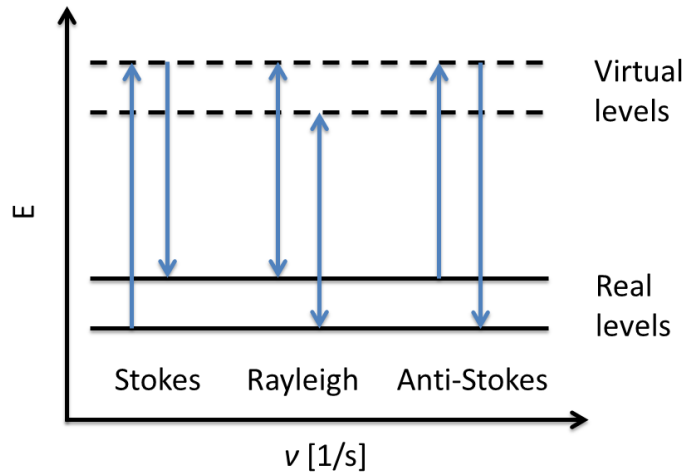


Figure 4.2: The different possibilities of light scattering: Rayleigh scattering (no Raman effect; the incident and emitted photons have the same energy), Stokes scattering (the molecule absorbs energy; the emitted photon has less energy than the absorbed photon) and anti-Stokes scattering (the molecule loses energy; the emitted photon has more energy than the absorbed photon)

The intensity of Raman scattering is

$$I_{Ra} = C I_l N \sigma \Omega l F(T) \quad (4.4)$$

where C is a constant, I_l the laser intensity, N the molecule number density, σ the Raman cross-section, Ω the scattering solid angle, l the length of the observed segment of the laser beam and $F(T)$ is a temperature dependent factor determined by the spectral width and resolution of the detection system and the investigated molecule. The intensity of the Stokes branch of Raman scattering (I_S) is much stronger than that of the anti-Stokes branch (I_{AS}) because the N is much larger in the ground state, since the population of molecular states is governed by the Boltzmann distribution. So it is quite straightforward to use I_S/I_{AS} to measure the temperature.

However, the drawback of Raman Scattering is that the signal is very weak. In the HPC, the density is about 20 times higher than at atmospheric pressure. So

we had expected sufficient Raman Scattering signal intensity. The laser we used is a Nd:YAG laser at 532 nm, 90 mJ/pulse. The major species, N₂, O₂ and CO₂ are tested. However, Raman Scattering still turns out to be too weak for even 1D measurement, where the intensity of the laser is concentrated in a thin 1D line instead of a 2D plane.

4.5 Laser-induced phosphorescence

Laser-induced phosphorescence (LIP) measurements are based on the fact that thermographic phosphors, after excitation by e.g. a laser, will emit red-shifted light carrying local temperature information. The micrometer sized particles exhibit high temperature sensitivity from cryogenic temperatures up to 2000 K [8], with the advantages of high accuracy, high signal yield, no collisional quenching, no Doppler broadening and so on. In combustion research, laser-induced phosphorescence has during recent years been demonstrated to have a great potential for surface thermometry in internal combustion engines, gas turbines and fire safety applications, and has recently been extended to combustion-related gaseous temperature measurements [9–12].

However, there are several open questions regarding applications of LIP in a combustion environment. For example, there are concerns about oxygen quenching on some types of phosphorescence [13], and about the low signal intensity at high temperature, combined with the strong black-body radiation of the phosphors and/or chemiluminescence of the flame. Phosphors without oxygen quenching issues are preferred and their measurement range are checked.

Various kinds of thermographic phosphors have been examined for their characteristics [8, 9], among which, Y₃Al₅O₁₂:Dy (YAG:Dy) and BaMgAl₁₀O₁₇:Eu (BAM) are potential candidates to meet the specifications of Table 4.1. There are two reasons. Firstly both phosphors are suitable for ratio methods, where the ratio of emissions in two wavelength bands is used as measure for temperature. It is easier to use a ratio method than a life-time method to do 2D measurements. Secondly, the temperature-sensitivity range of both phosphors covers 400 K to 1400 K on surface measurement. The challenge to apply LIP in gaseous measurement is that the phosphors have to be properly seeded into the gas. The number density should be high enough to ensure enough signal, but not too high to influence the combustion process. This limitation results in less signal intensity than is observed in surface measurement. Since the LIP signal decays dramatically when temperature increases, the intensity has to be checked to determine the measurable range. The seeding challenge will be addressed in Chapter 5.

Still one of the most important issues is the “survivability” of phosphors in combustion. For example, YAG:Dy is one of the most widely used phosphors, whose melting point is 2213±7 K [14]. This is of the same order or below the maximum temperature of many kinds of flames, and may therefore result in phase transitions and even chemical reactions. For LIP applications in combustion research, it is essential to validate if the thermal characteristics of phosphors will change when they experience a high-temperature combustion environment. Although there are other challenges, it is possible to apply LIP in certain applications once the survivability of phosphors is shown. One of the applications is the measurement of temperature distribution inside

a constant volume cell, which uses the pre-combustion method [2] to replicate the thermodynamic conditions prevailing in an internal combustion engine.

In this section, the survivability of YAG:Dy in combustion environments are tested. The survivability of BAM and more details of LIP will be introduced in Chapter 5. The major characteristics of both phosphors are listed in Table 4.3.

Table 4.3: Major characteristics of YAG:Dy and BAM

Name	Laser	measurement spectrum	Density	Particle Diameter
YAG:Dy	355 nm	455 & 497 nm	4.56 g/cm ³	1-3 μ m
BAM	355 nm	400 & 458 nm	3.7 g/cm ³	2-7 μ m

4.5.1 Survivability of YAG:Dy phosphors in a combustion environment

The feasibility of applying laser-induced phosphorescence in a combustion environment was shown by testing the consistence of the emission-temperature relations of thermographic phosphor particles (YAG:Dy). The relations were calibrated before and after the phosphor particles had passed a flame front. The calibrations were performed in air and in pure oxygen. The emission-temperature relation prevails from around 300 K to 1300 K. The difference in emission-temperature relation for the two different cases is less than the experimental precision (3%).

In the emission spectrum of YAG:Dy, two spectral regions differ in how they are affected by temperature. As shown in Fig. 4.3, with temperature ascending, the 455 nm emission peak increases in intensity whereas the 497 nm emission peak decreases in intensity. The intensity ratio of these two spectral positions exhibits the temperature sensitivity that can be utilized for thermometry. This ratio is recorded at different temperatures whereafter a curve that holds the emission-temperature relation can be fitted to the measured data. By comparing the fitted calibration curves before and after the YAG:Dy particles have experienced a combustion environment, the consistency of YAG:Dy emission temperature relations, as well as the consistency of the temperature relations between air and pure oxygen environments are demonstrated.

Experimental Method

To calibrate the YAG:Dy emission temperature relations, a 3-window tube furnace was used to control the temperature of the phosphor. The temperature to calibrate against was measured with thermocouples. The oven was not completely air tight, but sufficiently covered to suppress convection. The pressure inside the oven was 1 atm. Due to the fact that the leakage of the oven was very low, the environment in the oven could be altered between air and pure oxygen by flushing the oven accordingly. The phosphors were excited by the third harmonic of a Nd:YAG laser at 355 nm (Quantel YG980) and the emission was collected by two spherical lenses. A dichroic mirror was used to block any scattered light from the 355 nm laser. The light emission from the phosphors was dispersed by a spectrometer and recorded by an ICCD camera.

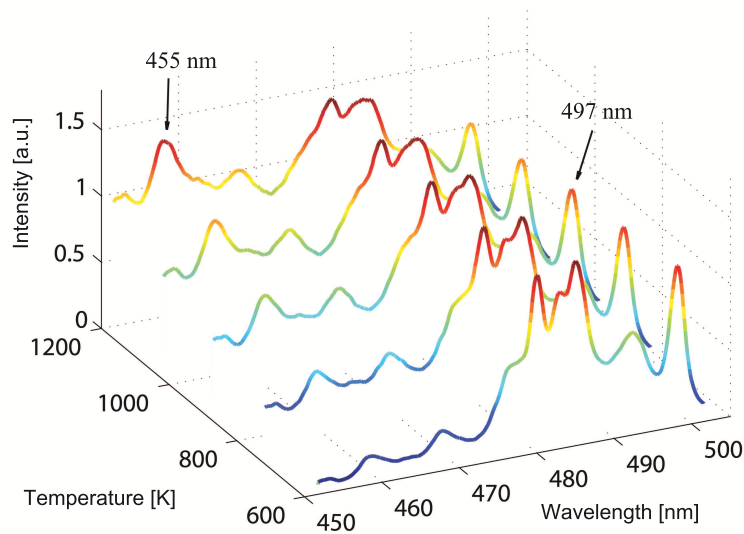


Figure 4.3: Effect of temperature on two spectral regions of YAG:Dy emission.

From 485 K to 1308 K, the laser-induced phosphorescence of YAG:Dy was recorded and analyzed to calculate the ratio of the emission peak at 455 nm and 497 nm. A curve describing the intensity ratio as a function of temperature was fitted from the experimental data. Above ~ 1300 K, the sensitivity of the intensity ratio was lost.

The combustion environment was created by a lean ($\phi = 0.9$) methane-air premixed flame on a burner. Phosphor particles were seeded into the air flow of the burner by a seeder (fluidized-bed concept). It could be shown that particles having a $1.8 \mu\text{m}$ diameter, a density of 4.56 g/cm^3 , a $590 \text{ J/(kg}\cdot\text{K)}$ heat capacity and a $14.0 \text{ W/(m}\cdot\text{K)}$ thermal conductivity, would yield a response time of $2 \mu\text{s}$ when heated up from room temperature to 99% of the flame temperature. In the flame, the phosphor particles were heated to about 2000 K. The gas phase temperature was calculated from adiabatic flame temperature. The temperature inside the particle is assumed to be uniform because its size is only about $1.8 \mu\text{m}$. For the same reason, the relative speed of particles and gas flow is negligible. When we consider a single particle, we can assume the Reynolds number to be zero and convection is not important in heat transfer. For the simplest calculation, we only consider conduction. The result has shown that the particles can respond fast enough to the gas phase temperature. If we include the effect of radiation, the response time will only be shorter.

Since the lean flame did not produce any soot particles the issue of phosphor particle contamination was avoided. After passing the flame, the phosphor particles were cooled down and captured by an impactor. The impactor was connected with a vacuum pump to collect the phosphor particles. The scheme of the experimental setup is shown in Fig. 4.4.

Results and Discussion

Calibration experiments as described above were carried out to study the influence of the combustion environment on the temperature characteristics of the phosphor par-

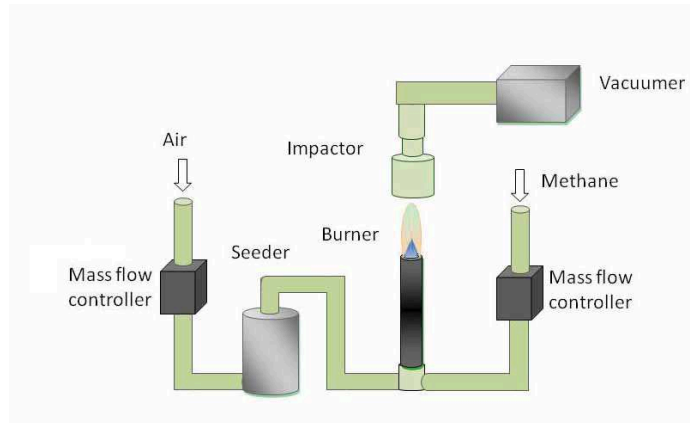


Figure 4.4: Setup for dispersing and recapturing phosphor particles in a combustion environment.

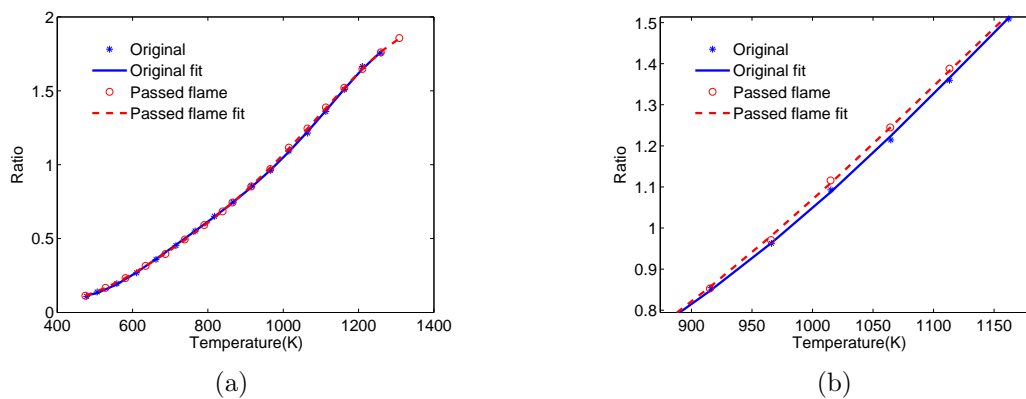


Figure 4.5: Comparison of emission-temperature relations of the YAG:Dy in air using the intensity ratio method, before and after passage through a lean methane-air flame: (a) Curves of the complete temperature range; (b) A zoom-in picture of the largest difference.

ticles. The method was to compare the emission-temperature relations of the original phosphor and the phosphor that had passed the flame front in an air environment, as presented in Fig. 4.5(a). At each experimental point, every 50 K, 20 spectra were accumulated to minimize the influence of laser energy fluctuation. Background emission including black-body radiation of the phosphors was also recorded and subtracted to get the corrected signal. The ratio of two spectral peaks could then be calculated. One curve, which can be represented by a fifth order polynomial very well, can be fitted into all the intensity ratios in each condition.

It is evident that these two curves in Fig. 4.5(a) are almost identical, which demonstrated the unchanged property of phosphors after encountering the flame. As shown in Fig. 4.5(b), the largest difference between them is 9 K which occurs around 1015 K. This difference is within the uncertainty of the experiments, which means that the emission-temperature relations are consistent. The result thus shows that combustion does not have an obvious influence on the emission-temperature relation.

Since combustion often involves consumption of oxygen, the concentration of oxygen might also influence the accuracy of the measurement, in case of oxygen quenching

of the phosphorescence. To assess the effect of oxygen quenching, the experiment was repeated in a pure oxygen environment, which was obtained by flushing the oven with oxygen. The phosphor powder was the same as in former experiments. Both phosphors were calibrated before and after passage through a lean methane-air flame. At each 250 K from 305 –1082 K, the spectra were recorded and compared. For the phosphors that passed the flame, the difference in the emission intensity ratio expressed in terms of temperature (according to the “emission-temperature-relation”, Fig. 4.5(a)) was smaller than 20 K; while for the original phosphors, the difference is smaller than 30 K. The differences are again within the uncertainty range. Therefore oxygen quenching is considered not to have a significant influence on the temperature dependent emission spectra of YAG:Dy.

The experimental precision depends on the calibration procedure as well as the signal intensity. In the high temperature range, the signal intensity is weakened while the black-body radiation of the phosphor particles increases. The signal to noise ratio decreases consequently. The black-body radiation was subtracted to correct the signal. However, when the intensity of the black-body radiation is of the same magnitude as the signal, the subtraction will bring an extra error to the signal. Thus the calibration does not include temperatures above 1308 K. The error of thermocouple measurements is 1% in the experimental temperature range. The precision of the optical system was estimated by doing and comparing several emission measurements at the same temperature. The error was minimized by accumulating 20 images at each measurement. The precision of the optical system is 2%. The overall precision is estimated to be better than 3%.

Summary and Future work

In summary, we reported the consistence of YAG:Dy emission-temperature relations in a combustion environment. The relations were calibrated for the phosphor before and after passage of a flame front in air and in a pure oxygen environment. The applied emission-temperature relation range varied from 300 K to 1300 K and the estimated precision is better than 3%. By comparing experimental results at different conditions, we can conclude that the emission-temperature relation of YAG:Dy is neither affected significantly by a combustion environment nor by the oxygen concentration. The obtained results show the applicability of laser-induced phosphorescence for temperature measurements in applications where the phosphor particles are exposed to flame chemistry and flame temperatures, and then drop to below 1300 K, e.g. to experimentally characterize temperature gradients in a diesel simulation cell. In a broader view, considering the most difficult application of laser-induced phosphorescence, i.e. turbulent flames, another challenge still remains. Questions like signal interferences from black-body radiation of phosphor emission and chemiluminescence need to be solved. Due to the turbulence, the signal cannot be corrected by subtracting the black-body radiation and chemiluminescence. Detector gating would not provide an effective suppression either, because most thermographic phosphors used so far have a long lifetime (for YAG:Dy about 100 ns at 1308 K) and weak signal at high temperatures. This should be compared to other techniques, e.g. laser-induced fluorescence and Raman scattering where gating down to the laser pulse duration (~ 10 ns) would not influence the signal intensity but largely suppress all continuous

background emission. There is evidently a great need for thermographic phosphors with very short emission lifetime. It has recently been found that some phosphors do have phosphorescence lifetimes in the subnanosecond range [15]. However, those phosphors have no sensitivity above 900 K, reducing the high temperature usability. For future development of the laser-induced phosphorescence method, the challenge is to search for a thermographic phosphor type that has both a short life-time and a strong signal at high temperature.

4.6 Laser-induced fluorescence

Laser-induced fluorescence (LIF) is a widely used method for concentration and temperature measurement [16–18]. LIF uses one or more kinds of species as a tracer (naturally existing or seeded to the mixture) that carries the temperature information. The tracer molecules (e.g. toluene) are laser-excited into higher electronic states and then emit fluorescence. The fluorescence is collected by one or more cameras. The intensity and the spectrum of the LIF signal depend on pressure, temperature and the local concentration of the tracer. Depending on the tracer, the laser light source and the methods to collect signal can be different. A review article by Schulz and Sick [19] presents the status of tracer-LIF, including different experimental strategies. In this section, we discuss how to determine the tracer and setup for temperature measurement of the spray in the High Pressure Cell (HPC) using the tracer-LIF method. The method and its results are further elaborated on in Chapter 6.

4.6.1 Selecting the tracer

Commercial fuel contains many fluorescing components, which interfere with each other making quantitative interpretation of measurements impossible. In this work, n-heptane (C_7H_{16}) is used as a surrogate fuel. To ensure quantitative measurement, the purity of the fuel is important. HPLC-grade n-heptane was used in this work. A fluorescing tracer must be added to carry the temperature information.

To measure the fuel spray quantitatively, we consider three main criteria in selecting a tracer:

- The tracer should cause minimum change on the fuel property;
- The tracer-LIF signal preferably only depends on temperature and tracer concentration;
- Simplicity is preferred in implementing the tracer-LIF method.

To investigate non-reacting sprays, the physical properties of the fuel are important, such as density, viscosity, heat capacity, and boiling point. The properties of the tracer should be close to those of n-heptane. Since n-heptane is organic, choosing an organic tracer is a reasonable choice. Commonly used organic tracers include 3-pentanone, acetone or toluene. The comparison of the physical properties of these tracers are listed in Table 4.4, where the value of density, heat of vaporization and heat capacity are given at 298.15 K. As an example, the property of a mixture of 90%

Table 4.4: The physical properties of the tracers [20]

Name	M [kg/kmol]	ρ [kmol/m ³]	$T_{boiling}$ [K]	H_{evap} [J/kmol]	$c_{p,gas}$ [J/(kmol*K)]
3-Pentanone	86.1	9.4	375.14	$3.85 \cdot 10^5$	$1.23 \cdot 10^5$
Acetone	58.1	13.5	329.28	$3.1 \cdot 10^7$	$7.45 \cdot 10^4$
Toluene	92.1	9.36	383.78	$3.8 \cdot 10^7$	$1.04 \cdot 10^5$
N-heptane	100.2	6.78	371.58	$3.65 \cdot 10^7$	$1.65 \cdot 10^5$
Mixture*	99.39	7.04	–	$3.66 \cdot 10^7$	$1.59 \cdot 10^5$
$\frac{Mixture}{N-heptane}$	0.99	1.04	–	1.00	0.96

*: the mixture contains 90% n-heptane and 10% toluene.

n-heptane and 10% toluene is also listed in the table. The properties of the mixture are at maximum 4% different from the value of pure n-heptane.

During spray penetration, air entrainment and turbulence mix fuel and ambient air. Thus the concentration distribution of the tracer will not be homogeneous. As stated before, the LIF signal will carry the information of temperature, concentration and laser fluence all together, making it difficult to interpret. A ratio method (also called two-line method [21]) is based on using the ratio of two parts of the spectrum to obtain temperature information. The ratio carries temperature information, because the spectrum shifts with changing temperature as can be seen in Fig. 4.6. In calculating the ratio, the spatial distribution of tracer and laser profile of the images, which are irrelevant to spectral shift, cancel.

The intensity of LIF, I_F , is given by

$$I_F = CI_l(x, y)N(x, y)f(T, \lambda), \quad (4.5)$$

where C is a constant, $I_l(x, y)$ the local laser intensity, $N(x, y)$ the local tracer density and $f(T, \lambda)$ the temperature dependent factor. Thus the ratio of two spectral bands (red and blue) is:

$$R = \frac{I_{red}}{I_{blue}} = \frac{CI_l(x, y)N(x, y)f(T)_{red}}{CI_l(x, y)N(x, y)f(T)_{blue}} = \frac{f(T)_{red}}{f(T)_{blue}}. \quad (4.6)$$

To use the ratio method, 3-pentanone and acetone need two lasers to excite the tracer, while toluene only needs one laser. So toluene LIF is a better method in terms of simplicity. The absorption curve of toluene extends from 230 nm to 290 nm [22, 23]. A fourth harmonic Nd:YAG laser (266 nm) or a KrF-excimer laser (248 nm) is commonly used to excite toluene. The beam profile of an Excimer laser is more like a top-hat, while the Nd:YAG laser has a Gaussian-like profile. The top-hat profile gives a more even signal intensity, so the Excimer laser (Lambda Physik, Compex 350T) is used. Toluene is a common organic solvent, so Viton rings were used in the sealing of the HPC to prevent erosion.

4.6.2 Spectral bands for ratio method

After excitation, toluene emits the fluorescence. When temperature increases, the intensity decreases and the spectrum shifts to the red. A set of normalized spectra at

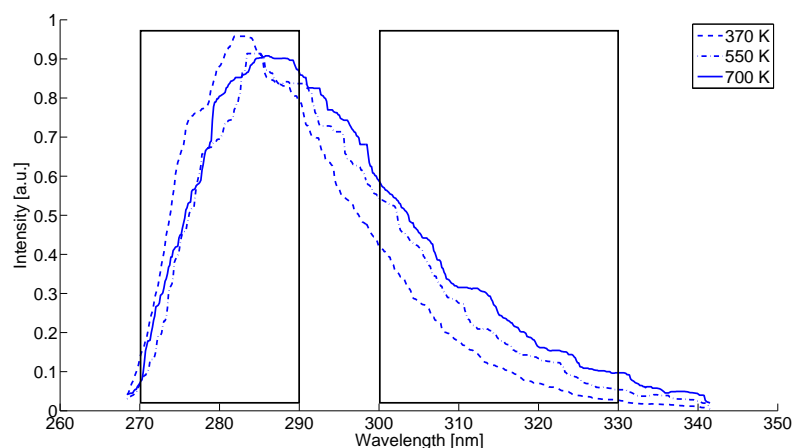


Figure 4.6: Normalized toluene LIF spectrum at three different temperatures. The two boxes indicate the wavelength regions of the two cameras.

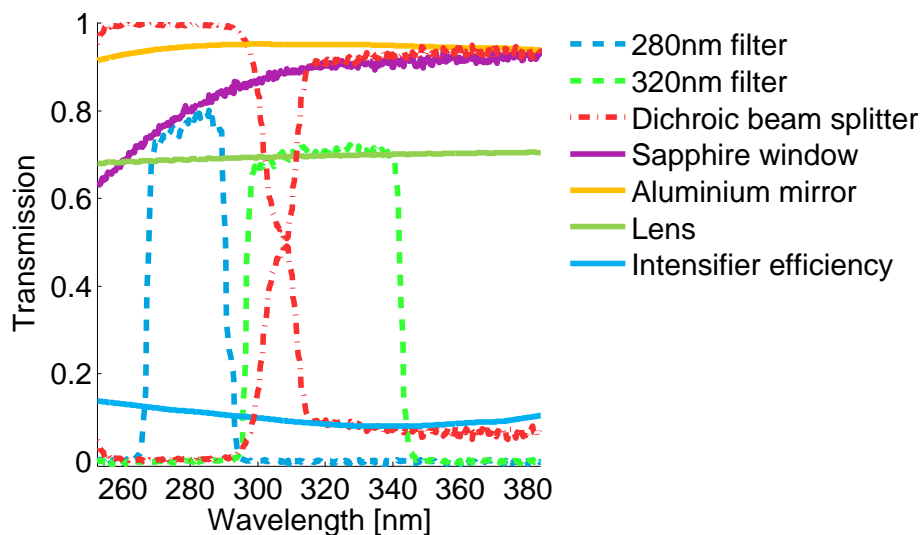


Figure 4.7: Transmission, reflection efficiencies and photocathode quantum efficiency of the optic detection line. The values of filters, dichroic beam splitter and sapphire window are measured. The other values are based on manufacturer specifications.

different temperatures are obtained from the HPC by a glow plug which is installed inside just for this purpose. Temperature measurement for the glow plug is not accurate enough for calibration. Fig. 4.6 shows an example of spectra shift with temperature.

In Fig. 4.6, the two blue rectangles indicate the approximate transmission bandwidth of the band pass filters that we used for the ratio method. The filter on the blue side centers at 280 nm with 20 nm band width, while the filter on the red side centers at 320 nm with 40 nm band width. The transmission rates of the filters are shown in Fig. 4.7.

4.7 Summary

In this chapter, the specifications were determined for 2D temperature measurement of sprays and residual gas in the HPC. Four laser diagnostic methods were tested and compared to select the most optimal ones. For measuring temperature of residual gas of pre-combustion, laser-induced phosphorescence using BAM as thermal phosphor was selected, mainly for its strong signal. For non-reacting sprays, laser-induced fluorescence using toluene as a tracer was selected for the simplicity of setup. For both diagnostic methods, the ratio method is used to cancel the influence of laser profile and differences in tracer concentration.

Bibliography

- [1] D.C. Oren, S. Wahiduzzaman, and C.R. Ferguson. A diesel combustion bomb: Proof of concept. *SAE Technical Paper Series*, 841358, 1984.
- [2] R.S.G. Baert, P.J.M. Frijters, L.M.T. Somers, C.C.M. Luijten, and W. de Boer. Design and operation of a high pressure, high temperature cell for HD diesel spray diagnostics: guidelines and results. *SAE Paper 2009-01-0649, 2009*, 2009.
- [3] R.P. Durrett, D.C. Oren, and C.R. Ferguson. A multidimensional data set for diesel combustion model validation: I - initial conditions, pressure history and spray shapes. *SAE Technical Paper Series*, (872087), 1987.
- [4] L.M. Pickett, C.L. Genzale, G. Bruneaux, L.M., L. Hermant, C. Christiansen, and J. Schramm. Comparison of diesel spray combustion in different high-temperature, high-pressure facilities. *SAE Int. J. Engines*, 3:156–181, 2010.
- [5] D.C. Fourquette, R.M. Zurni, and M.B. Long. Two-dimensional Rayleigh thermometry in a turbulent nonpremixed methane-hydrogen flame. *Combustion Science and Technology*, 44(5-6):307–317, 1986.
- [6] D. Hoffman, K.-U. Münch, and A. Leipertz. Two-dimensional temperature determination in sooting flames by filtered Rayleigh scattering. *Opt. Lett.*, 21(7): 525–527, Apr 1996.
- [7] D.F. Marran, J.H. Frank, M.B. Long, S.H. Stårner, and R.W. Bilger. Intracavity technique for improved Raman/ Rayleigh imaging in flames. *Opt. Lett.*, 20(7): 791–793, Apr 1995.
- [8] M.R. Cates, S.W. Allison, L. Jaiswal, and D.L. Beshears. YAG:Dy and YAG:Tm fluorescence to 1700 C. *ISA - 49th International Instrumentation Symposium*, 2003.
- [9] G. Särner. *Laser-Induced Emission Techniques for Concentration and Temperature Probing in Combustion*. PhD thesis, Lund University, 2008.
- [10] R. Hasegawa, I. Sakata, H. Yanagihara, B. Johansson, A. Omrane, and M. Aldén. Two-dimensional gas-phase temperature measurements using phosphor thermometry. *Applied Physics B: Lasers and Optics*, 88:291–296, 2007.

-
- [11] A. Omrane, G. Särner, and M. Aldén. 2D-temperature imaging of single droplets and sprays using thermographic phosphors. *Applied Physics B*, 79:4:431–434, 2004.
- [12] J. Brübach, A. Patt, and A. Dreizler. Spray thermometry using thermographic phosphors. *Applied Physics B*, 83:4:499–502, 2006.
- [13] J. Brübach, A. Dreizler, and J. Janicka. Gas compositional and pressure effects on thermographic phosphor thermometry. *Meas. Sci. Technol.*, 18:764–770, 2007.
- [14] J.L. Caslavsky and D.J. Viechnicki. Melting behaviour and metastability of yttrium aluminium garnet (YAG) and YAlO₃ determined by optical differential thermal analysis. *J. Mater. Sci.*, 15:1709–1718, 1980.
- [15] G. Särner, M. Richter, and Aldén M. Two-dimensional thermometry using temperature induced line shifts of ZnO:Zn and ZnO:Ga fluorescence. *Optics Letters*, 33:12:1327–1329, 2008.
- [16] M. Luong, R. Zhang, C. Schulz, and V. Sick. Toluene laser-induced fluorescence for in-cylinder temperature imaging in internal combustion engines. *Applied Physics B*, 91(3-4):669–675, 2008.
- [17] G. Tea, G. Bruneaux, J.T. Kashdan, and C. Schulz. Unburned gas temperature measurements in a surrogate diesel jet via two-color toluene-LIF imaging. *Proceedings of the Combustion Institute*, 33(1):783 – 790, 2011. ISSN 1540-7489.
- [18] M. Cundy, P. Trunk, A. Dreizler, and V. Sick. Gas-phase toluene LIF temperature imaging near surfaces at 10 kHz. *Exp Fluids*, 51:1169–1176, 2011.
- [19] Sick V. Schulz, C. and. Tracer-LIF diagnostics: quantitative measurement of fuel concentration, temperature and fuel/air ratio in practical combustion systems. *Progress in Energy and Combustion Science*, 31(1):75 – 121, 2005.
- [20] Brigham Young University. Dippr database. <http://dippr.byu.edu/>.
- [21] M. Aldén, A. Omrane, M. Richter, and G. Särner. Thermographic phosphors for thermometry: A survey of combustion applications. *Progress in Energy and Combustion Science*, 37(4):422 – 461, 2011. ISSN 0360-1285.
- [22] C.S. Burton and W.A. Noyes. Electronic energy relaxation in toluene vapour. *J Chem Phys*, 49:1705, 1968.
- [23] W. Koban, J.D. Koch, R.K. Hanson, and C. Schulz. Absorption and fluorescence of toluene vapor at elevated temperatures. *Phys. Chem. Chem. Phys.*, 6:2940 – 2945, 2004.

Temperature measurements of residual gas using BAM-LIP

We demonstrate the feasibility of laser-induced phosphorescence thermography for gas phase temperature field measurement in a high pressure cell (HPC). $\text{BaMgAl}_{10}\text{O}_{17}:\text{Eu}$ (BAM) was used as a thermographic phosphor; it shows a blue-shifted laser-induced emission spectrum with increasing temperature. Local temperature was determined from the intensity ratio of two disjunct emission bands. A new seeding device was developed to suspend the solid thermographic phosphor particles in a gas environment. The particle suspension time was modeled and validated by experiments. The influence of multiple scattering and other aspects of quantitative measurement were examined. The technique is currently capable of measuring up to 650 K, limited by signal intensity. The 2D temperature distributions were measured with a precision better than 60 K at 650 K. Multiple scattering limits the spatial resolution to about 10 mm along the line of sight.

This chapter is an integral copy of the article which has been submitted to Applied Physics B: Lasers and Optics. Minor changes have been made to improve the quality.

J.P.J. van Lipzig, M. Yu*, N.J. Dam, C.C.M. Luijten, L.P.H. de Goey, Gas phase thermometry in a high pressure cell using BaMgAl₁₀O₁₇:Eu as a thermographic phosphor, *submitted to Applied Physics B: Lasers and Optics (in revision)*, (2012).

*: The second author is the corresponding author and the direct supervisor of the first author.

5.1 Introduction

Ongoing development of advanced optical diagnostics to measure temperature distributions non-intrusively is of great importance to advanced combustion engine research. For example, the temperature distribution of the gas mixture prior to fuel injection is an important parameter in understanding the role of temperature stratification during premixed charge compression ignition (PCCI) combustion. In PCCI [1, 2], a positive time delay exists between end of injection and start of combustion, which results in lower emissions due to better mixing of fuel and air. In our group, an optically accessible constant-volume high pressure cell (HPC) [3] is used to investigate fuel sprays under engine-like conditions, including those representative for PCCI. The mass-averaged temperature of the gas inside the HPC can be computed accurately from the measured pressure using the ideal gas law. However, determining local temperatures non-intrusively is more of a challenge.

Laser-induced phosphorescence (LIP) is a promising technique to determine the 2D temperature fields in the gas phase. The method is based on electronically exciting a thermographic phosphor (TP) with laser radiation. During the relaxation, the TP emits radiation with a spectrum that changes with temperature, see Fig. 5.1 [4]. From the intensity ratio of two disjunct emission bands the temperature can be determined using a separately determined ratio-temperature calibration. The spectral bands used in our experiments are indicated by grey shading in Fig. 5.1. By using appropriate band pass filters in front of two separate cameras, and, after proper alignment, dividing the images on a pixel-by-pixel bases (so-called ‘image ratios’), the 2D temperature field is obtained. The LIP technique is an established method for remote surface temperature measurements [5–8]. The advantages of LIP include non-intrusiveness, high signal yield, insensitivity to oxygen quenching and independence of local TP concentration and laser intensity profile, which makes it a promising method for temperature measurements in the gas phase [4, 9, 10]. In this work the feasibility of gas phase TP thermometry is investigated.

To determine the local temperature, the TPs need to be seeded into a gas as solid particles. Seeding concentration and stickiness of particles have been concerns since the first attempt of Hasegawa [11]. In this work a new seeding device is designed, based on a powder injector from Wagner Group [12].

The TP needs to maintain its temperature dependent characteristics when exposed to the transient high temperature of the pre-combustion event, which is used to create engine-like conditions in the HPC. The survivability of a commonly used thermographic phosphor (YAG:Dy) in a harsh combustion environment was proven by Yu et al. [13]. First experiments with YAG:Dy for the present purpose gave insufficient signal levels. For this reason YAG:Dy was not further investigated in this work, and BaMgAl₁₀O₁₇:Eu (BAM) is used as TP, because of its higher signal yield.

BAM is the common name for a Barium Magnesium Aluminate crystal doped with Europium, which is a rare earth metal. BAM can be excited with 355 nm laser radiation, which results in a very strong emission in the blue spectral region, see Fig. 5.1. The emission originates from the transition of the 4f⁶5d configuration to the 4f⁷ configuration of Eu²⁺ and peaks around 440 nm [14]. BAM is available in powder form with a median particle diameter of 3.5 μm. The particle size distribution, presented in Fig. 5.2, is log-normal distribution fitted through specification data provided by

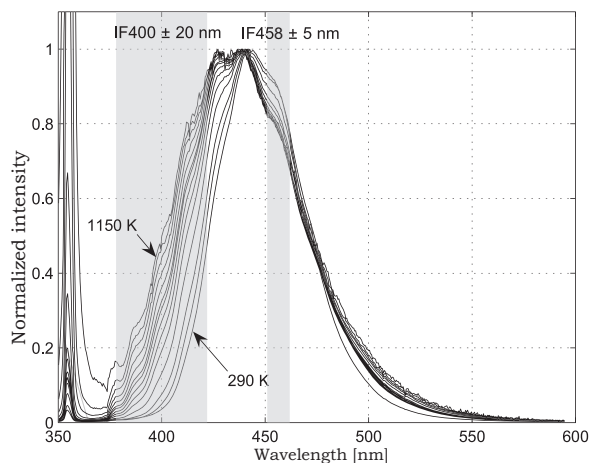


Figure 5.1: Emission spectrum of BAM for various temperatures (spectral regions which are used to determine the T-dependent intensity ratio are marked in grey) [4].

the manufacturer (Phosphor Technology).

Particle stickiness is a major concern, since optical access can be blocked by particles sticking on the windows of the combustion vessel. Lindén et al. [15] concluded from experience that BAM particles coated with SiO_2 stick the least. Therefore, the same coating is used in this work.

Recent studies show that it is not recommended to use BAM for temperature measurements higher than 800 K due to degradation mechanisms [16, 17]. Yet, the degradation process is rather slow; in the work of Bizarri and Moine [17], baking times of 150 min are used to prove the degradation effect. In this work the phosphorescent material is heated up to 2300 K and cooled down to 400 K over a timespan of seconds. Heating is achieved by means of spark-ignited combustion of the gas mixture, which in the case studied here also consumes all available oxygen. The degradation mechanisms are not investigated in this work. However, the influence of high temperature on the BAM particles is addressed.

The main objective of this work is to study the feasibility of using the LIP technique with TP particles to determine the 2D temperature field in the gas phase. The paper focusses on the measurement technique. First the experimental setup is discussed, in which the working principle of the newly designed seeder is explained, followed by a discussion about the behavior of the phosphorescent particles together with other aspects of quantitative measurements. The calibration procedure, obtained results and conclusions are presented in the last part.

5.2 Experimental

In Fig. 5.3 a schematic overview of the experimental setup is given. The TP particles are seeded into the HPC using the particle seeder described below. The cameras used are a PI-MAX 2 and a PI-MAX 3 ICCD from Princeton Instruments, placed on opposite sides of the HPC and fitted with interference filters (spectral pass bands indicated in Fig. 5.1).

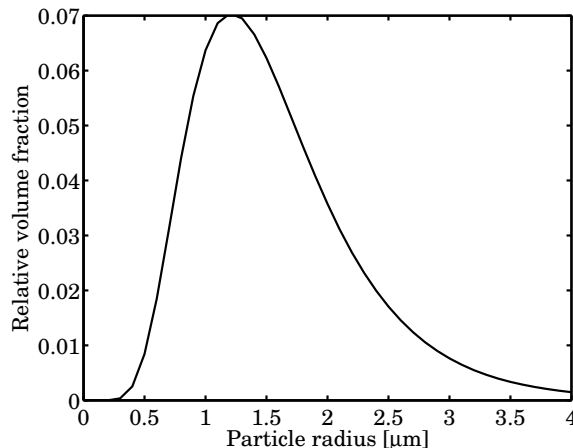


Figure 5.2: Particle distribution of BAM thermographic phosphors (Phosphor Technology).

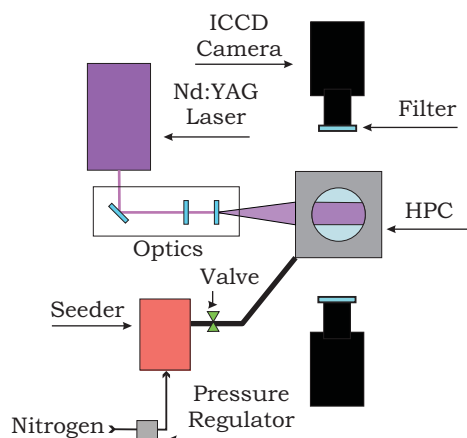


Figure 5.3: Top view of the experimental setup. HPC is depicted in front view in order to visualize the laser sheet.

5.2.1 High pressure cell (HPC)

The core of the HPC is a cubic combustion chamber produced through spark erosion inside a stainless steel cube. Ports on each side of the combustion chamber can be fitted either with a window or with a metal plug. The HPC is equipped with sub-systems for heating, cooling, fuel injection, gas supply, control, data acquisition and optical diagnostics. During experiments the walls of the HPC are kept at 393 K. The mixing fan is not used in this work, because the fan appeared to increase the number of particles sticking to the walls of the HPC. A more detailed description of the HPC is given by Baert et al. [3].

The gas supply system is based on four mass flow controllers, which enable filling pure gases one by one to prepare the gas mixture inside the HPC. The filling process is monitored by a gas pressure sensor. The HPC is evacuated before each experiment and subsequently filled with C_2H_2 and Ar. The filling procedure is paused after the filling of argon and the TP particles are seeded into the HPC using nitrogen as carrier gas. After the seeding the filling procedure is continued with N_2 and O_2 to form the desired mixture, which, once burned, produces the same density, O_2 mass

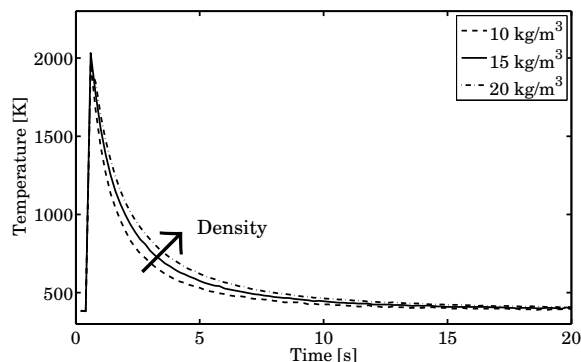


Figure 5.4: Temperature traces of typical experiments at various gas densities.

fraction and heat capacity as those expected at the desired engine condition. In Fig. 5.4 the cooling curves (mass-averaged temperature vs time) of typical experiments with a gas density of 10, 15 and 20 kg/m³ are presented. The global mass-averaged temperature (presented in Fig. 5.4) is derived from the pressure signal. The TP is used to determine the 2D temperature field after the pre-combustion inside the HPC, so as to characterize the ambient condition into which a fuel spray would be injected.

5.2.2 Seeding device

The BAM particles must be suspended in the gas in order to determine local temperatures. In the work of Omrane et al. [18], particles are dispersed in alcohol and transported using compressed air through a nebulizer in order to create a spray. The alcohol carrying the particles evaporates and only the TP particles remain. This strategy is not suitable in this work because alcohol or another liquid will influence the combustion event. In the work of Lindén et al. [15] and Yu et al. [13] a fluidized bed seeder was used. According to both authors, their seeder did not give enough powder supply and the particles tended to agglomerate.

Therefore, a new seeder was designed. It is based on a powder injector (PI-P1) from Wagner Group as shown in Fig. 5.5, which was originally designed for powder coating purposes. In cooperation with Wagner Group a powder container was designed that is suitable for elevated pressures using the PI-P1, see Fig. 5.6. The container and injector can be used up to a pressure of 5 bar absolute. The seeder is connected to the HPC by stainless steel tubing. Teflon tubing should be avoided, because particles are electrically charged by rubbing against it, which increases their stickiness.

The working principle of the device can be explained as follows: BAM powder is placed on top of the porous plate in the powder container. The porous plate is a 5 mm thick Nickel-Chromium metal foam (RECEMAT) with an average pore diameter of 0.4 mm. When the seeder valve (Hoke 7115G8YMM) is opened, a fluidized bed is created using N₂ coming in from the gas inlet. Due to the porous plate the velocity of the gas is almost evenly distributed and the BAM particles are fluidized. The particles suspended in the gas are sucked into the small channel of the center shaft towards the powder injector, due to a suction force induced by a venturi tube. N₂ is led through the injector nozzle and exits the nozzle with high velocity creating a low pressure in the suction tube. The suspended particles in the gas coming from the

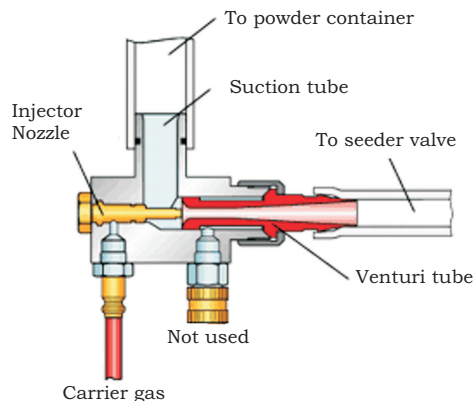


Figure 5.5: Schematic drawing of the Wagner Group PI-P1 powder injector (reproduced with permission from Wagner Group)[12].

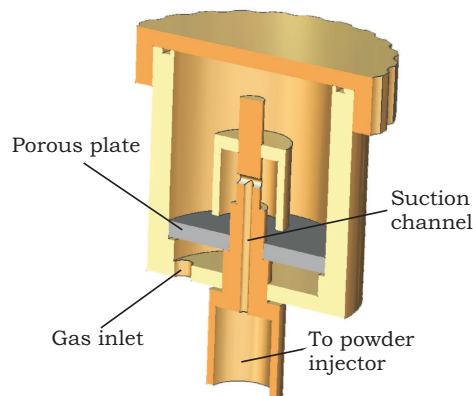


Figure 5.6: Structure of the newly designed powder container.

powder container, through the suction tube, are mixed with the carrier gas coming out of the nozzle. The particles are rapidly accelerated in the venturi tube, which introduces a shear force on the particles. This reduces particle agglomeration, which was confirmed by SEM data. A third supply of nitrogen can be used to dilute the particle concentration; this feature of the PI-P1 is not used in this work. The amount of particles being seeded into the HPC can be controlled by adjusting the pressure difference between the HPC and the seeder. In this work a pressure difference of 1 bar was used.

5.2.3 Optical setup

Interference filters are mounted in front of both cameras to select the appropriate regions of the emission spectrum (marked grey in Fig. 5.1). The filters are centered at 400 and at 457.9 nm and have a FWHM of 40 nm and 10 nm, respectively. The 400 nm filter is placed in front of the PI-MAX 2 and the 457.9 nm filter in front of the PI-MAX 3 camera. The ratio is computed by dividing the image of the PI-MAX 2 by the image of the PI-MAX 3 on a pixel-by-pixel basis, after background subtraction and flat fielding, see section 5.3. A Continuum PIV Powerlite laser operating at 5 Hz was used as a source to produce third harmonic 355 nm laser light for TP excitation.

The cylindrical laser beam was converted into a sheet using a series of lenses. The resulting sheet had a height of 90 mm and a thickness of 1 mm. The pulse energy was set to 29 mJ, which resulted in a fluence of 0.04 J/cm².

The cameras are set in 2×2 pixel binning mode to reduce the readout time and improve the signal-to-noise ratio. A resolution of 512×512 pixels is obtained, corresponding to a spatial resolution of ~0.2 mm/pixel.

5.2.4 Synchronization and data acquisition

The cameras and laser pulse were synchronized using a Stanford DG535 digital delay generator. The gating time of the synchronized cameras was set to 1 μs, which is close to the phosphorescence lifetime of BAM at room temperature. The pressure signal together with the gating signal produced by the cameras, was recorded at a rate of 100 kHz using a home-built TUE DACS data acquisition system controlled by a LabWindows program. The mass-averaged temperature at which the image was recorded was computed using the pressure and the trigger signal.

5.3 Aspects of quantitative measurements

The BAM particles need to fulfil certain criteria in order to be suitable as a TP. Besides, special attention has to be paid to the correction of ICCD camera images and evaluation of multiple scattering effects.

5.3.1 Particle suspension

In general, BAM particles will fall out of the gas in which they are suspended, because their density (3700 kg/m³) is significantly higher than that of the surrounding fluid (10, 15 or 20 kg/m³). The sedimentation speed is determined by a force balance between gravity, buoyancy and viscous friction (i.e. Stokes drag). Starting from a stagnant situation, the particles accelerate from zero to their final velocity within 2 ms. The vertical settling velocity is taken from [19] and given by:

$$v_p(R_p, \mu) = v_f + \frac{2(\rho_p - \rho_f)gR_p^2}{9\mu}, \quad (5.1)$$

with v_f the fluid velocity in vertical direction, ρ_p the particle density, ρ_f the fluid density, g the gravitational acceleration, R_p the particle radius and μ the dynamic viscosity of the gas mixture.

The TP particles are seeded in the beginning of the filling procedure, due to pressure limitations of the seeder. The time needed between seeding the particles and the start of the experiment is in the order of 100 s, depending on the required gas mixture density. The particles start to settle after they are seeded into the HPC with a velocity according to Eq. (5.1). The number of particles will decrease due to particles falling out of the field of view, which results in a decrease of phosphorescence signal. A simple signal intensity model is deployed below to predict the phosphorescence signal intensity at the start of the experiment, taking into account the time elapsed between seeding and start of pre-combustion.

In BAM, the phosphorescent activator Europium is doped in a microcrystalline host material, Barium Magnesium Aluminate, which is mostly transparent to incoming radiation [4, 20]. Therefore, it is assumed that the phosphorescence radiation is proportional to the particle volume. The signal prediction model uses this assumption, together with the known particle distribution (Fig. 5.2) and the settling velocity given by Eq. (5.1). It is assumed that the velocity of the gas in all directions is zero, the particles are initially distributed homogeneously over the volume of the HPC and there are no particles sticking to the walls. Particles which reach the bottom do not contribute to the signal anymore. The normalized volume concentration of particles of one size in a specific volume with height h_{HPC} is given by:

$$\phi_p(R_p, \mu, t) = 1 - \frac{v_p(R_p, \mu)t}{h_{HPC}}. \quad (5.2)$$

To prevent ϕ_p from becoming negative (since particles can not pass through the bottom of the HPC) as a function of time t , a shape function is introduced:

$$S(R_p, \mu, t) = \begin{cases} \phi_p & \phi_p > 0 \\ 0 & \phi_p \leq 0 \end{cases} \quad (5.3)$$

At a certain moment t the total volume of suspending particles at radius R_p yields:

$$dV(t) = V_{tot} Y_V(R_p) S(R_p, \mu, t) dR_p. \quad (5.4)$$

The particle distribution $Y_V(R_p)$ is given by Fig. 5.2. V_{tot} is the initial total volume of particles in the HPC. So the total volume of particles that is still suspending in the HPC is the integral of $dV(t)$ over all particle size from zero to the largest particle radius $R_{p,max}$. The intensity decay can now be calculated using:

$$I_b(\mu, t) = I \frac{V_{tot}}{V_{HPC}} \int_0^{R_{p,max}} S(R_p, \mu, t) Y_V(R_p) dR_p, \quad (5.5)$$

with I the emitted phosphorescence radiation per unit volume, and V_{HPC} the volume of the HPC.

Two experiments, with different dynamic viscosities of the gas mixture, were performed to validate the model. The dynamic viscosity was changed by adapting the gas mixture temperature. Particles were seeded into the HPC filled with pure N_2 and excited by 355 nm laser radiation. The phosphorescence signal was registered by an ICCD camera during 6 minutes. The results are normalized and presented together with model predictions in Fig. 5.7.

The model predictions show good agreement with the experimental results. The difference between model and experiment could be significantly reduced by adopting a 25% increase in v_p . The difference between experimental results and model predictions was not further investigated. A possible explanation could be a vortex, which is introduced when the particles are seeded from the bottom left corner of the HPC.

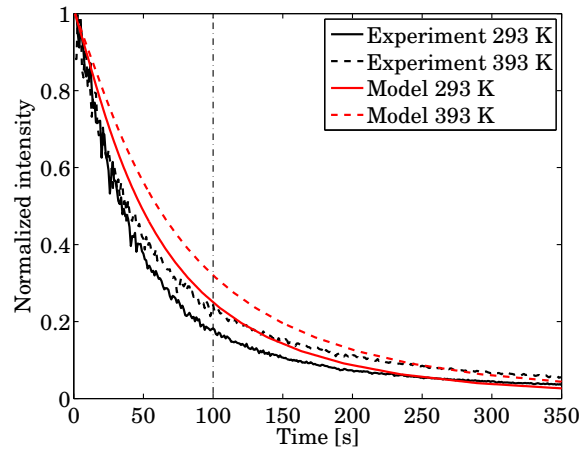


Figure 5.7: Intensity decay, model predictions compared with experimental results for two values of μ at two temperatures. A typical time delay between seeding and start of the actual experiment is about 100 s.

It can be concluded that the time between seeding the particles and conducting the experiment, should be kept to a minimum in order to achieve high signal intensities: the phosphorescence signal intensity is already reduced by $\sim 80\%$ after 100 s of particle settling. For this reason the experiments that are conducted at low mixture densities enjoy more signal, since then the filling time is relatively short.

5.3.2 Particle response time to temperature changes

The time scale in which the particles equilibrate with the local gas temperature should be fast enough to correctly reflect temperature variations in the gas. Also, the temperature in the particles themselves must be homogeneous, since the signal intensity scales with the volume of the particle. The Biot number is used to determine whether the temperature in a particle is homogeneous [21]:

$$Bi = \frac{hL_c}{k_p} \quad (5.6)$$

with h the convective heat transfer coefficient, L_c the characteristic length defined for a sphere written as $L_c = R_p/3$ and k_p the thermal conductivity of the particle equal to $24.2 \text{ W}/(\text{m}\cdot\text{K})$ [20]. Using the Nusselt relation for heat transfer by conduction from a spherical surface to a stationary, infinite medium around the surface [21];

$$Nu = 2h \frac{R_p}{k_f} = 2, \quad (5.7)$$

the Biot number is found to be much smaller than unity for all experimental conditions in this work. Therefore, the assumption of a homogeneous particle temperature is valid and the heat transfer equation can be simplified to calculate the temperature response time:

$$hA_p(T_\infty - T_p) = c_p \rho_p V_p \frac{dT_p}{dt}. \quad (5.8)$$

Where $A_p = 4\pi R_p^2$ is the surface area of the particle, T_∞ the temperature of the surrounding fluid, T_p the temperature of the particle, c_p its specific heat capacity, ρ_p its mass density and $V_p = \frac{4}{3}\pi R_p^3$ the volume.

The response time can be calculated by solving Eq. (5.8) using $Nu = 2$ [21], yielding

$$t = \frac{\rho_p R_p^2 c_p}{3k_f} \ln \frac{T_p - T_\infty}{T_d - T_\infty}, \quad (5.9)$$

where k_f is the thermal conductivity of the gas and T_d the desired temperature. T_d is set to be 95% of T_∞ . At 2300 K the response time is 145 μs with $k_f = 32 \cdot 10^{-3}$ W/m·K, $R_p = 1.3 \mu m$. The c_p of BAM is not known, therefore the heat capacity of Aluminum Oxide (Al_2O_3) was used (777 J/(kg·K)).

The bulk average temperature of the residual gas in the HPC heats up to 2300 K within a second during a pre-combustion event, then cools down gradually. At about 800 K the residual gas cools down with a rate of ~ 200 K/s. A response time of 145 μs is fast enough to follow the temperature of the gas sufficiently accurately.

5.3.3 Laser-induced heating

Compared with surface temperature measurements, the volume density of TP is much lower here, so higher laser fluence is required to obtain sufficient signal. The influence of the excitation laser on heating the particles should be investigated. Lindén et al. [15] performed experiments to investigate the heating effect and concluded that there is no indication of particles themselves being heated by the excitation laser up to a laser fluence of 1.5 J/cm². In this work a laser fluence of 0.04 J/cm² is used, which is well below that threshold value.

5.3.4 Particle influence on the pre-combustion

During the pre-combustion, energy is added to the system, i.e. chemical energy is converted to sensible heat. Hence the temperature of the gas mixture increases, governed by the heat capacity of the mixture. The particles suspended in the gas change the total heat capacity:

$$c_{total} = \frac{m_{gas}}{m_{gas} + m_p} c_{v,gas} + \frac{m_p}{m_{gas} + m_p} c_p \quad (5.10)$$

with m_{gas} the mass of the gas mixture, $c_{v,gas}$ the isochoric heat capacity of the gas mixture, m_p the total mass of the particles and c_p the specific heat capacity of the particles.

The following experiment was performed to determine the total mass of the particles suspended in the mixture. A sheet with adhesive tape is placed inside the HPC. The mass of the sheet before and after injection of TP particles is measured. Prolonged

waiting time is applied to be sure that all the particles are settled when the mass of the sheet is determined. The experiment was repeated four times. A total of 0.025 g TP particles is seeded into the HPC each experiment, which will change the total heat capacity, given by Eq. (5.10), by 0.04%, which is negligible.

5.3.5 Spatial alignment

The ICCD cameras are placed on opposite sides of the HPC and are focused on a common plane in the center, coincident with the laser sheet. To compute the spectral intensity ratio correctly, the cameras need to look at the same location of the laser sheet. Therefore, after globally adjusting the positions of the cameras, the raw images were morphed using a spatial alignment grid. A grid with reference points was placed inside the HPC in line with the laser sheet. Both cameras were focused onto the grid and images of the grid were taken. The reference points were coupled by using a linear conformal transformation, which accounts for translation, rotation and scaling. Besides morphing also 15×15 pixel median filtering was applied to smoothen the images (image filtering), which reduces the lateral spatial resolution to 3 mm.

5.3.6 Flat-fielding

The photocathode, phosphor screen and CCD chip pixels of the camera may all react differently to incoming radiation. To account for this difference, images are corrected for pixel-to-pixel sensitivity differences using a flat-field image, obtained by exposing the cameras to a light source which uniformly illuminates them, for example an integrating sphere. In this work the flat-field images were obtained with defocused camera lenses and a white piece of paper which was illuminated by a white light source.

Accurate flat-fields are the key to accurate temperature results, to avoid systematic errors in the ratio calculation. Lens aberrations and vignetting are also included in the flat-fields when they are obtained with the lenses fitted to the cameras.

There are indications that the flat-fields are wavelength dependent. Therefore, the flat-field images are obtained with the interference filters mounted in order to exclude possible wavelength dependencies.

In Fig. 5.8(a) the flat-field image of the PI-MAX 2 camera is shown and in Fig. 5.8(b) of the PI-MAX 3 camera. The difference in pixel sensitivity is clearly visible in both images together with the vignetting effect in the corners.

5.3.7 Background correction

The raw images are corrected for background signal, which consists of various sources. The background contains dark current and signal which can not be contributed to phosphorescence originating from excited particles in the laser sheet. Separate experiments have shown that fluorescence of the pre-combustion residual gas itself can be neglected.

The mean phosphorescence intensity during an experiment is presented in Fig. 5.9. The images which are lacking phosphorescent signal, i.e. above 1200 K, are used to determine the background, since all the phosphorescence radiation in the sheet is assumed to be lost. Non-radiative relaxation due to vibrations of the surrounding host

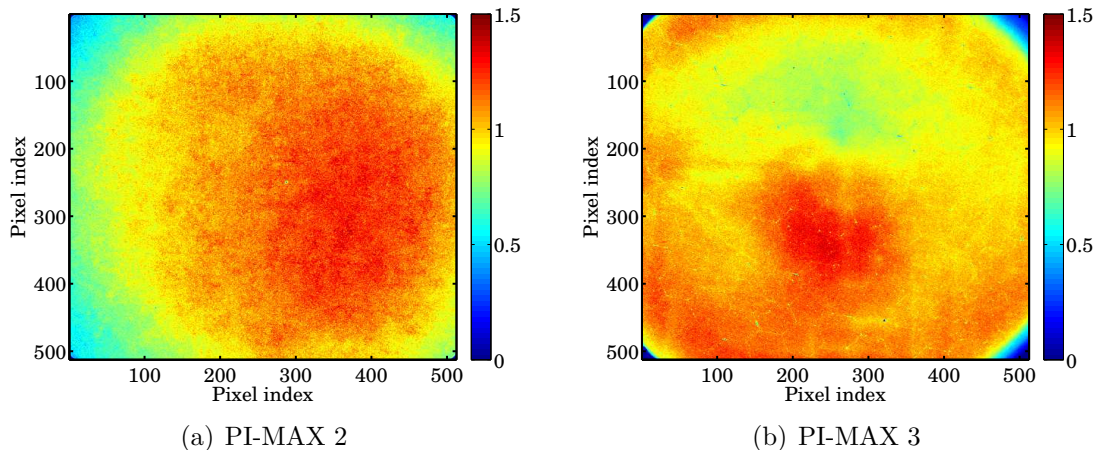


Figure 5.8: Flat-field image for both cameras with in color the correction factor. The correction factor is obtained by uniformly illumination of the cameras, applying dark current correction and dividing by the mean pixel value.

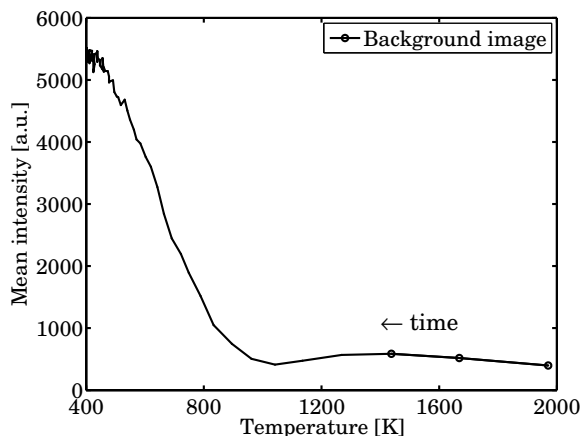


Figure 5.9: Mean phosphorescence signal intensity vs the mass-averaged temperature during an experiment, time is running from right to left. The locations of the selected background images are marked with black dots.

lattice, i.e. phonon quenching, can give an explanation for the loss of signal. Only the phosphorescence signal from relatively cool BAM particles sticking to the cooler walls is present. For this reason, three images at temperatures above 1200 K were averaged and used as background and subtracted pixel-by-pixel from the raw images. This background determination method was used in all the temperature measurement experiments.

5.3.8 Camera linearity

The linearity of the used ICCD cameras was investigated as well. Lindén et al. [16] investigated the behavior of a Princeton Instruments PI-MAX 2 ICCD camera. They concluded that the multi-channel-plate in the camera saturates before the end of the dynamic range of the CCD-chip is reached. The number of counts at which the camera saturates is different for each individual camera. For this reason it is advised

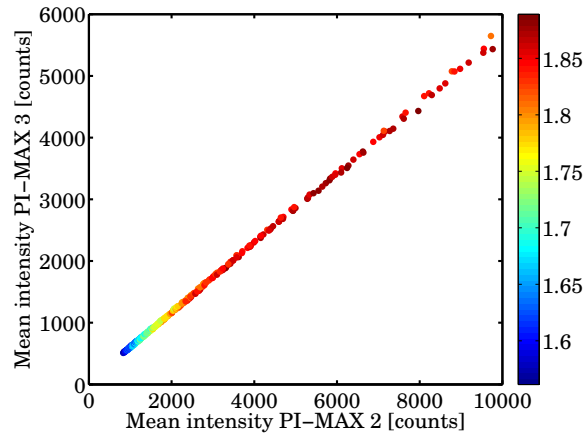


Figure 5.10: Averaged ratio (color) vs signal intensities for both cameras. Results shows a steady ratio above 2500 counts for the PI-MAX 2 and 1500 for the PI-MAX 3.

to investigate the linearity prior to experiments.

The cameras are fitted with lenses which have a standard f-stop scale, changing the effective lens opening by a factor of two for every stop. The linearity was investigated by exposing the cameras to a white light source and changing the diaphragm. The PI-MAX 2 camera was found to respond linearly up to $6 \cdot 10^4$ counts. The PI-MAX 3 camera, however, is only linear up to $2 \cdot 10^4$ counts. Pixel information should be discarded when the number of counts exceeds the linear range.

5.3.9 Signal intensity

For TP particles at a fixed temperature, the spectral intensity ratio should not depend on the actual signal levels. In order to check this, BAM particles are seeded into the HPC, which is filled with pure nitrogen. During 6 minutes, images are captured at a rate of 1 image per second, while the temperature is kept constant at 293 K. The signal reduced over time due to sedimentation of the TP particles. Besides the spectral intensity ratio, also the mean ratio and the mean phosphorescence intensity are calculated for each image. The mean ratio is plotted in color against the mean intensities of the two cameras and depicted in Fig. 5.10. The mean ratio is the mean of all individual ratios present in the sheet and is given by:

$$\bar{R} = \frac{1}{N_p} \cdot \sum_{x,y} R_{x,y} \quad (5.11)$$

with $R_{x,y}$ the local ratio as function of pixel coordinates and N_p the number of pixels. The mean ratio is by definition not equal to the ratio of the mean phosphorescence intensities of the cameras.

In Fig. 5.10, the mean ratio varies within 4%, when the intensity exceeds 2500 counts for the PI-MAX 2 and 1500 counts for the PI-MAX 3 camera. Below these values, the ratio varies more due to low signal-to-noise ratio. Together with the conclusion from the previous section, the number of counts I_c must fulfil; $2500 < I_c < 60000$ for the PI-MAX 2 and $1500 < I_c < 20000$ for the PI-MAX 3 camera.

5.3.10 Multiple scattering

The LIP technique in the gas phase, using phosphorescent particles, is potentially affected by multiple scattering. Ideally, the laser radiation only excites those phosphorescent particles present in the laser sheet. Next, their phosphorescence is detected by the ICCD camera without scattering by other particles. In practice, however, elastically scattered laser light may excite phosphorescence particles outside the nominal laser light sheet, and/or phosphorescence may reach the detector indirectly after scattering off other particles. In Fig. 5.11 the result of an experiment to indicate the degree of multiple scattering is presented. BAM particles were seeded into the HPC and excited by a thin laser light sheet. The height of the sheet was determined by a single slot, which resulted in a clearly defined sheet with sharp edges. The intensities observed along an arbitrary vertical line through the laser sheet are presented in Fig. 5.11.

In principle, the slot would limit the laser light sheet to between the dashed lines; multiple scattering causes the wings on both sides.

Multiple scattering can involve two possible scenarios: scattering of phosphorescence by other BAM particles, or elastic scattering of incoming radiation followed by excitation and phosphorescence of BAM particles outside the laser light sheet.

Which scenario is dominant cannot be decided from the obtained images. On just the basis of wavelength, scattering of laser light may be a factor of about two more efficient than that of the phosphorescence. Both scenarios effectively reduce spatial resolution, but in not quite the same way. Scattering of laser light within the light sheet itself has no effect on resolution, but scattering perpendicular to this plane effectively increases the excitation light sheet thickness. Scattering of phosphorescence, on the other hand, reduces spatial resolution when it occurs within the illuminated plane, but not so much when it occurs along the camera line of sight.

The width of the wings in Fig. 5.11 is a measure for the amount of multiple scattering, and can also be used to estimate the loss of resolution that multiple scattering causes along the line of sight. On both sides of the nominal light sheet (dashed lines in Fig. 5.11) the wings extend by about 25 pixels (half width). If we assume the scattering to be isotropic, the same increase also occurs along the line of sight. This then reduces the spatial resolution along that direction to 50 pixels \equiv 10 mm, a factor of about 10 larger than the nominal thickness of the laser light sheet. Note that in this scenario the resolution within the plane of the light sheet is unaffected if scattering of the laser light dominates (it remains determined by the image filtering).

Nevertheless, the contribution of scattering of phosphorescence radiation should not be excluded. The spatial resolution of the temperature field is decreased in all directions when the phosphorescence radiation is scattered. We assume that the decrease of spatial resolution by this mechanism is in the same order as the image filtering, and therefore is already taken into account.

Reducing the seeding density will result in less multiple scattering, but also reduces the phosphorescence signal. This can be compensated by seeding larger particles into the gas mixture. However, these particles will have a higher settling velocity which results in a shorter suspension time. Also, bigger particles will respond slower to changes in the local gas temperature. The seeding density, particle size and experimental conditions should be carefully adjusted to give an acceptable level of multiple

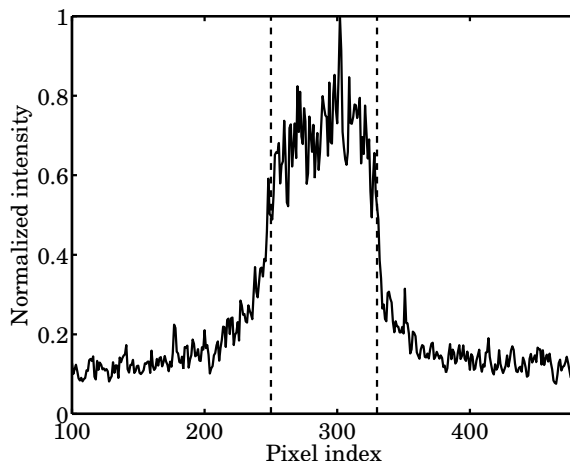


Figure 5.11: Blurred phosphorescence intensity profile due to multiple scattering. In the absence of scattering, laser light would be present between the dashed lines only; multiple scattering causes the wings on both sides.

scattering.

A promising method to reduce the influence of multiple scattering is the Structured Laser Illumination Planar Imaging (SLIPI) technique [22]. The ultra-fast SLIPI for single-shot imaging [23] can probably contribute to a reduction of multiple scattering. Three successive images with different light structure are combined to form one image wherein the multiple scattering is drastically reduced. The radiation due to elastic scattering is only present during the laser pulse, whereas in the LIP technique the phosphorescence radiation is present during the whole lifetime of the phosphor. Therefore, the time step between the three successive images should be longer than the lifetime of the phosphorescence.

5.4 Calibration

The translation of spectral intensity ratio into temperature requires a calibration step. In this work the HPC itself was used for calibration, by using all successive image ratios after the pre-combustion, together with the bulk temperature evolution. In Fig. 5.12 the temperature evolution of a pre-combustion experiment together with the timing of the ratio images is shown. The temperature decay curves are highly repeatable.

For each ratio image the mean ratio within the laser sheet was determined according to Eq. (5.11). It is assumed that the mean temperature in the sheet is equal to the bulk temperature. In this way the mean ratio of each image can be related to the bulk temperature, which results in a calibration curve.

The results become imprecise above ~ 650 K, due to low signal intensity. The calibration procedure was repeated multiple times for each gas density (10, 15 and 20 kg/m^3) to determine the accuracy. The calibration data of these experiments were fitted using a fourth order polynomial for each gas density, see Fig. 5.13. The amount of products and reactants present in the cell is presented in Table 5.1. The ratio-temperature relation of the 15 and 20 kg/m^3 series coincide within experimental uncertainty, the

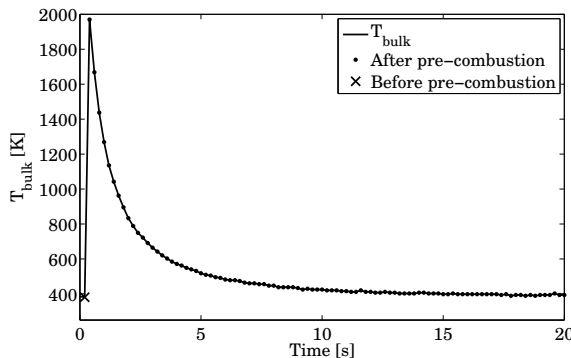


Figure 5.12: Temperature evolution of a pre-combustion experiment plotted together with the timing of the ratio images, before and after the pre-combustion.

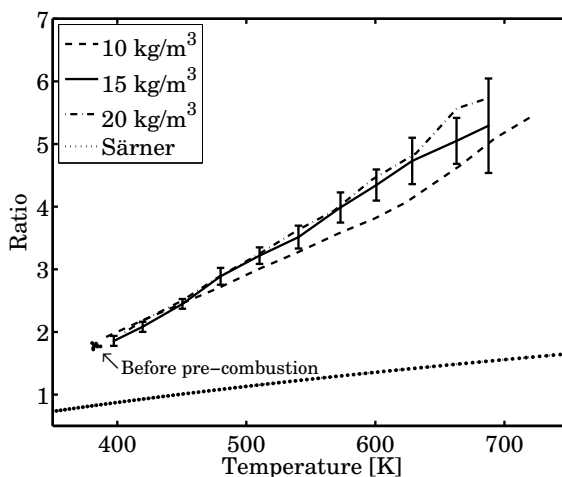


Figure 5.13: Ratio-temperature relation for different gas densities compared to literature data from Särner [4]. The cloud of data points in the lower left corner are obtained from measurements before pre-combustion.

curve for 10 kg/m^3 series deviates slightly. A temperature precision of 30 K at 393 K increasing to 60 K at 650 K is obtained.

Särner determined the ratio-temperature relation for surface temperature measurement, using BAM as TP [4]. There is no literature data available for BAM particles in the gas phase. In Fig. 5.13 the obtained ratio-temperature relations for the three different gas densities are depicted together with the data from Särner [4]. The ratios obtained by Särner are much smaller than ours, probably because different optical components are used.

5.4.1 Survivability

BAM particles are reported to undergo degradation upon heating, since the Eu atoms change from a divalent state to a trivalent state when exposed to temperatures above 800 K [17]. Degradation results in a change in the emission spectrum resulting in incorrect temperature information. It is unclear whether the transient high temperature of the pre-combustion influences the BAM characteristics, since the degradation is slow according to Bizarri and Moine [17].

The seeded BAM particles have not yet been exposed to high temperatures before the pre-combustion. Therefore, the ratio images before pre-combustion were used to check the degradation effect. These form the ‘cloud’ of data points in the lower left of Fig. 5.13. It is clear that the transient high temperature of the pre-combustion does not change the emission characteristics of BAM particles, since data obtained before pre-combustion coincide with the calibration curve obtained after pre-combustion.

5.5 Results and discussion

Experiments were performed to determine the temperature field in the HPC at three different gas densities (10, 15 and 20 kg/m³). Experiments were repeated at each condition. BAM particles were seeded into the HPC, time between seeding and the actual start of experiment was kept to a minimum to have as much signal as possible. The temperature distributions during the cooling phase were calculated using the ratio-temperature calibration curve. Images are recorded for 20 seconds at 5 Hz.

A 2D temperature distribution at 4.4 seconds after the pre-combustion is shown in Fig. 5.14. The density of residual gas is 10 kg/m³ and the bulk averaged temperature is 559 K. The edges of the laser light sheet are indicated by black lines. Outside of it, the TPs are also excited due to multiple scattering. The temperature distribution in the image shows that the top part of the HPC is hotter than the center and bottom parts. All other experiments show a similar temperature gradient in vertical direction. This is undoubtedly due to buoyancy of the hot pre-combustion gases. In the horizontal direction, the temperature gradient is much smaller.

Three locations in the temperature field were selected; they are marked with red circles in Fig. 5.14. The distance between adjacent locations is approximately 30 mm. The temperature evolution at the three points is plotted in Fig. 5.15. Results above 650 K are discarded because of low signal. The temperature at the three points is averaged over three experiments. Strong temperature fluctuations can still be observed, probably caused by the turbulent flow in the HPC. The temperature difference between top and bottom points is about 150 K at 4 s, which gradually decays during the cooling process.

Fig. 5.16 shows the scaled temperature evolution at the three locations. At 590 K, the top location is about 8% hotter than the center location, while the bottom location is about 15% colder than the center location. Since the distance between adjacent locations is the same, the temperature gradient in the top half of the HPC is smaller than that in the lower part.

Unfortunately, the presented BAM-LIP results are all in the condition of fan-off, which means it currently can not provide the 2D temperature distribution prior to the fuel injection, which normally are in the fan-on condition. The major limitation is the long filling procedure of the HPC. Since the seeding device can not stand more than 5 bars, the TPs have to be seeded early in the filling procedure. The mean intensity decreases by 80% due to the sedimentation of the TPs. The mixing fan can not be turned on as during spray measurements, since this accelerates the deposition of TPs on the cell walls.

A possible improvement is to seed the TPs just before pre-combustion with a high pressure seeder, so the volume density of particles remains high.

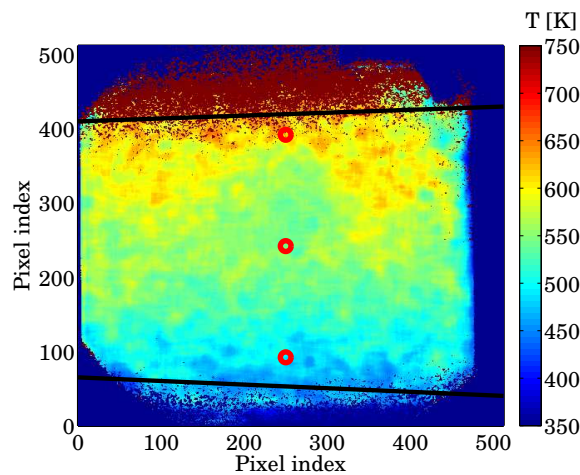


Figure 5.14: Temperature (color) distribution in the residual gas of the HPC at 4.4 s after the start of pre-combustion. ($T_{bulk} = 559$ K); black lines mark the edges of the sheet; spot temperatures are followed in Fig. 5.15.

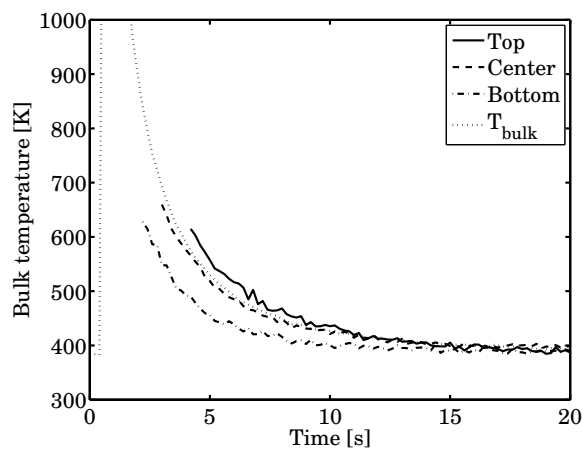


Figure 5.15: Temperature evolution for three different locations in the HPC within the laser sheet, plotted together with the bulk temperature.

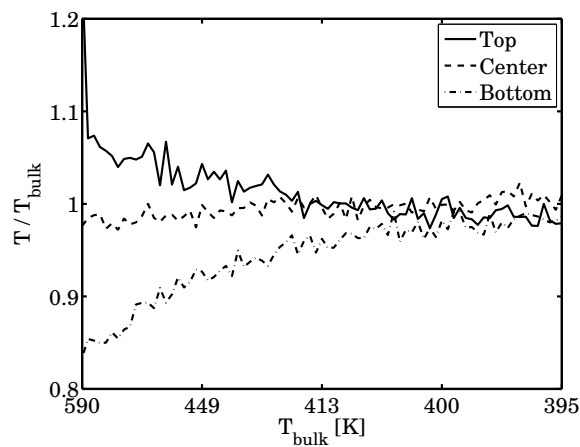


Figure 5.16: Relative temperature evolution for the three different locations.

5.6 Conclusions

The feasibility of the LIP technique for determining the 2D temperature field in the HPC was investigated. The following conclusions can be presented, emphasizing the potential of the LIP technique in the gas phase:

- BAM particles are suitable for TP seeding in the gas phase; the signal intensity is relatively strong due to the high quantum yield.
- BAM particles are not affected by the transient high temperature of the pre-combustion; they can withstand high temperatures for a short period of time (seconds), despite the fact that the particles undergo degradation at higher temperatures according to Bizarri and Moine [17].
- Particle sticking is not a major concern as long as stainless steel tubing is used and Teflon material is avoided. It is advised to use SiO₂ coated particles to reduce the stickiness [15].
- The BAM particles stay suspended in the gas just long enough to investigate the feasibility of the LIP technique. When the experiments were performed at higher gas densities, the signal decreased significantly due to particles falling out of the gas during the comparatively longer gas fill duration. A simple model was created and implemented to describe the gradual, size-dependent settling of the seeded particles. The model was validated using experimental results and can be used to predict the signal intensity at the start of experiment as function of the filling time.
- The powder injector and the designed powder container performed beyond expectations. No particle agglomerations were present as confirmed by SEM, probably due to the high shear forces induced.
- The spatial resolution was estimated to 3 mm in the illuminated plane and 10 mm along the line of sight. The spatial resolution is primarily affected by multiple scattering. A higher spatial resolution can be obtained when multiple scattering is reduced, for instance by using a lower number concentration of larger particles or SLIPI.
- A temperature precision of 30 K at 393 K increasing to 60 K at 650 K is obtained.
- Temperature field results show that there is a significant temperature gradient in vertical direction during the cooling phase in the HPC when the mixing fan is not used. The temperature difference (for example, 150 K after 4 s of cooling) is caused by hot gases moving to the top of the cell due to buoyancy.
- Unfortunately, the presented BAM-LIP results are all in the condition of fan-off, which means it currently can not provide the 2D temperature distribution prior to the fuel injection, which normally are in the fan-on condition. The major limitation is the long filling procedure of the HPC.

Bibliography

- [1] D.L. Flowers, S.M. Aceves, and A. Babajimopoulos. Effect of charge - non-uniformity on heat release and emissions in PCCI engine combustion. *SAE Technical Paper*, 2006-01-1363, 2006.
- [2] W.L. Hardy and R.D. Reitz. A study of the effects of high EGR, high equivalence ratio, and mixing time on emissions levels in a heavy-duty diesel engine for PCCI combustion. *SAE Technical Paper*, 2006-01-0026, 2006.
- [3] R.S.G. Baert, P.J.M. Frijters, L.M.T. Somers, C.C.M. Luijten, and W.A. de Boer. Design and operation of a high pressure, high temperature cell for HD diesel spray diagnostics: guidelines and results. *SAE Technical Papers*, 2009-01-0649, 2009.
- [4] G. Särner. *Laser-Induced Emission Techniques for Concentration and Temperature Probing in Combustion*. PhD thesis, Lund University, 2008.
- [5] S.W. Allison and G.T. Gilles. Remote thermometry with thermographic phosphors: Instrumentation and applications. *Rev. Sci. Instrum.*, 68(7):2615, 1997.
- [6] J. Brübach, J. Zetterberg, A. Omrane, Z.S. Li, M. Aldén, and A. Dreizler. Determination of surface normal temperature gradients using thermographic phosphors and filtered Rayleigh scattering. *Applied Physics B: Lasers and Optics*, 84: 537–541, 2006. ISSN 0946-2171.
- [7] A.L. Heyes, S. Seefeldt, and J.P. Feist. Two-colour phosphor thermometry for surface temperature measurement. *Optics Laser Technology*, 38(4 - 6):257 – 265, 2006.
- [8] M. Aldén, A. Omrane, M. Richter, and G. Särner. Thermographic phosphors for thermometry: A survey of combustion applications. *Progress in Energy and Combustion Science*, 37(4):422 – 461, 2011. ISSN 0360-1285.
- [9] J. Brübach, A. Dreizler, and J. Janicka. Gas compositional and pressure effects on thermographic phosphor thermometry. *Measurement Science and Technology*, 18(3):764, 2007.
- [10] J.P. Feist, A.L. Heyes, and S. Seefeldt. Oxygen quenching of phosphorescence from thermographic phosphors. *Meas. Sci. Technol.*, 14(5):N17, 2003.
- [11] R. Hasegawa, I. Sakata, H. Yanagihara, B. Johansson, A. Omrane, and M. Aldén. Two-dimensional gas-phase temperature measurements using phosphor thermometry. *Applied Physics B: Lasers and Optics*, 88, 2007.
- [12] Wagner Group website. <http://www.wagner-group.de>, May 2011.
- [13] M. Yu, G. Särner, C.C.M. Luijten, M. Richter, M. Aldén, R.S.G. Baert, and L.P.H. de Goey. Survivability of thermographic phosphors (YAG:Dy) in a combustion environment. *Meas. Sci. Technol.*, 21(3), 2010.
- [14] S. Shionoya, H. Yamamoto, and W.M. Yen. *Phosphor handbook*. CRC Press, 2nd edition, 2007.

-
- [15] J. Lindén, N. Takada, B. Johansson, M. Richter, and M. Aldén. Investigation of potential laser-induced heating effects when using thermographic phosphors for gas-phase thermometry. *Applied Physics B: Laser and Optics*, 96(2-3):237–240, 2009.
- [16] J. Lindén, C. Knappe, M. Richter, and M. Aldén. Limitations of ICCD detectors and optimized 2D phosphor thermometry. *Meas. Sci. Technol.*, 23(3):035201, 2012.
- [17] G. Bizarri and B. Moine. On BaMgAl₁₀O₁₇:Eu phosphor degradation mechanism: thermal treatment effects. *Journal of Luminescence*, 113(34):199 – 213, 2005.
- [18] A. Omrane, P. Petersson, M. Aldén, and M.A. Linne. Simultaneous 2D flow velocity and gas temperature measurements using thermographic phosphors. *Applied Physics B: Lasers and Optics*, 92:99–102, 2008.
- [19] M. Rhodes. *Introduction to Particle Technology*. Wiley, 1998.
- [20] M.J. Weber. *Handbook Of Optical Materials*. CRC Press, 2003.
- [21] F. Incropera, D. DeWitt, T. Bergman, and A. Lavine. *Introduction to heat transfer*. Wiley, fifth edition, 2007.
- [22] E. Berrocal, E. Kristensson, M. Richter, M. Linne, and M. Aldén. Application of structured illumination for multiple scattering suppression in planar laser imaging of dense sprays. *Opt. Express*, 16(22):17870–17881, 2008.
- [23] E. Kristensson, E. Berrocal, M. Richter, and M. Aldén. Ultra-fast Structured Laser Illumination Planar Imaging (SLIPI) for single-shot imaging of dense sprays. International Annual Conference on Liquid Atomization and Spray Systems, ICLASS, September 2009.

Table 5.1: Mixture composition at different densities

Density [kg/m ³]	Species	Reactant [mg]	Product [mg]
10	C ₂ H ₂	473	-
	O ₂	1309	-
	N ₂	9568	9568
	Ar	1194	1194
	CO	-	255
	CO ₂	-	1200
	H ₂ O	-	328
15	C ₂ H ₂	684	-
	O ₂	1943	-
	N ₂	14069	14069
	Ar	1728	1728
	CO	-	277
	CO ₂	-	1876
	H ₂ O	-	473
20	C ₂ H ₂	938	-
	O ₂	2490	-
	N ₂	18814	18814
	Ar	2298	2298
	CO	-	686
	CO ₂	-	2093
	H ₂ O	-	649

Gas phase temperature measurements using Toluene LIF

Planar laser-induced fluorescence (LIF) of toluene has been applied in an optical engine and a high-pressure cell, to determine temperatures of fuel sprays and in-cylinder vapors. The method relies on a red-shift of the toluene LIF emission spectrum with increasing temperature. Toluene fluorescence is recorded simultaneously in two disjunct wavelength bands by a two-camera setup. After calibration, the pixel-by-pixel LIF signal ratio is a proxy for the local temperature. A detailed measurement procedure is presented to minimize measurement inaccuracies and to improve precision. N-heptane is used as the base fuel and 10% of toluene is added as tracer. The toluene LIF method is capable of measuring temperatures up to 700 K; above that the signal becomes too weak. The precision of the spray temperature measurements is 4% and the spatial resolution 1.3 mm. We pay particular attention to the construction of the calibration curve that is required to translate LIF signal ratios into temperature, and to possible limitations in the portability of this curve between different setups.

The fuel spray results obtained in the high pressure cell are also compared to LES simulations. We find that the hot ambient gas entrained by the head vortex gives rise to a hot zone in the spray.

This chapter is an integral copy of the article which has been submitted to Applied Physics B: Lasers and Optics. Minor changes have been made to improve the quality.

R.P.C. Zegers*, M. Yu *, C. Bekdemir, N.J. Dam, C.C.M Luijten and L.P.H. de Goey, Planar toluene LIF to determine spray temperatures and fuel stratification in an optical engine and high pressure cell, *submitted to Applied Physics B: Lasers and Optics*, (2012).

* Both authors contributed equally to this work. Zegers is responsible for the engine experiments and Yu for the experiments conducted in the high pressure cell. The analysis of the experiments has been done by both researchers. The LES simulations have been performed by Bekdemir.

6.1 Introduction

Non-intrusive accurate 2D temperature measurements under high-temperature conditions as prevalent in internal combustion (IC) engines have been a challenge for the last decade. Mass-averaged temperature in engines can be derived quite accurately from the in-cylinder pressure evolution. However, temperature stratification resulting from injection of fuel into a cylinder filled with hot air cannot yet be measured accurately. Recent research suggests that toluene laser-induced fluorescence (LIF) is an appropriate measurement technique for measuring gas and vapor temperatures [1–3]. The principle of the technique is as follows. After excitation of toluene vapor by means of UV light (248 nm in our case), it emits fluorescence, the spectral distribution of which depends on temperature. After calibration, the ratio of integrated fluorescence intensities in two disjunct wavelength bands, provides a convenient measure for the local temperature. As with all ratio-based methods, this technique has the advantage that it is independent of the local excitation laser intensity and toluene density. A potential disadvantage, however, is that the calibration factor need not be constant over the whole field of view.

Toluene has a few advantages over other tracers: it has a high fluorescence quantum yield, a relatively large red shift as function of temperature and a lower toxicity than e.g. benzene [2, 4]. The influence of pressure is negligible [1]. A major disadvantage of toluene LIF is the decrease of its effective fluorescence lifetime with increasing temperature [5]. This is a result of fast depopulation of the excited state due to inter system crossing (ISC) [6]. Even with high excitation laser fluence, signal levels will decrease to noise levels at high temperatures (~ 700 K in our case) and therefore decrease the precision.

The applicability of the toluene LIF technique in an engine environment was investigated by only a few researchers. Luong et al. measured in-cylinder temperatures without fuel injection [7]. Mannekutla et al. showed the potential of the technique for fuel sprays [8], but results were tentative, probably due to fuel fluorescence or fuel decomposition in air. In our research, toluene LIF is used as a tool to measure temperatures during and after injection of fuel inside an optically accessible heavy-duty engine and a constant volume high-pressure cell. Toluene LIF is used because of the promising outlook of the technique and its relatively modest equipment requirements. Temperature stratification after spray injection is of major importance for partially premixed combustion (PPC) strategies in diesel engines. In the PPC regime, there is a finite time delay between end of injection and start of combustion, resulting in premixed fuel and air regions with various temperatures and fuel concentrations. Earlier toluene LIF studies have not aimed at measuring temperature stratification after fuel injection.

Cycle-to-cycle variations influence the mixture formation and therefore the time and location where combustion starts. Controlling the ignition event is a major research topic in the application of PPC combustion strategies in practical combustion engines. For this reason, we investigate the mixture properties by means of planar (2D) toluene LIF on the basis of single laser shots. The use of toluene LIF has the advantage that the toluene itself serves as a fuel tracer, whereas the redshift of its fluorescence is a temperature marker (for the vapor phase). In order to better interpret the data from the optical Diesel engine, we compare those results with measurements on a single

fuel spray in a constant-volume high-pressure cell with more extensive optical access, which in turn are compared with LES simulations.

6.2 Materials/Setup

In this research, two setups are used, being an optically accessible one-cylinder engine and a constant volume high-pressure cell (HPC).

6.2.1 Optically accessible engine

The engine setup consists of a one-cylinder optically accessible heavy-duty Diesel engine, based on a Ricardo Proteus block and equipped with a DAF MX cylinder head. The engine is driven by an electrical motor. A schematic layout of the complete setup is given in Fig. 6.1 and a cross-section of the engine is shown in Fig. 6.2. The piston is elongated, and the upper part of the liner and the piston bottom are both made of sapphire. Via an oval aluminium-coated mirror (Molenaar Optics), positioned under 45 degrees, optical access to the combustion chamber is obtained. The hydraulic cylinder can be lowered, allowing easy access to the combustion chamber for cleaning. For details of the engine we refer to [9]. Specifications are summarized in Table 6.1.

Table 6.1: Engine specifications, top dead center (TDC) is defined as 360 CAD (crank angle degrees).

Bore	130 mm
Stroke	156 mm
Connecting rod	270 mm
Displacement volume	2.07 liter
Compression ratio	13.9
IVO	715 CAD
IVC	190 CAD
EVO	500 CAD
EVC	10 CAD
Piston bowl/crown	Flat bathtub
Piston bowl diameter	90 mm
Piston bowl depth	20 mm

IVO = inlet valve opening, IVC = inlet valve closing, EVO = exhaust valve opening, EVC = exhaust valve closing.

The engine is equipped with both a port fuel injection (PFI) system (used for toluene injection in the intake manifold) and a common rail injector of Delphi Diesel Systems (used for fuel injection). Toluene is pressurized in a 100 ml vessel using compressed nitrogen at 4 bar and is directly connected to two PFI injectors which are controlled by a MOTEC M8 programmable motor management system. The distance between the PFI injectors and the inlet valve is approximately 50 cm. The details of the common rail diesel injector are presented in Table 6.2.

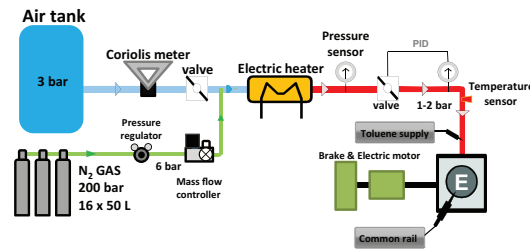


Figure 6.1: Schematic layout of the optical engine setup.

Table 6.2: Fuel injector specifications.

Holes	7
Hole size	195 μm
Flow (nominal)	1.7 l/min
Spray cone angle (ϕ)	143 degrees

Nominal flow as measured by Delphi Diesel Systems at 100 bar.

6.2.2 High-pressure cell

The HPC is essentially a constant volume combustion vessel dedicated to optical diagnostics on single fuel sprays. Its core is a cubic 1.25 liter combustion chamber produced by spark erosion inside a stainless steel cube. It is equipped with subsystems for heating, cooling, fuel injection, gas supply, computer control, data acquisition and optical diagnostics. Three sides provide optical access through large sapphire windows. A single fuel spray can be injected along a diagonal in a vertical plane (see schematic view in Fig. 6.3). Ambient conditions are created by means of the so-called pre-combustion technique: a combustible mixture of specifically tailored pressure and composition is ignited (the pre-combustion), which raises temperature and pressure in the HPC. The fuel spray is injected when the cell contents have cooled down to the desired conditions. The composition of the end gas of the pre-combustion determines

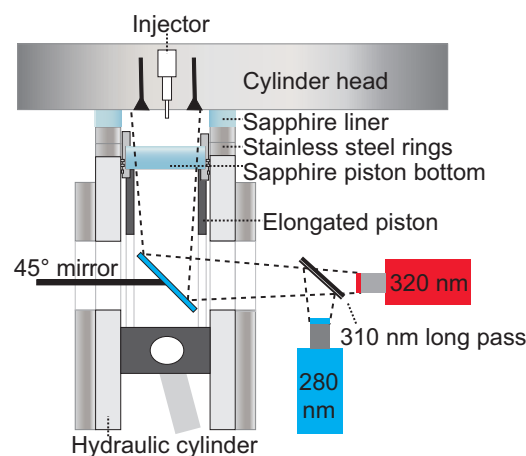


Figure 6.2: Cross-section of the optically accessible engine.

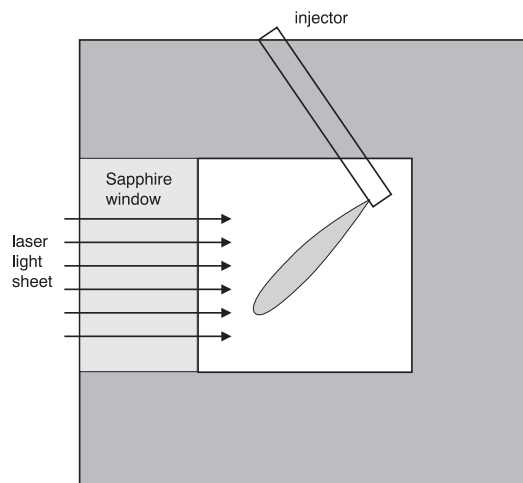


Figure 6.3: Schematic vertical cross section of the HPC, through the plane of fuel injection. Two more windows are at the front and back side of the cell, along a line perpendicular to the laser light sheet. The whole cell can be heated, and there is an internal fan to improve mixing.

whether the fuel spray is injected into an inert (no O_2 left) or oxidative (O_2 left) environment. A more detailed description of the HPC is provided by Baert et al. [10]; its main features are summarized in Table 6.3.

The gas supply system is based on four mass flow controllers, which enable filling pure gases one by one to prepare the gas mixture inside the HPC. The filling process is monitored by the gas pressure sensor. A mixing fan is used to enhance the mixing. We use C_2H_2 , O_2 , N_2 and Ar to form a mixture, which, once burned, produces the same density, O_2 mass fraction and heat capacity as those expected at the desired engine condition.

6.2.3 LIF setup

Each of the two toluene LIF setups contain two cameras which are used in various configurations, as described in the sections below. The specifications of the equipment are similar for all configurations.

General specifications

The components used in the toluene LIF setups are specified in Table 6.4. Both bandpass filters have a diameter of 50 mm to fit the UV lenses. Due to failure of camera 2, three different cameras have been used. These have been named camera 1 to 3. The transmission efficiencies of the used filters, lenses, sapphire windows and the dichroic beam splitter, as well as the reflection efficiencies of the aluminium-coated mirror and the quantum efficiency of the photocathode of the cameras over the wavelength range of interest are plotted in Fig. 6.4.

Table 6.3: Specifications of the HPC

Basic parameters	
Shape of the chamber	108×108×108 mm ³ (1.26 l)
Window size	50 mm thick, 100 mm diameter
Maximum pressure	300 bar (sapphire windows)
Heating and cooling system	
Wall temperature	293 K - 473 K
Fuel temperature	313 K - 423 K
Injector holder temperature	333 K
Fuel supply system	
Injector	Delphi single-hole nozzle
Injector coating	TiN coated
Nozzle hole size	150 μm
C_d	0.86 (at 800 bar)
C_m	0.77 (at 800 bar)
Sensors	
Gas pressure	Druck PMP 4070 (0-70 bar)
Injection pressure	Kistler 4067A5000
Pre-combustion pressure	Kistler 6041 AU20 (0-250 bar)

Table 6.4: The components of the toluene LIF setups

Laser	Lambda Physik, Compex 350T
Laser wavelength	248 nm
Toluene	Sigma Aldrich HPLC grade 99.6% pure
Dichroic beam splitter	310 nm long pass Semrock FF310-Di01
Bandpass filter 1	320 nm FWHM 43.8 nm Semrock BrightLine FF01-220/40
Bandpass filter 2	280 nm FWHM 22 nm Semrock BrightLine FF01-280/20
Lenses	Halle OUC 2.5, f = 100 mm, F# = 2
ICCD Camera 1	Princeton instruments PI-MAX 3
ICCD Camera 2	Princeton instruments PI-MAX 3
ICCD Camera 3	Princeton instruments PI-MAX 2
ICCD photocathode coating	unigen II
Camera resolution	16 bit

Illumination

For all experiments we use a light sheet derived from a broad-band KrF excimer laser (Lambda Physik Compex 350; nominal $\lambda = 248$ nm). In the HPC the laser light sheet contains the spray axis. In the optical engine this was not possible. Here, the horizontal light sheet enters the combustion chamber 5 mm below the cylinder head (Fig. 6.5). Its thickness varies between about 1 and 2 mm throughout the combustion

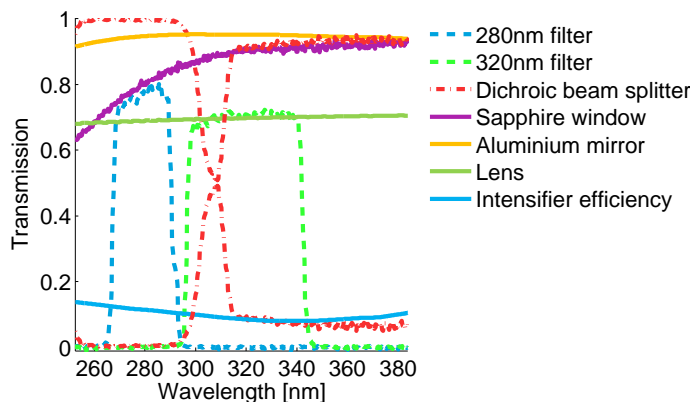


Figure 6.4: Transmission efficiencies, reflection efficiencies and photocathode quantum efficiency (QE) of the optical detection line. All values are based on manufacturer specifications.

chamber. Therefore, only a relatively small cross section of the fuel sprays is illuminated directly. However, in the actual measurements the apparent cross sections may be larger due to illumination by scattered laser light.

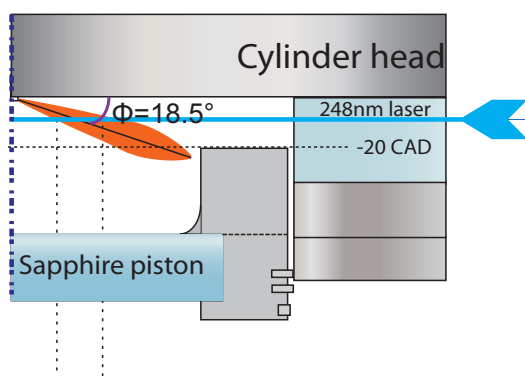


Figure 6.5: Spray image schematic in the optical engine, with the laser sheet in blue and the spray in red. The cone angle of the injector is 143° .

Camera configuration

The toluene LIF thermometry technique requires that two images be taken from the same event in two different wavelength ranges. The latter are indicated by the two boxes in the LIF spectra of Fig. 6.6. Acquiring these two images can be done either by one single camera or by two separate ones. The former has the advantage of minimized cost, but goes at the expense of spatial resolution and somewhat complicated measures for image separation (see, e.g., Ref. [11]). The latter is more flexible, and is the method chosen here. In both cases, the individual images have to be mapped onto each other, and corrected for pixel-to-pixel variations in sensitivity.

When using two cameras, they can be positioned on opposite sides or on the same side of the measurement volume; in the latter case a beam splitter can be used to separate the spectrum bands. The two strategies are shown in Fig. 6.7 for the HPC setup. A

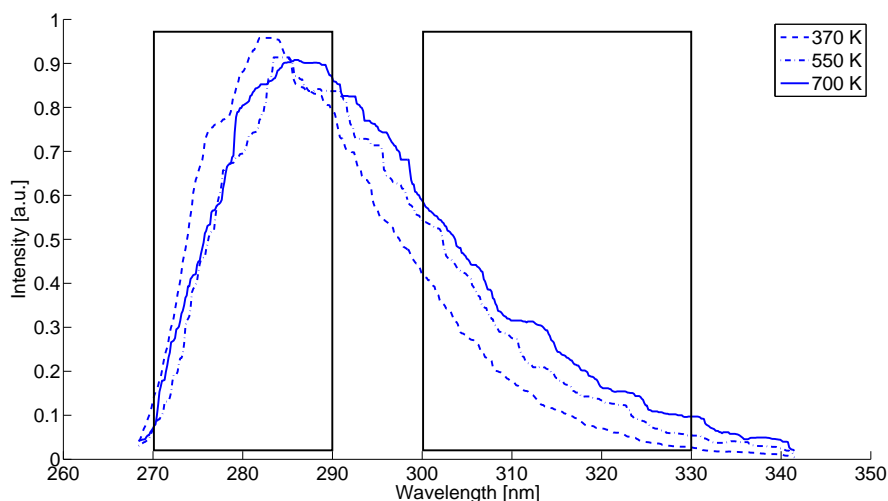


Figure 6.6: Normalized toluene LIF spectrum at three different temperatures. The two boxes indicate the wavelength regions of the two cameras.

same-side camera configuration requires only one path for optical access eliminating probable differences. A disadvantage of the same-side camera configuration is the requirement of a (dichroic) beam splitter to split the signal into two parts or two wavelength ranges. A regular beam splitter will transmit or reflect a part of the total signal only, which reduces the sensitivity. A dichroic beam splitter will in theory reflect and transmit the wavelengths of interest but needs to be positioned precisely to avoid a difference in wavelength reflection. An opposite side camera configuration on the other hand avoids the use of the dichroic beam splitter, and the cameras can be positioned closer to the setup. A drawback of the opposite site arrangement is the difference in line-of-sight of both cameras. Since both pre-combustion and the spray penetration involve strong turbulence, the difference in light path may induce distortion in the images, decreasing the spatial resolution. A two-side camera configuration has been used previously in [3?] and did not reveal any major drawbacks. For the experiments on the optical engine, the same-side configuration is the only option. On the HPC, however, both options are possible. We there have tested both approaches, using a dichroic (rather than a broad-band) beam splitter to split the fluorescence immediately into the desired wavelength ranges. As it happens, the optical characteristics of the dichroic beam splitter are sensitive to the angle of incidence of the light, which may vary over the field of view if the object is not at infinity. The implications of this effect for the temperature calibration will be discussed further below (Section 6.5.2).

6.3 Aspects of quantitative measurements

To perform accurate toluene LIF measurements, special attention has to be paid to several aspects concerning the equipment and measurement procedure. In particular, the potentially most serious pitfall of allegedly spectrally resolved measurements through spectral band-pass filters, rather than a spectrograph, is that the informa-

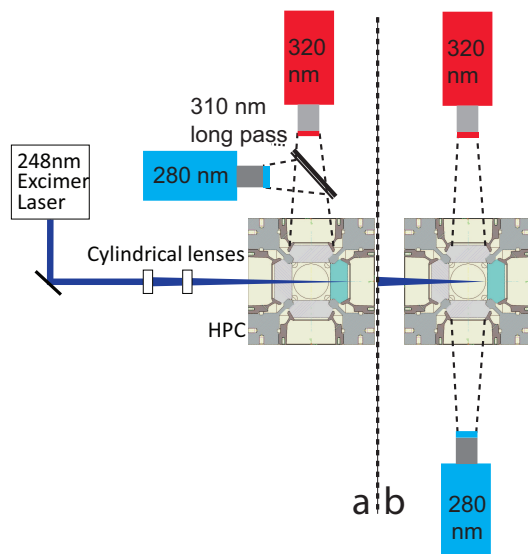


Figure 6.7: Schematic view of both camera configurations in the HPC setup. a) one side setup b) opposite side setup

tion of the spectrum is in fact lost. The interpretation of the light intensity measured behind the band-pass filters necessarily relies on the assumption that the underlying spectrum has not been compromised. (This complication, of course, pertains to measurements through band-pass filters in general, not just to the present toluene LIF measurements.) Various aspects will be systematically described and discussed in the following subsections. Data processing steps are given in Appendix B.

6.3.1 Fuel

The base fuel and tracer should not contain any species which fluoresce in the wavelength range of interest upon illumination at 248 nm. Therefore, HPLC grade toluene and n-heptane base fuel were used.

Fig. 6.8 shows an example of fluorescence images after the injection of a pure n-heptane spray in the HPC into residual pre-combustion gas at about 600 K, recorded with the opposite-side camera configuration. In the 280 nm range the spray is barely visible. However, in the 320 nm wavelength band, the spray increases the signal with about 150 counts above the residual gas intensity, presumably due to fluorescent impurities in the fuel. The residual gas itself, without fuel injection, does not show any detectable fluorescence in both wavelength bands. Previous research also mentions background signal from impurities, but neglected it because the signal levels were below 10% of the toluene signal [3]. However, the increased background level is not constant over the field of view and needs to be taken into account when evaluating the uncertainty of the results.

6.3.2 Tracer

Even in the absence of oxygen, the tracer lifetime may be limited due to thermal decomposition. In the optical engine, the tracer is injected into the inlet gas, way

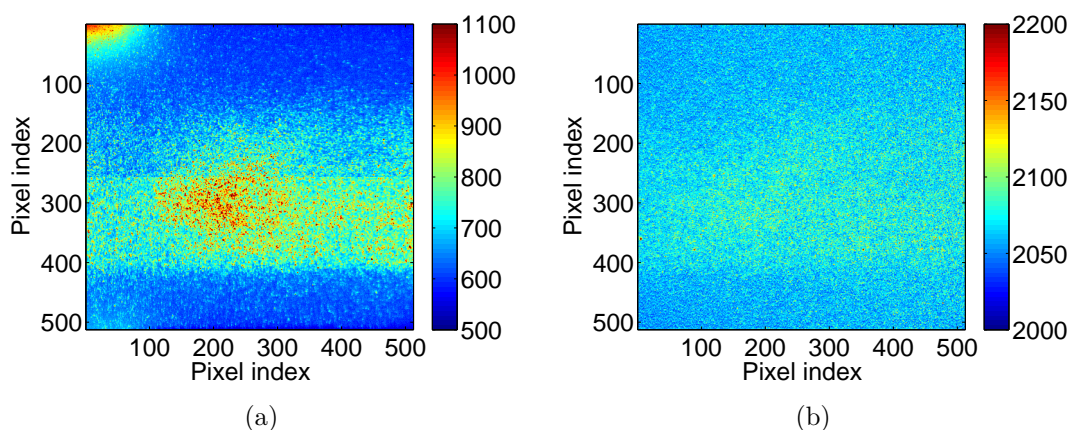


Figure 6.8: Raw images of pure n-heptane injection(320 nm (a) and 280 nm (b)) in the HPC into residual pre-combustion gas at about 600 K. The fuel is injected from the top right corner. The increased signal in the center of the 320 nm image originates from fluorescent minor impurities in the fuel. The top left corner of the 320nm signal shows increased signal due to a minor light leak.

before fuel injection. In the HPC, this is not possible, since the toluene would not survive precombustion; therefore, toluene is mixed into the fuel that is injected into the HPC. The residence time (before laser excitation) at high temperature is in both cases much less than about 0.1 s, so that thermal decomposition is not expected to be significant [12]. At high tracer density, the excitation laser beam will be absorbed on its way through the combustion chamber. This should not affect the fluorescence ratios (more on this below), but does of course limit the signal strength away from the entrance window of the laser beam. The toluene concentration must be adjusted to an acceptable compromise between signal level and signal uniformity.

Fluorescence trapping might play a role in our experiments, because of the redshift of the toluene fluorescence relative to its absorption spectrum [2]. The absorption spectra of toluene [12] extend to 290 nm at temperatures around 700 K; therefore different toluene concentrations from those used during calibration might influence the amount of fluorescence trapping.

6.3.3 Laser

The laser energy may vary from shot to shot, but the normalized fluorescence spectrum, however, need not change with laser power.

The magnitude of the laser fluence [mJ/cm^2] does affect the fluorescence yield. At low fluence the fluorescence yield rises linearly with laser pulse energy, but at higher fluence saturation sets in and the fluorescence yield levels off. Eventually, under conditions of full saturation, the fluorescence yield is independent of laser pulse energy. Although it is generally advised to stay away from saturation [3], it is not immediately obvious why the LIF ratio method would not work any more when the fluorescence yield is saturated.

To delimit the linear regime, we recorded the band-pass-filtered LIF signals of toluene vapor at a fixed CAD and inlet temperature in the motored optical engine, and calculate the ratio of the signals on the two cameras. The laser fluence, relative

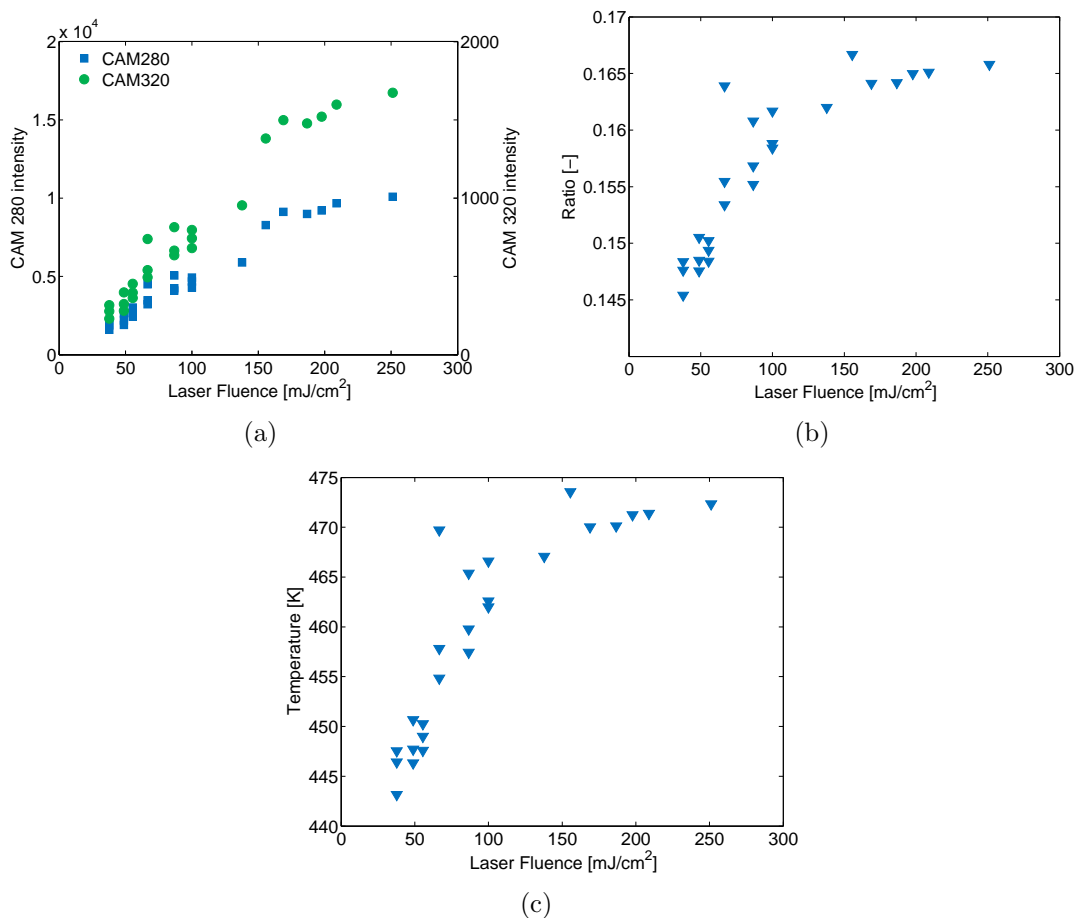


Figure 6.9: LIF intensities and ratios as a function of (single shot) laser fluence obtained in the optically accessible engine at 300 CAD, with an inlet air temperature of 50 °C. The 320/280 ratios represent a temperature span of approximately 460 ± 15 K.

to the beam waist of 1.5 mm and assuming negligible absorption, was varied from approximately 50 to 250 mJ/cm² with constant toluene concentration and camera gain. The measured average pixel values are shown in Fig. 6.9(a) as function of laser fluence. When looking at the calculated 320/280 ratio (figure 6.9(b)), it can be concluded that increasing the laser fluence above 150 mJ/cm² does not influence the ratio. Remarkably, the ratio does change for a laser fluence below 150 mJ/cm². This is explained by the low overall signal levels on the 320 nm camera. Other researchers mention a laser fluence of about 50 mJ/cm² as the upper limit for linear fluorescence response [3], which contradicts with our findings. Currently, the results published on the assumed ratio change as function of fluorescence saturation are inconclusive. Therefore all experiments presented below are conducted with moderate laser power levels around 150 mJ/cm² just before entering the engine.

6.3.4 Camera

The quantum efficiency of the intensifier photocathode is dependent on the incoming wavelength. In the wavelength region around 300 nm the quantum efficiency of the

unigen II coating of our camera systems (originally purchased for experiments around 200 nm) is in the order of only 10%. When the intensity signal on the camera drops, the accuracy decreases due to a lower signal-to-noise ratio. Therefore a 2×2 pixel binning approach is used, resulting in a decreased spatial resolution of 512×512 pixels. ICCD cameras only respond linearly to the incoming amount of photons over a certain intensity range. Also multi-channel-plate (MCP) saturation needs to be avoided [13]. Due to the low photocathode quantum efficiency for the wavelength range under investigation, the MCPs do not saturate in the performed experiments. To check the linearity range, the camera intensity as function of the incoming light from a white diffusive screen is measured and the light intensity is adjusted by means of the camera lens diaphragm. The observed maximum intensity of the linear range is different for all cameras used and is 1.2×10^4 counts for camera 1, 2.5×10^4 counts for camera 2 and 6.0×10^4 counts for camera 3 (on a full dynamic scale of 6.5×10^4). It should be mentioned that this test was performed with a white light source and the MCP might now saturate earlier than for the UV wavelengths.

6.3.5 Dichroic filters and the finite solid angle of light collection

The characteristics of multi-layer coated beam splitters and narrow bandpass filters depend on the angle of incidence of the incident light. In a first order approximation, the variation of cut-off wavelength with angle of incidence θ_i can be described by

$$\lambda(\theta_i) = \lambda_0 \sqrt{1 - \sin^2 \theta_i / n_{\text{eff}}^2},$$

in which the effective refractive index n_{eff} depends on the filter, and λ_0 is the filter design wavelength at normal incidence. The shift is always to the blue, and can amount to a few percent of the design wavelength for moderate angles of incidence. (Specific data can be found on manufacturers web sites; see e.g. [?]) In light-starved applications like ours, the desire to harvest as much light as possible naturally leads to the use of fast collection optics close to the source. This, however, implies both an angle of incidence variation over the field of view and over the solid angle that contributes to single pixels. The situation for the 45° beam splitter is schematically illustrated in Fig. 6.10.

For the HPC measurements, the distance between the HPC and cameras is reduced as much as possible, and this was found to cause a gradient in the temperature calibration over the field of view (same-side setup only). We discuss our approach to correct for that in section 6.5.2 of this paper.

6.3.6 Collisional quenching

Previous research shows a large influence of molecular oxygen on the fluorescent signal by collisional quenching, the efficiency of which changes as function of temperature [5, 14]. To achieve the highest possible signal and to avoid oxidation of the fuel, all experiments have been conducted without oxygen.

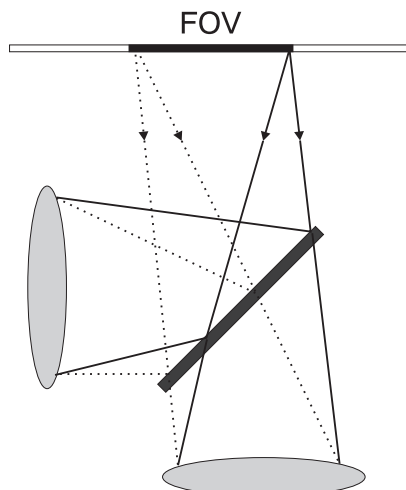


Figure 6.10: Schematic representation of the angle of incidence variation over the FOV.

6.3.7 Background subtraction

In all experiments the recorded fluorescent images also contain background consisting of several contributions. Part of the background concerns hardware offset (fixed) and dark current (depends on settings). However, the background in the HPC also contains fluorescence from pre-combustion residual gas, and during spray injection also fluorescence of the fuel, as shown in Fig. 6.8. To correct for the background fluorescence level of pre-combustion residual gas, the image recorded 0.2 seconds (5 Hz recording speed) prior to the spray image is used as background and subtracted pixel by pixel from the spray measurement. The influence of the decreasing temperature between the background recording and the spray, which is on the order of 10K, is neglected. The shot-to-shot fluctuations of laser power introduce fluctuations in the background signal, however the additional error is less than 1% of the total signal. The background signal from the base fuel is difficult to remove because the temperature response of the fluorescence signal is unknown. This signal increases the intensity of the 320 nm image with 2%–7%, depending on the operating conditions, **in both the engine and HPC measurements.**

6.3.8 Spatial alignment

Spatial alignment is performed by recording a grid image with both cameras. By using a linear conformal transformation, distortions due to translation, rotation and scaling are accounted for. After transformation, the grid lines in both images match each other with an precision corresponding to the 2 pixel thickness of the grid lines.

6.3.9 Flat-fielding

The response of an ICCD-camera-based detection system cannot be expected to be uniform over the CCD chip. Contributions to the non-uniformity may arise from individual pixel sensitivity variations, non-uniform amplification in the image intensifier, local variations in the photocathode quantum efficiency, vignetting by collection

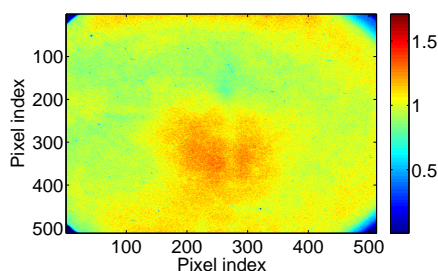


Figure 6.11: Image of a uniformly lit plane recorded with defocused camera lens; camera 1 with Halle lens. Pixel values in arbitrary units

optics and spatial variations in the spectral characteristics of the filters used (see Section 4.4 above). Insofar as the response is linear, the net non-uniformity can be corrected for by means of a so-called flat-field image: an image recorded by the detection system from a uniformly lit object plane. Non-uniformities in the flat-field image are the net result of non-uniformities in the detection chain: essentially, the pixel values in the flat-field image (after background subtraction) can be treated as individual scale factors. The flat-fielding method corrects for sensitivity variations across the photocathode, phosphor screen and CCD chip. When the flat-field image is determined with a lens mounted on the camera, lens aberrations and vignetting are also accounted for [13, 15]. Accurate flat-fields for both cameras are the key to achieve accurate image ratios and minimize the systematic error.

Flat-field images were recorded with defocused camera lenses from a diffusely reflecting screen illuminated by a white-light source. In order to account for possible wavelength dependence in the flat-field images, a UV light source in the spectral range of the toluene fluorescence would have been preferred. Fig. 6.11 displays the flat-field image of camera 1; it shows a difference in sensitivity between pixels of approximately a factor of two over the whole field of view. The vignetting effect in the corners is also clearly seen, although in this case that is largely due to a mismatch between the square CCD array and the circular image intensifier, and cannot be corrected for. In the opposite camera configuration, the co-flat-fielding method without bandpass filters is used, as previously used by Tea et al. [3], to quantify the relative sensitivity difference between the two cameras. By using fluorescence induced by illuminating the HPC filled with toluene vapor and N_2 by a thin light sheet, the camera sensitivities are compared for the UV wavelength bands used for the actual measurement. Again, relative pixel-to-pixel sensitivity variations in the region of interest vary by approximately a factor of 2.

Note that the co-flat-fielding technique has the potential disadvantage of unequal optical paths to the two cameras involved. This will not be an issue in the flat-fielding itself, for which the HPC contains only N_2 and toluene vapor, but may become a concern during measurements on a potentially dense spray.

6.3.10 Evaluation of spatial alignment and flat field correction

The purpose of spatial alignment and flat field correction is to force the two cameras to show the same response to the same fluorescent signal, so as not to introduce errors in the fluorescence ratio calculation.

Fig. 6.12 shows a number of image intensity correlation graphs. The location of each data point in the graphs is determined by the corresponding pixel values on two cameras, in the same-side configuration (left column) and in the opposite-side one (right column). Both cameras looked at the same scene: HPC filled with toluene vapor and N_2 . For the same-side configuration, a 30/70 broad-band beam splitter was used, in order to really have both cameras looking at the same source. Fig. 6.12(a) and 6.12(b) show the raw data, in which the cameras have been aligned mechanically only, but the signals have not been processed other than by background subtraction and 12×12 nearest-neighbor averaging. Obviously, both cameras respond differently, and the cloud of data points is broad and far removed from the ‘ideal line’ of equal pixel intensities. Improved alignment in software produces the middle row of Fig. 6.12, but this does not show much of an improvement. Flat-fielding, in this case using co-flat-fielding based on the average of ten separate images recorded by both cameras, brings a major improvement, as shown in the lower row of Fig. 6.12. The residual standard deviation of the pixel value ratios amounts to 2% for the same-side and to 3% for the opposite-side configuration.

6.4 Calibration

Calibrating the LIF ratio vs. temperature is a tedious but crucial task. The most direct calibration procedure, at least in principle, would be to determine this ratio for toluene at a known range of temperatures, using exactly the same setup as would be used in the actual experiments. To avoid the need to perform such a calibration each time the optical setup is changed, or for cases in which the ideal calibration procedure is not practically feasible, we here use an alternative approach. This approach is based on the notion that the *emitted* spectrum is characteristic for toluene (independent of the environment), but that the *measured* spectrum will be different because of all optics in between the emission and the detector. If we start out with accurate *emitted* spectra over a range of temperatures, and know the optical characteristics of all elements in the detection path, then the spectrum that would be measured at any temperature in a particular setup can be reconstructed, and the LIF ratio calculated. This procedure will be detailed below. We use temperature-dependent spectra recorded at IFPEN as a basis [1], and in the end compare temperatures derived from LIF ratios with global temperatures in our optical engine.

6.4.1 Optical path corrections

The correction for the optical path consists of two steps: (1) the IFPEN base data were transformed into emission spectra by correcting for the wavelength-dependence in the IFPEN spectrometer by Tea et al. [3]; (2) the resulting emission spectra are transformed into spectra that we would measure in our setups. From these spectra

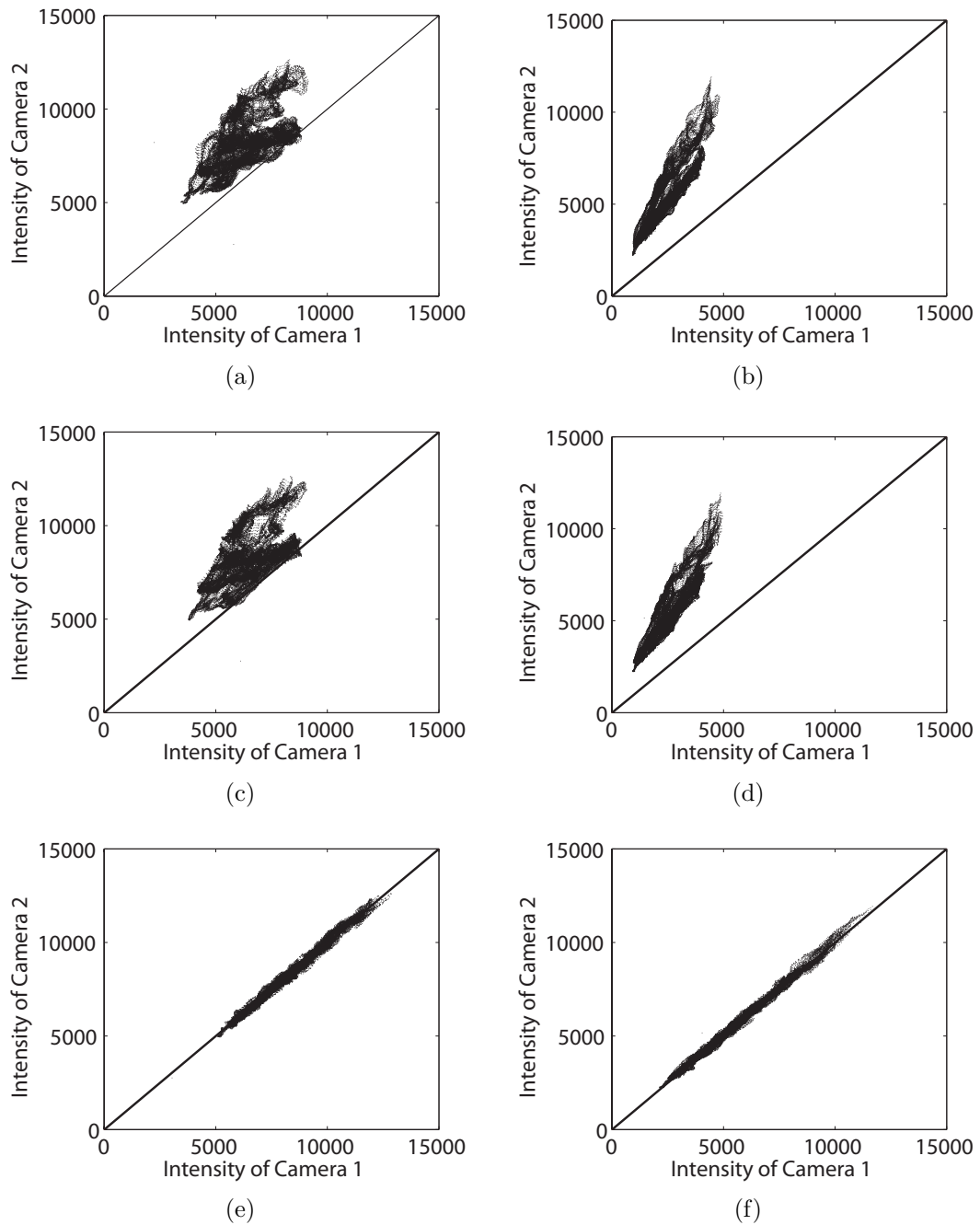


Figure 6.12: Signal intensity correlation for an image pair obtained in one-side (left column) and opposite configuration (right column). The signal is obtained from a mixture of toluene vapor and nitrogen. (a&b) Original; (c&d) After spatial alignment; (e&f) After co-flat-fielding correction. The one-side images are obtained by using a 30-70% beam splitter. The used images are 12×12 px neighbor average filtered.

and the filter characteristics the LIF ratios for our setups are calculated as a function of temperature. The optical path corrections of step (2) include the wavelength-dependent transmission/reflection coefficients of camera lenses, the sapphire piston window, mirrors (incl. the dichroic beam splitter in the case of the same-side setup), and the photocathode of the ICCD cameras used; these were given in Fig. 6.4. As an example, the emission spectra reconstructed from the IFPEN data for various temperatures (red) are shown in Fig. 6.13, together with the spectra arriving at our ICCD cameras after reflection or transmission by the dichroic mirror (setup of Fig. 6.7a). Obviously, the transition region in the transmission/reflection characteristics of the dichroic mirror significantly reduces spectral intensity in the 300 nm region.

For this calibration approach, different overall camera sensitivities (“overall” meaning apart from flat field corrections that have been discussed above) have to be taken into account explicitly. We determine the relative sensitivity in a straightforward way, by recording images from the same object under constant illumination. This factor varies with gate time, camera gain and recording speed, and should be determined separately for each measurement condition.

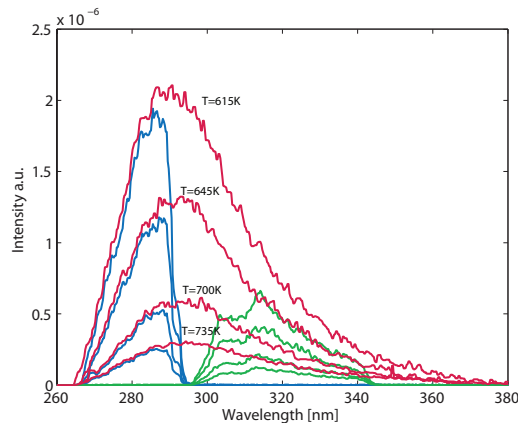


Figure 6.13: Measured toluene spectra (red) from IFPEN for different temperatures adjusted with the transmission and reflection efficiencies from Fig. 6.4. The resulting 280 nm part of the spectrum is blue and the 320 nm part is green. The red curves have been scaled with a factor 20 for visualization purposes.

6.4.2 Engine model

A multi-zone engine model, which incorporates a Woschni correlation to estimate the heat loss to the cylinder walls [16], is used to calculate the bulk in-cylinder temperature from the pressure trace. Our model does not account for blow-by losses via the piston rings, and the bulk in-cylinder temperature at the moment of intake valve closing (IVC in Table 6.1) is treated as a variable, ranging between 30 – 70°C. Fig. 6.14 shows the LIF ratio vs. temperature plots derived in this way for various IVC temperatures, and compares them to the similar data derived from the original IFPEN curves, corrected for the differences in the optical setup used in both experiments, as described in the previous section. Clearly, the curves are very similar, but the IFPEN data cross several of our curves for different IVC temperatures. This may be due to differences

in heat loss approximations and blow-by. The IFPEN temperatures are also derived from the in-cylinder pressure trace and also include an unknown inaccuracy.

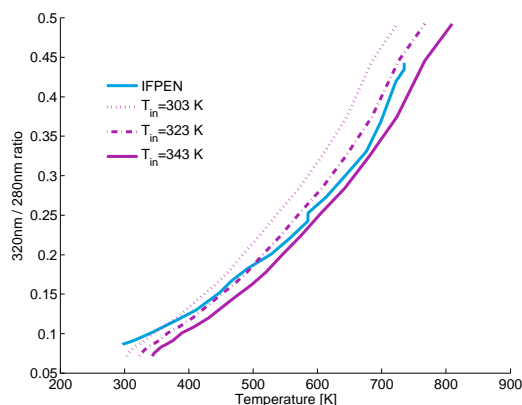


Figure 6.14: Temperature calibration lines from the optical engine in Eindhoven and at IFPEN. The red curves are based on the same LIF data but with three different assumptions for the IVC temperature.

6.4.3 Uncertainty analysis

We estimate the precision, or random error, in the final result starting from the flat-field-corrected images discussed in the context of Fig. 6.11. The standard deviation of pixel values around the ‘ideal line’ amounts to 2% and 3% for the same-side and opposite-side configurations, respectively. Thus, the standard deviation in the LIF ratio amounts to about 4%. Depending on the actual value of the ratio (see Fig. 6.14), this translates into a temperature precision of 7-12 K for ratios between 0.1 and 0.4. The accuracy, defined here as the uncertainty due to systematic errors in the procedure, originates from several sources: undesired fluorescence from the base fuel, residual non-uniformities in the flat-field matrices, and systematic errors in the calibration procedure. Unfortunately, even the HPLC-grade n-heptane base fuel itself produces some LIF upon 248 nm illumination, and notably in the 320 nm band (see Fig. 6.8). Here, the base fuel may contribute from 2-7% of the total signal, depending on the operating point.

The flat field correction at opposite configuration use the toluene LIF signal to obtain the co-flat-fielding matrix. The camera response accounted for in the flat-field matrix is from almost the same wavelength range as in the actual spray measurements.

However, for the one-side configuration, the flat-field approach using the toluene LIF signal itself cannot be used because of the dichroic beam splitter. Therefore, flat-field images are obtained using a white light source.

6.5 Results

The results section is split into two major parts. Part one presents the results in the optically accessible engine, the second part presents the result in the high-pressure cell.

6.5.1 Optically accessible engine results

Residual fuel fluorescence

A basic assumption of the LIF ratio method is that the fluorescence transmitted by the band-pass filters is really due only to the tracer. Thus, it is imperative that the fuel itself does not fluoresce upon 248 nm irradiation. Before each measurement series, we check for fluorescence signal during fuel injection without adding toluene to the system. Initial experiments were performed with spectrometric-grade n-heptane (99.3% pure). This always resulted in clearly recognizable spray images (Fig. 6.15), obviously due to fluorescence of trace components in the fuel. The whole fuel line was then flushed with HPLC-grade n-heptane (99.6% stated purity; Sigma-Aldrich). Fig. 6.16 shows the time evolution of the average signal in one of the spray tips (location indicated in Fig. 6.15) measured on both cameras, as a function of the amount of fuel flushed through the fuel line (including fuel pump, tubing and injector). After an initial fast decrease, the signal gradually decreases further, but not to zero, especially on the 320 nm camera. After having the system stay idle overnight, the fluorescence was again increased (data points to the right of the vertical dashed line), apparently due to residuals in crevices in the fueling system that leaked back into the fresh fuel.

This residual fluorescence gives rise to LIF ratios that deviate strongly from those expected for toluene fluorescence at the same temperature. Therefore, during actual toluene LIF measurements the signal must be sufficiently high for the residual contribution to be negligible.

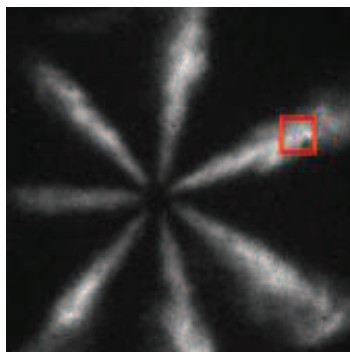


Figure 6.15: Single shot LIF image of a heptane spray in the optical engine. The red square represents the selected area of the spray to determine the intensity decrease as function of the amount of flushed high purity heptane.

Temperature During fuel injection

Temperature stratification during fuel injection was investigated by adding toluene to the inlet manifold. Together with air, the toluene will be entrained by the injected fuel spray, which should allow visualization of the temperature field in and around the sprays. A representative result of the measurements, and a translation of the LIF ratios to a temperature field on the basis of Fig. 6.14, is shown in Fig. 6.17 (non-reactive conditions). The recorded images are smoothed by 12×12 neighbor averaging, thus

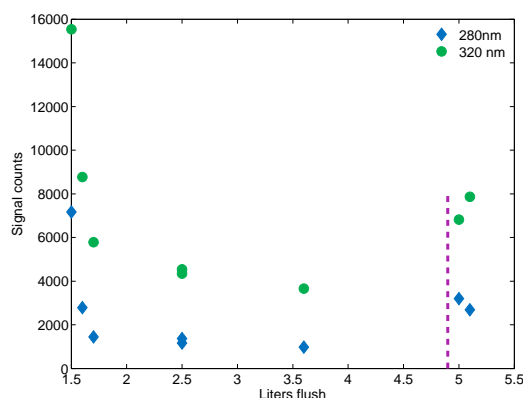


Figure 6.16: Intensity as function of pure n-heptane flush. The fueling system was filled with 99.3% pure n-heptane prior to flushing with 99.6% pure n-heptane. Images are recorded at -20 CAD ATDC, (laser power 60 mJ, camera gain=100). The vertical line displays different measurement days. The counts are not accumulated.

achieving a lateral resolution comparable to the thickness of the excitation laser light sheet. Pixel values below 300 counts (after background subtraction) are discarded. The temperature field, although qualitatively correct, shows a number of artifacts. Some of these are due to the mechanical construction of the combustion chamber (the valve seats are clearly visible), some others likely relate to multiple scattering or fluorescence trapping by the sprays. The global temperature field is uniform, but shows a LIF ratio-based temperature that is approximately 250 K above the global temperature derived from the pressure trace. The high ratios at the valve edge and in between the sprays suggest trapping of fluorescent signal which is more pronounced in the 280 nm region than in the 320 nm region. The cold fuel spray regions are clearly recognizable.

6.5.2 High pressure cell results

To investigate the spray temperature field in more detail than is possible in an engine environment, experiments have been conducted in a high-pressure cell. The purpose of the research is to investigate the major characteristics of the temperature distribution while spray propagates into hot ambient gas. The experimental conditions are listed in table 6.5.

Table 6.5: Experimental conditions

Injection pressure	900 bar
Injection duration	2 ms
Ambient temperautre	590 K
Ambient density	20 kg/m ³

We present two separate data sets. The first one is obtained by a same-side camera configuration and the second by an opposite side arrangement. The laser sheet thickness converges from 1.8 mm to 0.8 mm from left to right in the HPC, and therefore

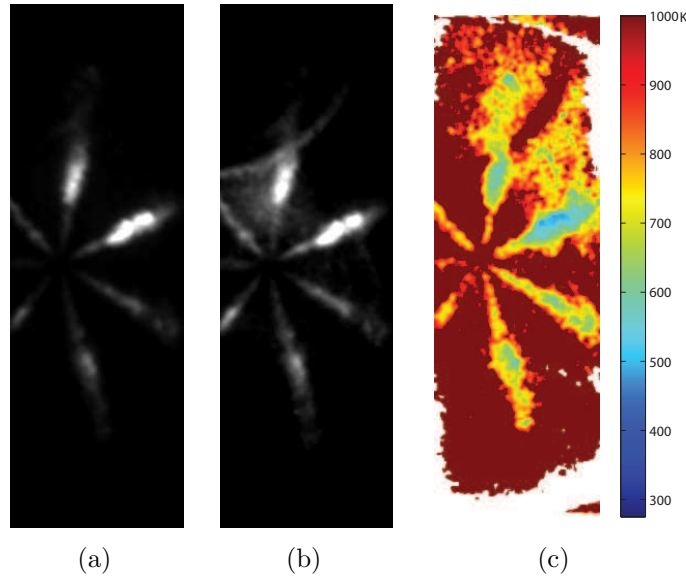


Figure 6.17: Fuel injection in a mixture of nitrogen and toluene vapor, recorded at 20 CAD before TDC. Injection started 25 CAD before TDC. The toluene vapor entrains fuel sprays in the fuel/gas mixing process.

the spatial resolution at the laser entrance side will be lower than at the far end. The spray enters the cell diagonally at the far end.

Temperature distribution in the spray region

Same-side camera configuration results The results presented in this section are for the same-side camera configuration. The obtained spatial scaling factor is 9.28 px/mm. The images are smoothed by 12×12 neighbor averaging, to represent the same spatial resolution as the average laser thickness in the middle of the HPC (1.3 mm). The fuel doped with 10 vol.% toluene is injected into ambient conditions of $T_{amb}=590$ K, for a duration of 2 ms. Per injection one image is acquired, the delay time is advanced in steps of 0.5 ms to investigate the time evaluation. As a result, each pair of images originates from separate injections.

As mentioned above, the dichroic beam splitter is suspected to affect the temperature calibration of the LIF ratio, because its optical characteristics vary with angle of incidence of the incoming light. Evidence for this is presented in Fig. 6.18. Panel (a) shows the fluorescence intensity (integrated over part of the laser light sheet width) as a function of laser penetration depth into the HPC. (Zero corresponds to where the laser beam enters the field of view.) This measurement was made about 2 seconds after fuel/toluene injection into the HPC, after which time the mixing fan is expected to have homogenized the cell contents. Obviously, the signals drop with increasing penetration depth. In itself, this could simply be due to absorption of the laser beam. Fig. 6.18(d), however, shows that also the LIF ratio drops with increasing penetration depth, in spite of the presumably uniform temperature. This effect is found to be independent on incident laser power and of toluene concentration; we attribute it to the beam splitter. Note that according to the curves of Fig. 6.4 it is indeed the "red" part of the spectrum that is most sensitive to the exact switching wavelength of the

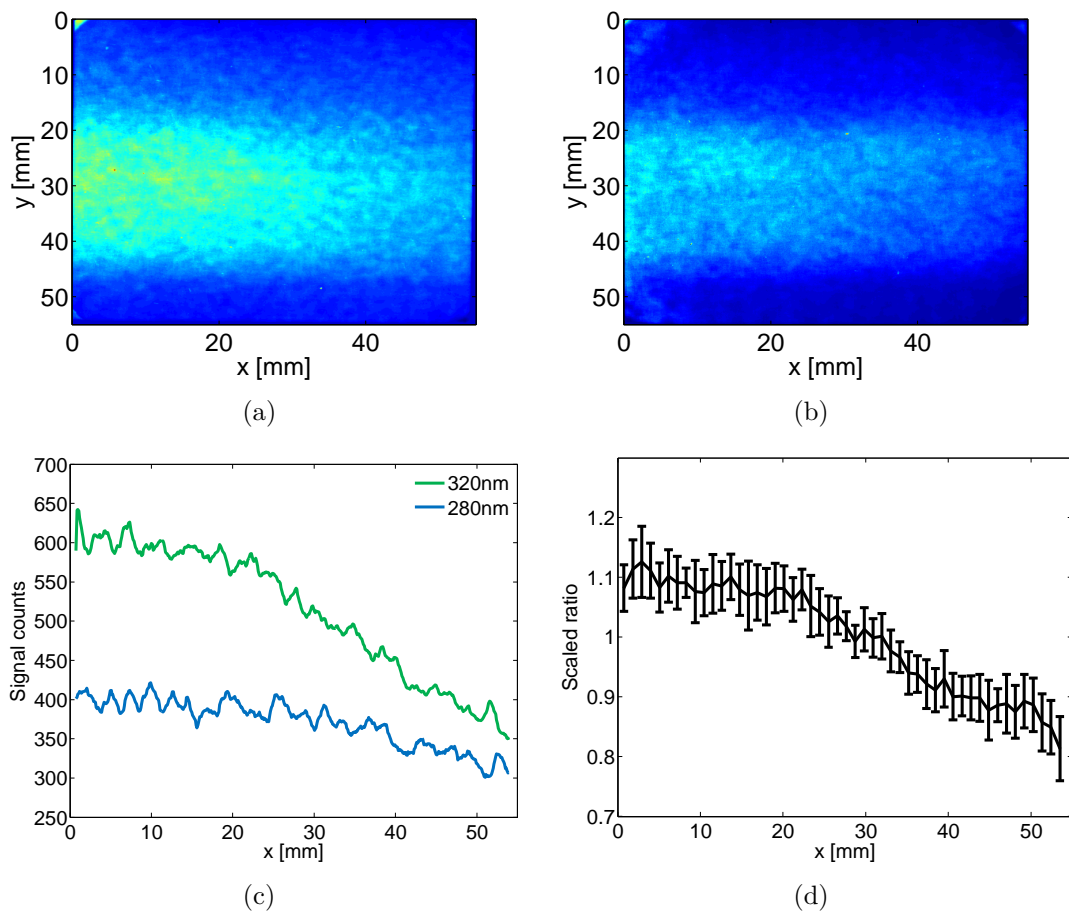


Figure 6.18: The correction of dichroic beam splitter effect. The laser sheet propagate from left hand side to right hand side. (a) Toluene vapor image of camera 1. (b) Toluene vapor image of camera 2. (c) 280 nm and 320 nm part of the fluorescence signal after spray injection as function of the distance from the left side of the field of view. (d) mean value and standard deviation of 13 vertically averaged scaled ratio curves. The ratio is scaled using the average ratio in x-direction.

beam splitter.

By using Fig. 6.18(d) as a correction curve, the temperature distributions of the sprays are calculated, as shown in Fig. 6.19. The fuel is injected out of the top right corner and the laser beam propagates from left to right. The rectangle in Fig. 6.19 indicates the extent of the laser light sheet. It does not directly illuminate the liquid part of the spray; for our conditions the liquid length of the spray is estimated to be 27 mm using a mixing-limited spray vaporization model [17]. Other areas may be excited indirectly by laser scattering via the walls all by multiple scattering.

Increased background levels due to undesired fluorescence contribute to the systematic errors of the LIF ratio which result in a temperature which is approximately 19% above the ambient temperature. To account for these systematic errors the edge of the spray is assumed to have the same temperature as the ambient gas and the other temperatures are given as a temperature difference with respect to the boundary temperature.

When observing the experimental spray development in a two-dimensional cross-

section one can conclude that the temperature field coincides with the simplified and generally accepted view of a diverging spray due to air entrainment, which should result in heating of the fuel from the core region outwards and in downstream direction. However, at the 1.58 and 2.08 ms point, large gaps in the spray pattern might indicate increased air entrainment and therefore increased temperatures in these regions compared to other nearby regions. The experimental results are compared with LES to verify the findings.

6.5.3 Numerical setup

The LES code used in this study is the fully compressible AVBP solver co-developed by IFP Energies Nouvelles and CERFACS for structured and unstructured meshes [18]. The second order centred Lax-Wendroff convective scheme [19] is combined with an explicit time advancement. Unresolved subgrid-scale turbulence is modeled by a Smagorinsky model [20] with constant coefficient. The dispersed liquid phase is resolved using a mesoscopic Eulerian formalism [21]. The region close to the injector, dominated by high volumetric ratios of liquid fuel and breakup effects, is not included in the simulations. The DIturBC injector model [22] is used to bridge that region by imposing physical flow conditions at a distance approximately 10 nozzle diameters downstream of the injector outflow plane. Its principle is to impose boundary conditions for the two phase flow at a distance downstream of the injector nozzle, in regions where the flow has been dispersed by breakup phenomena and can be addressed by a diluted mesoscopic Eulerian formalism.

The LES has been run on a computational mesh which represents a closed combustion vessel with slightly larger dimensions than the HPC (112^3 versus 108^3 mm³). It consists of a tetrahedral mesh with local refinement. The mesh size near the nozzle exit is 80 μ m and gradually increases to 800 μ m towards the other end of the domain, yielding approximately 0.7 million nodes and 4.3 million cells. All boundaries, except for the injection plane, are taken as adiabatic walls which have negligible influence on the spray internal structure. This mesh has been chosen on the basis of spray formation results presented in [23].

Opposite camera configuration results

The opposite-side camera setup obviously is not plagued by beam splitter artifacts. We have determined independent calibration points for the LIF signal ratio by evaporating toluene into the heated HPC. These results will be compared to the IFPEN-based calibration curve here.

The temperature calibration line in Fig. 6.20 is obtained by using the same approach as in section 6.4. It differs from the one presented in figure 6.14 because of the lack of the dichroic beam splitter. The image also presents two data points obtained from toluene vapor at two different ambient temperatures. As expected the ratio calibration points match well with the IFPEN data and once again prove the validity of the calibration approach presented in section 6.4.

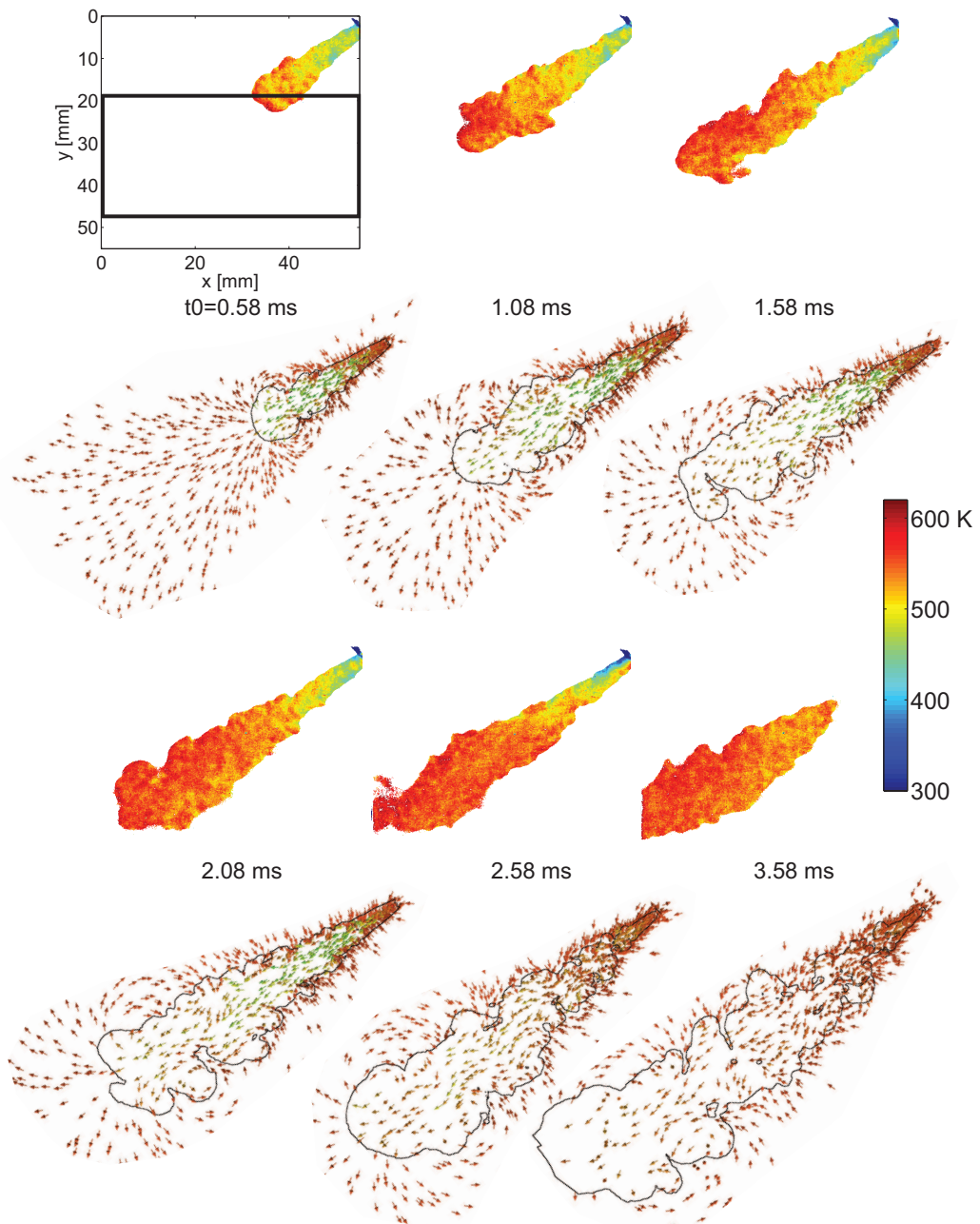


Figure 6.19: Comparison between temperature distribution in the HPC and velocity fields obtained with LES. The black rectangle in the top left image represents the laser sheet area. Toluene outside this rectangle is excited by multiple scattering. The velocity vectors are colored according to temperature. The limited field of view of the experimental setup prohibits visualization of the complete spray at 2.58 and 3.58 ms.

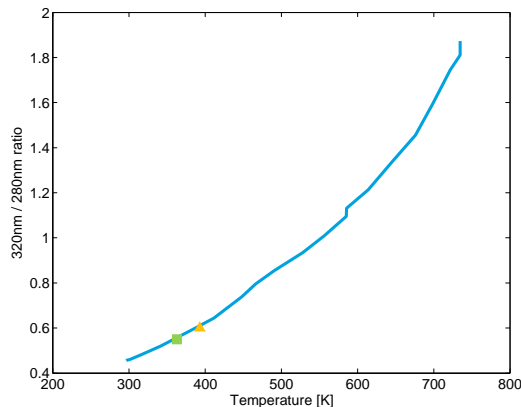


Figure 6.20: Temperature calibration line for the opposite camera configuration. The square and triangle represent two measurement points from toluene vapor ratios at known ambient temperature.

6.6 Conclusions and recommendations

In principle, Planar Toluene LIF is capable of visualizing temperature distributions with high precision, instantaneously, and with a good spatial resolution.

The working principle being based on the intensity ratio between fluorescence in two disjunct wavelength bands, the toluene LIF method is, however, susceptible to a number of potential pitfalls, several of which have been discussed in this paper. These are of two kinds. On the one hand, the signal intensity drops quickly with rising temperature, giving rise to increased uncertainty. From this point of view, it may be worthwhile to study the possible effect that saturation may have on the fluorescence spectrum; should this be negligible, than the method would be safe to use in the saturated regime, which is beneficial for the signal level.

On the other hand, there is the issue of fluorescence wavelength selection. Modern coating techniques can produce bandpass filters that combine a narrow transmission wavelength band with steep edges and high ($\sim 90\%$) transmission efficiency, but these spectral properties depend on the angle of light incidence. The desire to collect as much light as possible, and thus using fast collection optics, then introduces variations in the spectral collection efficiency over the field of view. This translates into a spatial dependence of the calibration factor. We have found such effects for the dielectrically coated optics used in our "same-side" configuration (Fig. 6.7a). Similar issues, at least with the same net effect of location-dependent deviation in the spectral collection efficiency, may arise if measurements are performed close to reflecting surfaces.

We have discussed several ways to obtain calibration data, based on either accurate spectra measured at IFPEN, or LIF signal ratios in our own setups at known, independently measured temperatures. All methods show good agreement. Temperature field measurements in and around fuel sprays have been evaluated, and show a precision of about 4%. Comparison with LES is satisfactory, both showing similar hot regions and gradients. The accuracy of the experimental temperature fields, however, is negatively affected by residual fluorescence of the base fuel (HPLC-grade n-heptane). As in all measurements through spectral band pass filters, the actual spectral information in

the signal is lost, and one must resort to a somewhat religious belief that all light transmitted by the filter really originated from the molecules of interest. To avoid that assumption, a spectrograph can be used, but this obviously goes at the expense of at least one spatial dimension.

Bibliography

- [1] R. Devillers, G. Bruneaux, and C. Schulz. Investigation of toluene LIF at high pressure and high temperature in an optical engine. *Applied Physics B: Lasers and Optics*, 96:735–739, 2009. ISSN 0946-2171.
- [2] C. Schulz and V. Sick. Tracer-LIF diagnostics: quantitative measurement of fuel concentration, temperature and fuel/air ratio in practical combustion systems. *Progress in Energy and Combustion Science*, 31(1):75 – 121, 2005. ISSN 0360-1285.
- [3] G. Tea, G. Bruneaux, J.T. Kashdan, and C. Schulz. Unburned gas temperature measurements in a surrogate diesel jet via two-color toluene-LIF imaging. *Proceedings of the Combustion Institute*, 33(1):783 – 790, 2011. ISSN 1540-7489.
- [4] K. Mohri, M. Luong, G. Vanhove, T. Dreier, and C. Schulz. Imaging of the oxygen distribution in an isothermal turbulent free jet using two-color toluene LIF imaging. *Applied Physics B: Lasers and Optics*, 103:707–715, 2011. ISSN 0946-2171.
- [5] W. Koban, J.D. Koch, R.K. Hanson, and C. Schulz. Toluene LIF at elevated temperatures: implications for fuel/air ratio measurements. *Applied Physics B: Lasers and Optics*, 80:147–150, 2005. ISSN 0946-2171.
- [6] F.P. Zimmermann, W. Koban, C.M. Roth, D. Herten, and C. Schulz. Fluorescence lifetime of gas-phase toluene at elevated temperatures. *Chemical Physics Letters*, 426(4-6):248 – 251, 2006. ISSN 0009-2614.
- [7] M. Luong, R. Zhang, C. Schulz, and V. Sick. Toluene laser-induced fluorescence for in-cylinder temperature imaging in internal combustion engines. *Applied Physics B: Lasers and Optics*, 91:669–675, 2008. ISSN 0946-2171.
- [8] J. Mannekutla, A. van Vliet, R.K., N.J. Dam, and H. ter Meulen. The temperature field just before combustion in a diesel engine. *European Combustion meeting*, 2011.
- [9] E. Doosje. *Limits of mixture dilution in gas engines*. PhD thesis, Eindhoven University of Technology, 2010.
- [10] R.S.G. Baert, P.J.M. Frijters, L.M.T. Somers, C.C.M. Luijten, and W. de Boer. Design and operation of a high pressure, high temperature cell for HD diesel spray diagnostics: Guidelines and results. *SAE Technical Paper*, 2009-01-0649, 2009.

-
- [11] S. Krüger and G. Grünefeld. Stereoscopic flow-tagging velocimetry. *Applied Physics B: Lasers and Optics*, 69:509–512, 1999. ISSN 0946-2171.
- [12] W. Koban, J.D. Koch, R.K. Hanson, and C. Schulz. Absorption and fluorescence of toluene vapor at elevated temperatures. *Phys. Chem. Chem. Phys.*, 6:2940–2945, 2004.
- [13] J. Lindén, C. Knappe, M. Richter, and M. Aldén. Limitations of ICCD detectors and optimized 2D phosphor thermometry. *Measurement Science and Technology*, 23(3):035201, 2012.
- [14] W. Koban, J. D. Koch, R. K. Hanson, and C. Schulz. Oxygen quenching of toluene fluorescence at elevated temperatures. *Applied Physics B: Lasers and Optics*, 80:777–784, 2005. ISSN 0946-2171.
- [15] T.C. Williams and C.R. Shaddix. Simultaneous correction of flat field and non-linearity response of intensified charge-coupled devices. *Review of Scientific Instruments*, 78(12):123702, 2007.
- [16] U. Egüz, L.M.T. Somers, C.A.J. Leermakers, and L.P.H. De Goey. Multi-zone modelling of PCCI combustion. *International Journal of Vehicle Design*, 55(1):76–90, 2011.
- [17] J.V. Pastor, J.J. López, J.M. García, and J.M. Pastor. A 1D model for the description of mixing-controlled inert diesel sprays. *Fuel*, 87:2871–2885, 2008.
- [18] V. Moureau, G. Lartigue, Y. Sommerer, C. Angelberger, O. Colin, and T. Poinsot. Numerical methods for unsteady compressible multi-component reacting flows on fixed and moving grids. *Journal of Computational Physics*, 202(2):710 – 736, 2005. ISSN 0021-9991.
- [19] P. Lax and B. Wendroff. Systems of conservation laws. *Communications on Pure and Applied Mathematics*, 13:217–237, 1960.
- [20] J. Smagorinsky. General circulation experiments with the primitive equations: I. the basic experiment. *Monthly Weather Review*, 91(3):99–164, 1963.
- [21] P. Février, O. Simonin, and K.D. Squires. Partitioning of particle velocities in gas-solid turbulent flows into a continuous field and a spatially uncorrelated random distribution: theoretical formalism and numerical study. *Journal of Fluid Mechanics*, 533:1–46, 2005.
- [22] L. Martinez, A. Benkenida, and B. Cuenot. A model for the injection boundary conditions in the context of 3D simulation of diesel spray: Methodology and validation. *Fuel*, 89:219–228, 2010.
- [23] C. Bekdemir, L.M.T. Somers, L.P.H. de Goey, J. Tillou, and C. Angelberger. Predicting diesel combustion characteristics with large-eddy simulations including tabulated chemical kinetics. *Proc. Comb. Inst.*, Submitted, 2012.

Conclusions, Recommendations and Outlook

The major purpose of this work was to study the 2D temperature distribution of fuel sprays to improve the understanding of the mixing mechanism and its consequences for the combustion process in compression ignition engines. A constant volume high pressure cell (HPC) is used to simulate engine conditions. Two topics are addressed: the 2D temperature distribution of pre-combustion residual gas in the HPC and the 2D gas temperature distribution in fuel sprays. The first topic concerns the ambient conditions prior to fuel injection. In both cases, laser diagnostic techniques are investigated in detail and analytical models are used to describe the physical processes involved.

According to the specifications for 2D temperature measurement of sprays and residual gas in the HPC, four laser diagnostic methods were tested and compared to select the most optimal ones. For measuring the temperature of pre-combustion residual gas, laser-induced phosphorescence using BAM as thermalgraphic phosphor was selected, mainly because of its strong signal. For non-reacting sprays, laser-induced fluorescence using toluene as a tracer was selected for the simplicity of setup. For both diagnostic methods, the spectral ratio method is used to cancel the influence of laser profile and differences in tracer concentration. Both methods are discussed below.

7.1 2D temperature distribution in the HPC

We have presented an analytical and experimental study of the cooling process of the residual gas obtained from pre-combustion in the HPC. An analytical model was developed to study the temperature decay from the peak of pre-combustion (> 2000 K) to about 500 K. It is based on the history of bulk average temperature, as deduced from the pressure recorded during the cooling process.

The analytical model assumes that turbulent convection is dominating the cooling process. Without fan-mixing the heat transfer rate decays together with the turbulent kinetic energy. Assuming the decay rate of turbulent kinetic energy to be proportional to the 1.5th power of turbulent kinetic energy itself, the cooling model can describe

the cooling process with an accuracy of 50 K. However, from several seconds after the pre-combustion, the model tends to overpredict the temperature, probably because buoyancy is not considered in the model. Fortunately, however, these longer time scales are irrelevant for typical spray injection experiments.

If fan mixing is added, a constant turbulent flow is maintained, that is, the turbulent kinetic energy is constant during the cooling process. With this assumption, the modeling results match experimental results very well for cases with fan on.

A natural and a forced convection model are used to estimate the thermal boundary layer thickness and the core temperature in the scenarios without and with fan-mixing, respectively. In the first scenario, the core temperature is about 5 – 7% higher than the bulk temperature. In the second scenario the difference is 2 – 6%. These results are reasonable when compared with experiments. The model provides a good estimation for the ambient condition during fuel spray measurements.

To determine the 2D temperature distribution also experimentally, the feasibility of phosphor thermometry was demonstrated, using the laser-induced phosphorescence (LIP) technique on $\text{BaMgAl}_{10}\text{O}_{17}:\text{Eu}$ (BAM) as thermographic phosphor (TP). Although there are no indications that a short (seconds) exposure to high temperature (> 800 K) changes the characteristics of BAM, low signal intensity poses a limitation to the method above this temperature. The technique is capable of measuring temperature in the gas phase below 650 K with sufficient signal intensity.

The issue of weak signal at high temperature arises mainly due to two reasons: the lifetime of BAM-LIP emission decreases dramatically with increasing temperature; and the TPs settle on the bottom of the cell. The TPs need to be suspended long enough in the gas to go through the filling procedure of the HPC. A model was developed to describe the gradual, size-dependent settling of the seeded particles. The model was validated using experimental results and can be used to predict the signal intensity at the start of an experiment as function of the filling time.

The powder injector and the powder container, designed for the TP experiments, performed beyond expectation. Particle agglomeration was not observed, probably due to the high shear forces induced. Particle sticking is not a major concern as long as stainless steel tubing is used and Teflon material is avoided. The particles should be coated with SiO_2 to reduce the stickiness. Also the mixing fan of the HPC tends to blow the TPs to the wall, so it is turned off in the experiments.

The spatial resolution in the TP experiment was estimated to be 3 mm in the plane of the laser sheet and 10 mm along the line of sight. The spatial resolution is primarily determined by multiple scattering present in the experiments. A higher spatial resolution can be obtained when multiple scattering is reduced, e.g. by using a lower number density but bigger particles. The precision is better than 30 K at 400 K and 60 K at 650 K.

Temperature field results show that there is a significant temperature gradient in the vertical direction present during the cooling phase in the HPC when the mixing fan is not used. The temperature difference between top and bottom of the HPC (for example, 150 K after 4 seconds of cooling) is caused by hot gases moving to the top of the cell due to buoyancy. This finding supports the interpretation of the analytical model, which overpredicts the temperature for neglecting the buoyancy effect.

Although the potential of the method has been clearly demonstrated, the presented BAM-LIP method is currently not able to provide the 2D temperature distribution

prior to fuel injection. The major limitation is the long filling procedure of the HPC. Since the seeding device can not stand more than 5 bars, the TPs have to be seeded at the very early stage of the filling procedure. The mean intensity decreases by 80% due to the falling of the TPs. A possible improvement is to seed the TPs just before the pre-combustion with a high pressure seeder, so the volume density remains high enough to emit sufficient signal at higher temperature. More advanced techniques such as Structured Laser Illumination Planar Imaging (SLIPI) could also be applied to reduce the multiple scattering effect.

7.2 2D temperature distribution of fuel sprays

In this topic, we have presented the comparison of two phenomenological spray models in their prediction of temperature distribution in a fuel spray, and the implementation of laser-induced fluorescence (LIF) using 10% toluene as a tracer for 2D temperature measurement in n-heptane sprays.

The major difference between the Versaevel and the Valencia model exists in their assumptions for radial profiles of fuel concentration and velocity. The Versaevel model assumes a top-hat profile while the Valencia model assumes a Gaussian profile, which is observed by averaging multiple injections. Both models predict spray penetration very well, however, they differ considerably in their prediction of the temperature distribution. The Valencia model predicts lower central line temperatures than the Versaevel model, which might be because the turbulence in a fuel spray is so strong that the Gaussian profile is not observable. Detailed evaluation of these two assumptions is needed in future research.

This research displays the strengths and weaknesses of toluene planar LIF in detail. The approach to measure temperature distributions during and after fuel injection in the HPC using planar toluene LIF has been elaborately explained. The toluene LIF method is capable of measuring temperatures up to 700 K; above that the signal becomes too weak. The precision of the spray temperature measurements is 4% and the spatial resolution is 1.3 mm.

An opposite-side camera setup seems to be beneficial over a one-side setup because it avoids the dichroic beam splitter requirement, but the precision is lower because of different light paths. Unfortunately, we were not able to measure fuel sprays in opposite configuration due to camera failure. In the one-side configuration, the characteristics of the dichroic beam splitter were found to vary over the field of view due to variation in the angle of incidence of the collected light. This needs to be corrected for. However, its influence could be reduced by using a dichroic beam splitter of which the transmission slope is in between the band-pass filter transmission curves without overlapping.

Experimental results from the HPC reveal a hot zone in the fully developed spray. The spray temperature measurements are compared with Large-Eddy Simulation (LES) results, which show that the head vortex entrains hot ambient gas, thereby creating a hot zone in the spray behind the head vortex.

The toluene LIF method offers a relatively simple and precise way to measure the 2D temperature distribution in fuel sprays. However, several improvements can be done to improve the absolute accuracy.

Firstly, the spray images showed a substantial background signal level in the 320 nm wavelength band. This originates from impurities in either the HPLC-grade n-heptane base fuel, or from impurities left in the fueling system from previous experiments. We recommend to acquire the highest purity base fuel available and to only use non-lubricated fuel pumps and fuel lines which have been purged thoroughly.

Primary tests showed that the flat-field images are wavelength-dependent. The presented results show a way to avoid this problem: co-flat-fielding using the LIF intensity of a homogeneous toluene vapor prevents the need for separate flat-fields. For the one-side setup with a dichroic beam splitter, the co-flat-fielding can be performed by replacing the dichroic beam splitter by a regular beam splitter, although the characteristics of the beam splitter should be taken into account as well.

Images should be obtained preferably using identical camera types, to avoid large differences in optical properties. The intensity regimes in which the cameras respond linearly vary greatly for the cameras used here. It is highly recommended to check the linearity regimes for the wavelength region of interest and stay in between these values at all times.

The results presented here are inconclusive for the dependence of the ratio change on toluene LIF saturation levels. Additional research should confirm if any such effect exists.

Last but not least, detailed data sets of spectra recorded at accurate temperatures including the optical pathways are needed for calibration.

7.3 Outlook

In general, the toluene LIF method is capable of providing 2D temperature information in a fuel spray with 4% precision, which makes it possible to detect the temperature gradients in sprays. The other applications include the temperature in internal combustion engines and burners. This technique could be used to build a database for the new combustion concepts which prefer a stratified mixture of air and fuel. It will also help to gain more knowledge of the physical processes of a fuel spray, together with the analytical models.

The BAM-LIP method could be used in measuring temperature distribution in gas-phase environment, where combustible tracers, such as toluene, are not applicable. The seeding device developed in this work can be used in seeding solid particles in various applications such as PIV and dust combustion etc. The analytical cooling model describes the temperature decay in a constant volume cell very well, and is recommended to be applied in similar setups.

Implementation of the Valencia model

The Valencia model is based on the conservation laws of fuel mass, total momentum and energy. By assuming Gaussian profiles of fuel mass fraction, velocity and the enthalpy difference between axis and ambient gas, the 2D equations are reduced to 1D equations, which are much easier to be solved. The values along the spray axis are firstly solved. Then the value at any location can be obtained via the Gaussian function. Temperature, for example, is obtained from the local fuel mass fraction and enthalpy.

First of all, the velocity $U(x, r)$, fuel mass fraction $f(x, r)$ and specific enthalpy $h(x, r)$ profiles can be described by

$$\frac{U(x, r)}{U_{cl}(x)} = \left[\frac{f(x, r)}{f_{cl}(x)} \right]^{1/Sc} = \left[\frac{h(x, r) - h_{a,\infty}}{h_{cl}(x) - h_{a,\infty}} \right]^{1/Pr} = \exp \left[-k \left(\frac{r}{x} \right)^2 \right]. \quad (\text{A.1})$$

where Sc is the Schmidt number and Pr the Prandtl number. Physically, Sc is the ratio of viscous diffusion rate and mass diffusion rate; Pr is the ratio of viscous diffusion rate and thermal diffusion rate. Since the dependencies over Sc and Pr are quite small, both parameters are set to be 1 to simplify the problem, meaning the momentum, mass and enthalpy diffuse in the same rate.

The edge of the spray is defined as $r = R = x \tan(\theta/2)$. Somewhat arbitrarily, the velocity is defined to have dropped to 1% of the centerline value. In that case the exponent in the equation is 0.01, so that

$$k = \frac{\ln(100)}{\tan^2(\theta/2)}. \quad (\text{A.2})$$

In the steady condition, the conservation equation of axial fuel mass flux can be written as

$$\begin{aligned} M_{f,0} = M_f(x) &= \int_0^\infty \rho(x, r) U_{cl} \exp(-k\xi^2) \cdot f_{cl} \exp(-k\xi^2) \cdot 2\pi r dr \\ &= 2\pi x^2 \cdot U_{cl}(x) \cdot f_{cl}(x) \cdot \int_0^\infty \rho(\xi, f_{cl}(x)) \cdot \exp(-2k\xi^2) \cdot \xi \cdot d\xi \end{aligned}$$

where $M_f(x)$ is the flux of fuel mass and $\xi = r/x$.

In the conservation equations, the cross-sectional integral is denoted as $F(f_{cl}(x), k)$:

$$F(f_{cl}(x), k) = \int_0^\infty \rho(\xi, f_{cl}(x)) \cdot \exp(-2k\xi^2) \cdot \xi \cdot d\xi. \quad (\text{A.3})$$

Similarly, the conservation equations of axial momentum, fuel mass and energy are formulated as

$$I_0 = I(x) = 2\pi x^2 \cdot U_{cl}^2(x) \cdot F(f_{cl}(x), k) \quad (\text{A.4})$$

$$M_{f,0} = M_f(x) = 2\pi x^2 \cdot U_{cl}(x) \cdot f_{cl}(x) \cdot F(f_{cl}(x), k) \quad (\text{A.5})$$

$$H_0 = H(x) = 2\pi x^2 \cdot U_{cl}(x) \cdot (h_{cl}(x) - h_{a,\infty}) \cdot F(f_{cl}(x), k) \quad (\text{A.6})$$

where $I(x)$ is the axial momentum flux and $H(x)$ the axial enthalpy flux. In another form, these equations can be simplified as:

$$f_{cl}(x) = \sqrt{\frac{1}{2\pi} \frac{1}{F(f_{cl}(x), k) \cdot I_0}} \cdot \frac{M_{f,0}}{x} \quad (\text{A.7})$$

$$U_{cl}(x) = f_{cl}(x) \cdot \frac{I_0}{M_{f,0}} \quad (\text{A.8})$$

$$h_{cl}(x) - h_{a,\infty} = f_{cl}(x) \cdot \frac{H_0}{M_{f,0}} = f_{cl}(x) \cdot (h_{f,0} - h_{a,\infty}) \quad (\text{A.9})$$

If Eq. (A.7) can be solved, then the velocity and enthalpy will be known from Eq. (A.8) and Eq. (A.9). We solve Eq. (A.7) in two steps. Firstly, from the thermodynamic relations and Eq. (A.9) we can find the function of $\rho(f)$. Then, in the second step, we determine the $f_{cl}(x)$ function. The detailed explanation follows.

Rewriting Eq. (A.9), we have:

$$h_{cl}(x) = f_{cl}(x) \cdot (h_{f,0} - h_{a,\infty}) + h_{a,\infty} = \sum Y_i \cdot h_i(T), \quad (\text{A.10})$$

where Y_i represents the mass fraction of the different components in the mixture. Y_{fl} is the mass fraction of fuel in liquid phase, Y_{fv} the mass fraction of fuel in vapor phase and Y_a is the mass fraction of ambient gas. Y_{fv} is determined by the saturated vapor pressure $P_{sat}(T)$, which is a function of local temperature:

$$Y_{fv} = Y_a \cdot \frac{Mw_f}{Mw_a} \cdot \frac{1}{\frac{P_{tot}}{P_{sat}(T)} - 1} \quad (\text{A.11})$$

where Mw_f is the molecular weight of fuel and Mw_a the molecular weight of ambient gas. By definition, we also know that $Y_{fl} + Y_{fv} = f_{cl}$ and $Y_a = 1 - f_{cl}$.

Inserting Y_i relations into Eq. (A.10), the equation only has two variables: T and f . So function $T(f)$ is obtained. Then the density of the mixture is determined by:

$$\rho(\xi, f_{cl}(x)) = \frac{1}{\frac{Y_{fl}}{\rho_f} + \frac{Y_{fv}}{\rho_v} + \frac{Y_a}{\rho_a}}, \quad (\text{A.12})$$

where ρ_{fl} is the density of liquid fuel, ρ_{fv} the density of fuel vapor and ρ_a the density of ambient gas. These densities values are the density of pure species at local temperature and pressure. Thus they are functions of temperature as well.

Inserting Eq. (A.12) and $T(f)$ into Eq. (A.7), this equation can be solved numerically. With $f_{cl}(x)$, the temperature distribution $T(x, r)$ can be given by using the local fuel mass fraction and the relation $T(f)$.

APPENDIX B

Toluene LIF Data processing

The toluene LIF data processing procedure includes removing background, spatial alignment, flat field correction, ratio calculation and converting to temperature distribution. We obtain an image pair, of which $I_r(x, y)$ is the pixel intensity of the “red” part of the spectrum (320 nm) at position x, y and $I_b(x, y)$ is the pixel intensity of the “blue” part of the spectrum (280 nm). In case of one-side configuration, the data correction procedure for both images can be expressed as:

$$I_{r,corr}(x, y) = (I_r(x, y) - B_r(x, y)) \cdot TR(x, y) \cdot F_r(x, y) \quad (\text{B.1})$$

and

$$I_{b,corr}(x, y) = (I_b(x, y) - B_b(x, y)) \cdot F_b(x, y), \quad (\text{B.2})$$

where $B(x, y)$ is the background signal, $TR(x, y)$ the spatial transformation matrix and $F(x, y)$ is the flat field matrix. In case of opposite configuration, the data processing procedure can be expressed as:

$$I_{r,corr}(x, y) = (I_r(x, y) - B_r(x, y)) \cdot TR(x, y) \cdot C_r(x, y) \quad (\text{B.3})$$

and

$$I_{b,corr}(x, y) = (I_b(x, y) - B_b(x, y)), \quad (\text{B.4})$$

where the major difference is the co-flat-fielding matrix $C_r(x, y)$. To only present temperature regions which have reasonable accuracy, pixels with less than 300 counts are neglected because of the low signal-to-noise ratio. The temperature distribution can be obtained with the calibration relation.

$$T(x, y) = T(R(x, y)) = T\left(\frac{I_{r,2}(x, y)}{I_{b,2}(x, y)}\right) \cdot BS(x, y), \quad (\text{B.5})$$

where $R(x, y)$ is the LIF ratio distribution and $BS(x, y)$ is the correction for the beam splitter, which is only used in the one-side configuration of the HPC experiments.

Acknowledgement

The writing of this dissertation has been the most significant academic challenge I have ever faced so far. Without the support, help, guidance and patience of many people, this study would not have been completed. It was to them that I own my deepest gratitude.

I wish to thank first my promoter Prof. Philip de Goey. His support and trust during the whole process, especially the period that everything seems to be going wrong, have been extremely valuable. His guidance in both scientific research and project management skills had helped me a lot. I also owe many thanks to Prof. Rik Baert, who had been my promoter and guided me in the first year of my PhD career.

It gives me great pleasure in acknowledging the support and help of my co-promoters Dr.ir. Carlo Luijten and Dr. Nico Dam. Carlo has been my daily supervisor since the beginning of my PhD career. His guidance and the huge efforts that he had put in refining the dissertation are of great value. His critical thinking and time management skills had influenced me a lot. Nico had brought in great knowledge in laser diagnostics. Without his guidance and help in experimental work, this thesis will take much longer time to finish.

During the project, I have had the great pleasure to work with Dr.ir Rob Bastiaans, Ron, Cemil, Jeroen and Bert. We developed and refined the cooling model, toluene-LIF and BAM-LIP together. I would like to thank Prof. Marcus Aldén, Gustaf Särner, Johannes Lindén, Christoph Knappe, Dr. Gilles Bruneaux and Gabrielle Tea for their help in the laser diagnostics.

I own many thanks to Hans, Gerard, Henri, Theo, Paul, Bart, Geert-Jan, Jan, Mark and Frank. You are the most reliable technical support people. And Marjan, you are always willing to help and I think you are the best secretary in the world.

It was very nice to share the same office with Xander, Marcelo, Atieh and Maurice. Your presence had made our office a pleasant place to work. I also want to thank all the colleagues in our group. I will never forget the joyful moments that we shared together in coffee breaks, lunches and group outings etc. I wish you all good luck and success in you future career.

I would like to thank my friends Cecilia, Chen, Emma, Jie, Jiangtao, Lei, Li, Ping, Qianqian, Qiwei, Rui, Ruojuan, Shaohao, Tong, Xiangyu, Yu, YuanYuan, Yuan, Zhe, Zhipeng, Ziqian and all other friends for your help and the great happiness that we

shared together.

Finally, it is beyond the words to express my feelings to the selfless support and love of my parents. They always back me up in all difficult times. And my love, Ying Shen, had accompanied me in the whole Phd study. Her understanding and support are of great value to me and made this work more meaningful.

Miao Yu

Veldhoven, October, 2012

Curriculum Vitae

Miao Yu was born on 18-03-1981 in Anhui, China. After finishing his Bachelor of Science's degree in 2002 at the University of Science and Technology of China (USTC), he worked for two years in the Shock Wave Lab at USTC. He studied Fluid Mechanics at the same university and graduated with the Master of Science's degree in 2007. From December 2007, he started a PhD project at the Eindhoven University of Technology (TU/e) of which the results are presented in this dissertation.

